The pseudoparticle approach in SU(2) Yang-Mills theory

Den Naturwissenschaftlichen Fakultäten
der Friedrich-Alexander-Universität Erlangen-Nürnberg
zur
Erlangung des Doktorgrades

vorgelegt von
Marc Wagner
aus Nürnberg

Als Dissertation genehmigt von den Naturwissenschaftlichen Fakultäten
der Universität Erlangen-Nürnberg

Tag der mündlichen Prüfung:	24. Juli 2006
Vorsitzender der Promotionskommission:	Prof. Dr. D.-P. Häder
Erstberichterstatter:	Prof. Dr. F. Lenz
Zweitberichterstatter:	Prof. Dr. J. W. Negele

To my parents Margit and Friedrich Wagner

Zusammenfassung

In dieser Arbeit wird ein effektives Modell für SU(2)-Yang-Mills-Theorie vorgestellt, der Pseudoteilchen-Ansatz. Die Grundidee besteht darin, das Pfadintegral auf diejenigen Eichfeldkonfigurationen zu beschränken, die als Summe einer kleinen Anzahl von Pseudoteilchen dargestellt werden können, und die Integration über alle Feldkonfigurationen durch eine Integration über Pseudoteilchen-Freiheitsgrade zu ersetzen, beispielsweise Amplituden und Farbausrichtungen.

Es wird gezeigt dass der Pseudoteilchen-Ansatz bei geeigneter Wahl der Bausteine, zum Beispiel 400 Instantone, Antiinstantone und Akyronen, wesentliche SU(2)-Yang-Mills-Eigenschaften reproduziert:

- Das statische Quark-Antiquark-Potential ist linear für große Abstände mit einer attraktiven $1/R$-Korrektur wie vom bosonischen String-Bild vorausgesagt.
- Die Stringspannung ist eindeutig positiv, was ein klares Signal für Confinement ist.
- Die Stringspannung, die topologische Suszeptibilität und die kritische Temperatur des Confinement-Deconfinement-Phasenübergangs zeigen konsistente Skalierungseigenschaften bezogen auf die Kopplungskonstante.
- Dimensionslose Verhältnise bestehend aus Stringspannung, topologischer Suszeptibilität und kritischer Temperatur sind in qualitativer Übereinstimmung mit Gitterergebnissen.

Um die Wichtigkeit gewisser Klassen von Eichfeldkonfigurationen in Bezug auf Confinement festzustellen, werden unterschiedliche Pseudoteilchen-Ensembles verglichen. Die Ergebnisse deuten darauf hin dass topologische Ladung ebenso wie langreichweitige Wechselwirkungen zwischen Pseudoteilchen wesentliche Eigenschaften von Feldkonfigurationen sind, die für Confinement verantwortlich sind.

Abstract

We present an effective model for SU(2) Yang-Mills theory, the pseudoparticle approach. The basic idea is to restrict the path integral to those gauge field configurations, which can be written as a sum over a small number of pseudoparticles, and to replace the integration over all field configurations by an integration over pseudoparticle degrees of freedom, e.g. amplitudes and color orientations.

We demonstrate that the pseudoparticle approach with a suitable choice of building blocks, e.g. 400 instantons, antiinstantons and akyrons, is able to reproduce many essential features of SU(2) Yang-Mills theory:

- The static quark antiquark potential is linear for large separations with an attractive $1/R$-correction as predicted by the bosonic string picture.
- The string tension is unambiguously positive, which is a clear indication of confinement.
- The string tension, the topological susceptibility and the critical temperature of the confinement deconfinement phase transition exhibit consistent scaling behaviors with respect to the coupling constant.
- Dimensionless ratios involving the string tension, the topological susceptibility and the critical temperature are in qualitative agreement with lattice results.

To determine the importance of certain classes of gauge field configurations with respect to confinement, we compare different pseudoparticle ensembles. Our findings indicate that topological charge as well as long range interactions between pseudoparticles are essential properties of confining gauge field configurations.

Contents

1 Introduction **5**

1.1 The basic principle of the pseudoparticle approach 6

1.2 Outline 7

2 Pseudoparticle ensembles in SU(2) Yang-Mills theory **9**

2.1 Building blocks of pseudoparticle ensembles: instantons, antiinstantons and akyrons 9

2.2 Pseudoparticle ensembles 11

2.2.1 $\mathcal{A}$-ensembles 11

2.2.2 $\mathcal{AC}$-ensembles 12

2.2.3 $\mathcal{S}^{12}$-ensembles 12

2.2.4 Ultraviolet regulators and the role of the coupling constant 13

2.3 Numerical realization of pseudoparticle ensembles 14

2.3.1 Monte-Carlo simulations 14

2.3.1.1 A single Monte-Carlo step in the Metropolis algorithm 15

2.3.1.2 Calculating the action numerically 15

2.3.1.3 A single Monte-Carlo simulation 17

2.3.1.4 The whole procedure for generating field configurations 18

2.3.2 Boundary effects and how to exclude them 18

2.4 Varying the number of pseudoparticles 19

2.5 Compact degrees of freedom versus non-compact degrees of freedom 21

3 Calculating observables **23**

3.1 The static quark antiquark potential 23

3.1.1 Calculating the string tension σ and the Coulomb coefficient α 25

3.1.1.1 Method 1: area perimeter fits 25

3.1.1.2 Method 2: Creutz ratios 27

3.1.1.3 Method 3: generalized Creutz ratios . . . 30
3.1.1.4 Method 4: fitting the Wilson loop ansatz to $-\ln\langle W_{(R,T)}\rangle$ . . . 32
3.1.1.5 Comparison of method 1 to 4 . . . 33
3.1.2 Calculating the static quark antiquark potential . . . 34
3.2 The topological susceptibility . . . 35
3.3 The critical temperature of the confinement deconfinement phase transition . . . 37
3.3.1 The pseudoparticle approach in finite temperature SU(2) Yang-Mills theory 37
3.3.1.1 Periodic pseudoparticles . . . 37
3.3.1.2 The spacetime region . . . 39
3.3.1.3 The pseudoparticle density . . . 40
3.3.2 The ensemble average of the Polyakov loop as order parameter . . . 40

4 Applications **45**
4.1 Pseudoparticle excitations and gauge field distributions . . . 45
4.1.1 The distribution of instanton, antiinstanton and akyron amplitudes . . . 45
4.1.2 The distribution of the transverse part and the longitudinal part of the gauge field . . . 46
4.2 Pseudoparticles of different size . . . 47
4.3 Gaussian localized pseudoparticles of different size . . . 49
4.4 The effect of instantons, antiinstantons and akyrons . . . 51
4.5 Very large pseudoparticle ensembles . . . 53
4.6 The pseudoparticle approach in quantum mechanics . . . 55
4.6.1 Calculating energy levels in the path integral formalism . . . 55
4.6.2 Application of the pseudoparticle approach . . . 56

5 Summary and outlook **59**
5.1 The pseudoparticle approach as a successful effective model for SU(2) Yang-Mills theory . . . 59
5.2 Applications of the pseudoparticle approach . . . 60
5.3 Concluding remarks . . . 61

A Euclidean SU(2) Yang-Mills theory **63**

B Data analysis and error bars **65**
B.1 Error bars for ensemble averages ($\langle s\rangle$, $\langle|A^a_\parallel|\rangle$, $\langle|A^a_\perp|\rangle$, $\langle W_{(R,T)}\rangle$, $\langle Q_V^2\rangle$ and $\langle L\rangle_\beta$) . 65

B.2 Error bars for $-\ln\langle W_{(R,T)}\rangle$ 65
B.3 Error bars for σ and α (fitting methods) and $V_{\mathrm{q\bar{q}}}(R)$ 66
B.4 Error bars for $-\ln(\Gamma_X(R_1,\ldots,T_4))$, σ and α (generalized Creutz ratios) 66
B.5 Error bars for T_{critical} 66
B.6 Error bars for $\chi^{1/4}/\sigma^{1/2}$ and $T_{\mathrm{critical}}/\sigma^{1/2}$ 66

C Color orientation matrices **67**

D Any linear superposition of akyrons has vanishing topological charge density **69**

E The Fourier transform of a pseudoparticle **71**

E.1 Instantons and antiinstantons form transverse gauge fields, akyrons form longitudinal gauge fields 72

F The continuum limit in the pseudoparticle approach **73**

F.1 The gauge field 73
F.2 The integration measure 75
F.3 Approximations with the correct naive continuum limit 75
F.3.1 "$\mathcal{A}$-ensembles" 76
F.3.2 "$\mathcal{S}^{12}$-ensembles" 76

G Calculating Wilson loops numerically **77**

G.1 Choosing an appropriate number of sample points 78

Chapter 1

Introduction

When Richard P. Feynman published his famous path integral paper in 1948 [1], a new formalism for quantum mechanics and quantum field theory was born. Meanwhile, the path integral formalism is a standard tool in quantum field theory, both for perturbative calculations, where path integrals permit a simple and straightforward derivation of Feynman rules, and for non-perturbative calculations, where observables are expressed in terms of Euclidean path integrals, which can be computed numerically.

In order to calculate path integrals numerically, one usually introduces a discretized spacetime lattice to reduce them to ordinary multidimensional integrals. In the case of quantum chromodynamics the corresponding theory is known as lattice gauge theory. Since its first formulation by Wilson in 1974 [2] and the pioneering numerical work of Creutz [3, 4, 5, 6], enormous progress has been made. Today at least the gauge sector, that is the pure gluonic theory, can be handled very efficiently and is well understood from a numerical point of view.

Although solving path integrals on the lattice to produce numerical values for physical quantities is an important and interesting field, physicists are also interested in getting a sound understanding of the underlying mechanisms. Especially the striking phenomenon of confinement, emerging already from the deceptively simple Yang-Mills Lagrangian, is not well understood yet. A common approach to tackle this problem is to replace the path integral by an integration over a subclass of gauge field configurations. By doing so, one can study the effect of these field configurations on certain observables, in particular on the string tension and on the quark antiquark potential. This in turn might help to clarify the physical mechanism responsible for confinement.

Many such attempts, most of them considering pure SU(2) Yang-Mills theory instead of full QCD, have been made: there are ensembles of singular gauge instantons, instanton gas models and instanton liquid models, and ensembles of calorons (there are numerous papers on this subject; c.f. e.g. [7] and references therein), ensembles of regular gauge instantons and ensembles of merons [8, 9], or the identification and removal of center vortices on the lattice (c.f. e.g. [10]), just to name a few of them. Some of these approaches have analytical aspects but most of them extensively resort to numerical methods.

In this work we generalize the idea of studying certain classes of gauge field configurations, especially their importance with regard to confinement. To this end, we introduce the pseudoparticle approach [11], an effective model for SU(2) Yang-Mills theory. The basic principle of

this method is to represent the gauge field in the path integral as a sum over a fixed number of pseudoparticles, typically around 400, and to replace the integration over all field configurations by an integration over the pseudoparticle degrees of freedom. The intention is to use a significantly smaller number of degrees of freedom than in lattice calculations (≈ 400 in the pseudoparticle approach compared to e.g. $16^4 \times 12 = 786,432$ on a 16^4-lattice) but to produce results, which are in qualitative agreement with lattice results. We specify a couple of pseudoparticle ensembles and demonstrate that they are able to reproduce many essential features of SU(2) Yang-Mills theory, particularly confinement. We also consider pseudoparticle ensembles, which do not yield confinement. Comparing these results gives evidence that topological charge and long range interactions between pseudoparticles are necessary properties of confining gauge field configurations.

1.1 The basic principle of the pseudoparticle approach

In contrast to a particle, which is localized in space but not in time, a pseudoparticle is a field configuration, which is localized in space as well as in time. When talking about pseudoparticles in SU(2) Yang-Mills theory, one usually thinks about instantons and antiinstantons (c.f. (A.10) and (A.11)), which have been a very successful tool for many years and which are therefore widely known. An instanton/antiinstanton is a solution of the classical Yang-Mills equations of motion (A.9). It is the minimum action field configuration with topological charge $Q = \pm 1$. However, this work is not about instantons and antiinstantons in particular. In our context, a pseudoparticle can be any localized gauge field configuration. It is not necessarily a solution of the classical equations of motion. In general it is rather far from that.

The pseudoparticle approach is a numerical technique to approximate path integrals in Euclidean SU(2) Yang-Mills theory (c.f. Appendix A):

$$\left\langle \mathcal{O} \right\rangle \;=\; \frac{1}{Z} \int DA\, \mathcal{O}[A] e^{-S[A]} \quad , \quad Z \;=\; \int DA\, e^{-S[A]} \tag{1.1}$$

with the action S defined by (A.1). The basic idea behind the pseudoparticle approach is to represent the gauge field A_μ^a as a linear superposition of a small number of pseudoparticles, typically around 400, where each of the pseudoparticles has a position and certain other parameters, e.g. an amplitude and/or a color orientation. Written in a very general form the gauge field is given by

$$A_\mu^a(x) \;=\; \sum_i (\rho(i)a)_\mu^a(x - z(i)) + \sum_j (\rho(j)\tilde{a})_\mu^a(x - z(j)) + \ldots , \tag{1.2}$$

where the values of the indices i and j are from different ranges, a and $\tilde{a}$ are different types of pseudoparticles, $\rho(i)$ contains the parameters of the i-th pseudoparticle and $z(i)$ is the position of the i-th pseudoparticle. Figure 1.1 shows (1.2) in a graphical way. It is important to stress that such a sum of pseudoparticles is not supposed to be close to a solution of the classical Yang-Mills equations, like it is the case e.g. in instanton gas models. Even if every building block on its own is a solution of the classical equations of motion, we usually pack them together so tightly that the resulting sum is far from that. The intention of the pseudoparticle approach is to describe full quantum physics and not only certain semiclassical corrections.

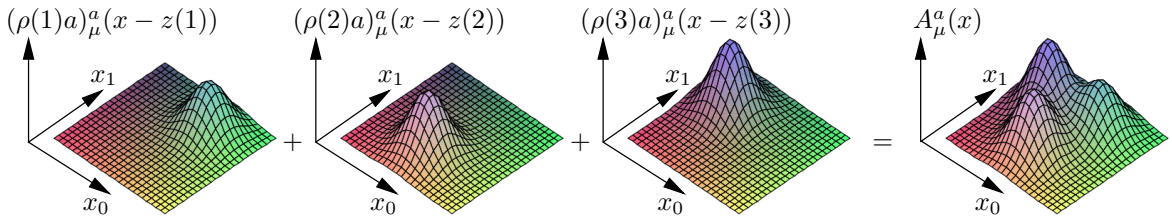

Figure 1.1: (1.2) illustrated graphically. In this specific example there are only three pseudoparticles, which are of the same type.

The integration over all field configurations in the path integral is replaced by an integration over the parameters $\rho(i)$ of the pseudoparticles:

$$\int DA \ldots \quad \rightarrow \quad \int \prod_i d\rho(i) \ldots \tag{1.3}$$

When considering a spacetime region with a finite number of pseudoparticles, this is an ordinary multidimensional integral, which can be computed by Monte-Carlo methods.

Note that the pseudoparticle approach is a very general technique, which can also be applied to other quantum field theories with only minor modifications. An example, the harmonic oscillator in quantum mechanics, is discussed in section 4.6.

The starting point of this work has been [8, 9]. However, there are two important generalizations of the techniques presented therein:

- We do not restrict our approach to instantons and merons. In the following a pseudoparticle can be any localized gauge field configuration. For example we also employ pseudoparticles without topological charge, so called akyrons (c.f. (2.3)), and Gaussian localized pseudoparticles, that is pseudoparticles without long range interactions (c.f. section 4.3).
- In addition to a color orientation matrix we also assign each pseudoparticle a variable amplitude. Due to that amplitude the pseudoparticles are able to model small quantum fluctuations.

Parts of this work have already been published [11].

1.2 Outline

This work is organized as follows.

In Chapter 2 we specify the pseudoparticles and pseudoparticle ensembles, which we will consider for the major part of this work. We also discuss the numerical realization of pseudoparticle ensembles.

In Chapter 3 we show how certain observables can be calculated in the pseudoparticle approach: the quark antiquark potential, the topological susceptibility and the critical temperature of

the confinement deconfinement phase transition. We also present numerical results, which are in qualitative agreement with lattice results. Our results demonstrate that the pseudoparticle approach with an appropriate choice of pseudoparticles is able to reproduce many essential features of SU(2) Yang-Mills theory.

In Chapter 4 we compare different pseudoparticle ensembles, where some of them are confining and others are not. The intention is to find out necessary properties of confining gauge field configurations. We also consider very large pseudoparticle ensembles and discuss possible connections to non-compact lattice gauge theory. Finally, we apply the pseudoparticle approach to quantum mechanics.

In Chapter 5 we summarize our results and give a brief outlook regarding further research.

There is a short review of Euclidean SU(2) Yang-Mills theory in Appendix A. It might be helpful to clarify our notation and conventions.

In Appendix B we deal with data analysis. We explain in detail how error bars appearing in the plots throughout this work have been generated.

Chapter 2

Pseudoparticle ensembles in SU(2) Yang-Mills theory

2.1 Building blocks of pseudoparticle ensembles: instantons, antiinstantons and akyrons

A pseudoparticle is a gauge field configuration, which is localized in space and in time. For the most part of this work we consider pseudoparticles

$$A^a_\mu(x) = \mathcal{A}(i)\mathcal{C}^{ab}(i)a^b_{\mu,\text{instanton}}(x-z(i)) \quad , \quad a^b_{\mu,\text{instanton}}(x) = \eta^b_{\mu\nu}\frac{x_\nu}{x^2+\lambda^2} \tag{2.1}$$

$$A^a_\mu(x) = \mathcal{A}(i)\mathcal{C}^{ab}(i)a^b_{\mu,\text{antiinstanton}}(x-z(i)) \quad , \quad a^b_{\mu,\text{antiinstanton}}(x) = \bar{\eta}^b_{\mu\nu}\frac{x_\nu}{x^2+\lambda^2} \tag{2.2}$$

$$A^a_\mu(x) = \mathcal{A}(i)\mathcal{C}^{ab}(i)a^b_{\mu,\text{akyron}}(x-z(i)) \quad , \quad a^b_{\mu,\text{akyron}}(x) = \delta^{b1}\frac{x_\mu}{x^2+\lambda^2} \tag{2.3}$$

(c.f. Figure 2.1) with $\eta^b_{\mu\nu} = \epsilon_{b\mu\nu} + \delta_{b\mu}\delta_{0\nu} - \delta_{b\nu}\delta_{0\mu}$ and $\bar{\eta}^b_{\mu\nu} = \epsilon_{b\mu\nu} - \delta_{b\mu}\delta_{0\nu} + \delta_{b\nu}\delta_{0\mu}$. Each pseudoparticle has an index i, an amplitude $\mathcal{A}(i) \in \mathbb{R}$, a color orientation matrix $\mathcal{C}^{ab}(i) \in \mathrm{SO}(3)$, a position $z(i) \in \mathbb{R}^4$ and a size $\lambda \in \mathbb{R}^+$. When considering a single pseudoparticle, the color

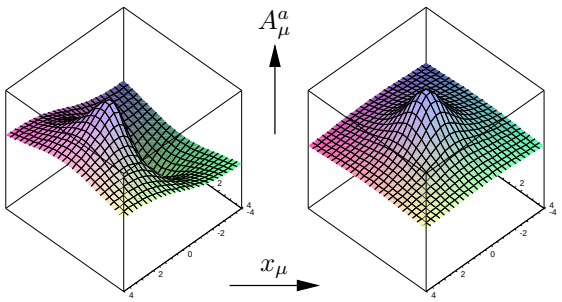

Figure 2.1: the gauge field of a single instanton, antiinstanton or akyron ($\lambda = 1.0$) plotted against suitably chosen spacetime directions.

orientation matrix is a global gauge transformation of the corresponding $a^a_{\mu,\dots}$. Since such a global gauge transformation can be specified by an element of SU(2), for which we can choose the three sphere as parameter space, it can be expressed in terms of $(c_0(i),\dots,c_3(i)) \in S^3$, i.e. $c_0(i),\dots,c_3(i) \in [-1,1]$, $c_0(i)^2 + \mathbf{c}(i)^2 = 1$:

$$\mathcal{C}^{ab}(i) \;=\; \delta^{ab}\Big(c_0(i)^2 - \mathbf{c}(i)^2\Big) + 2c_a(i)c_b(i) + 2\epsilon^{abc}c_0(i)c_c(i) \tag{2.4}$$

(c.f. Appendix C). We do not consider spatial rotations, because the effect of any spatial rotation can also be achieved by applying a suitably chosen color orientation matrix [12]. Ensembles containing such pseudoparticles are Lorentz invariant and globally gauge invariant.

Setting $\mathcal{A}(i) = 2$ in (2.1) yields an instanton in regular gauge. Although we are aware that for $\mathcal{A}(i) \neq 2$ such pseudoparticles are not actually instantons, we will nevertheless refer to them by that term. For $\mathcal{A}(i) = 2$ the action of an instanton is $S = 8\pi^2/g^2$, otherwise it is $S = \infty$. The topological charge is given by

$$Q \;=\; \frac{1}{4}\mathcal{A}(i)^2\Big(3 - \mathcal{A}(i)\Big). \tag{2.5}$$

With exception of a sign reversal in (2.5) the same applies for antiinstantons (2.2).

A single akyron is a pure gauge[1], that is $S = 0$ and $Q = 0$. Note that for a linear superposition of akyrons $S \neq 0$ in general. However, any such superposition has vanishing topological charge density (c.f. Appendix D).

A common and essential property of instantons, antiinstantons and akyrons is their long range nature. For large $|x|$ the corresponding gauge fields decrease like $1/|x|$. As a consequence these pseudoparticles have the ability to interact over large distances.

Why this particular choice of pseudoparticles?

An important reason for considering pseudoparticles (2.1) and (2.2) is their similarity to regular gauge instantons and merons, which are known to exhibit confinement [8, 9]. Therefore, using such pseudoparticles is certainly a good starting point.

Additionally we include akyrons (2.1) so that the gauge field has both a transverse part and a longitudinal part (superpositions of instantons and antiinstantons form transverse gauge fields, whereas superpositions of akyrons form longitudinal gauge fields; c.f. Appendix E.1). Furthermore, one can show that in the continuum limit, i.e. the limit of infinitely many pseudoparticles, instantons, antiinstantons and akyrons almost form a basis of all gauge field configurations (c.f. Appendix F.1).

Finally, numerous "computer experiments" with different types of pseudoparticles have shown that observables in the pseudoparticle approach are not very sensitive to moderate changes in the definition of the pseudoparticles. For example if we replace in (2.1) to (2.3) $1/(x^2+\lambda^2)$ by $\exp(-x^2/2\lambda^2)$ we get similar results for sufficiently large λ (c.f. section 4.3). It seems that results in the pseudoparticle approach hardly depend on details but rather on certain "global pseudoparticle properties", like their ability to interact over sufficiently large distances or whether they carry topological charge or not.

[1] Ancient Greek: *akyros* = pure gauge (literally "without effect").

2.2 Pseudoparticle ensembles

We place N pseudoparticles with randomly and uniformly chosen positions inside a hyperspherical spacetime volume (c.f. Figure 2.2). In the following we denote the radius of this spacetime hypersphere by $r_{\text{spacetime}}$ and its volume by $V_{\text{spacetime}}$. These quantities are related according to $V_{\text{spacetime}} = (\pi^2/2) r^4_{\text{spacetime}}$. The pseudoparticle density is given by $n = N/V_{\text{spacetime}}$. For the most part of this work we consider around 400 pseudoparticles (2.1) to (2.3) with size $\lambda = 0.5$. Usually the density is $n = 1.0$, which amounts to $r_{\text{spacetime}} \approx 3.0$.

The intention of the pseudoparticle approach is to use a significantly smaller number of degrees of freedom than in typical lattice calculations (when applying around 400 pseudoparticles this is the case; e.g. a 16^4-lattice has $16^4 \times 12 = 786,432$ degrees of freedom), but to produce results, which are in qualitative agreement. In other words, the pseudoparticles are chosen such that they represent essential degrees of freedom of SU(2) Yang-Mills theory with respect to certain observables, in particular the quark antiquark potential for large separations. Using a significantly smaller number of pseudoparticles, i.e. $N \ll 100$, is impossible, because to extract physically meaningful results we require a sufficiently large spacetime region, where border effects are negligible (c.f. Figure 2.2 and section 2.3.2).

In this work we consider three types of pseudoparticle ensembles, $\mathcal{A}$-ensembles, $\mathcal{AC}$-ensembles and $\mathcal{S}^{12}$-ensembles.

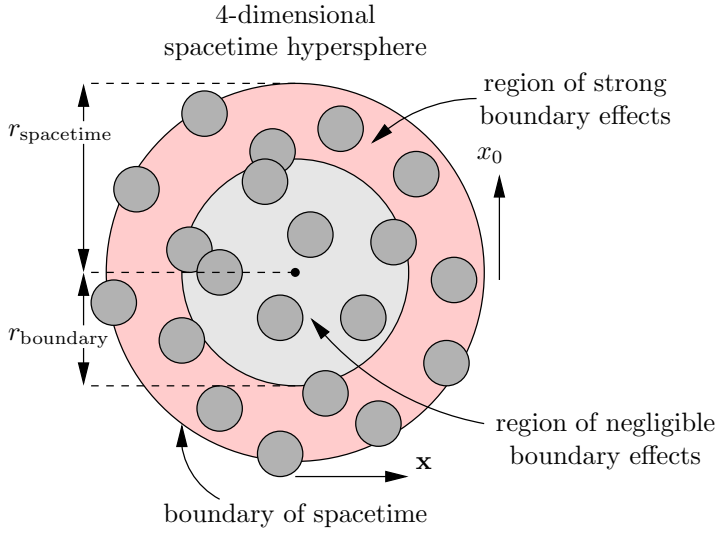

Figure 2.2: a spacetime hypersphere of radius $r_{\text{spacetime}}$ with $N = 20$ pseudoparticles (pseudoparticles are symbolized by dark gray circles).

2.2.1 $\mathcal{A}$-ensembles

The gauge field is a superposition of instantons, antiinstantons and akyrons:

$$A^a_\mu(x) \;=\; \sum_i \mathcal{A}(i)\mathcal{C}^{ab}(i) a^b_{\mu,\text{instanton}}(x - z(i)) + \sum_j \mathcal{A}(j)\mathcal{C}^{ab}(j) a^b_{\mu,\text{antiinstanton}}(x - z(j)) +$$

$$\sum_k \mathcal{A}(k)\mathcal{C}^{ab}(k)a^b_{\mu,\text{akyron}}(x - z(k)) \tag{2.6}$$

(here and in the following the indices i, j and k assume values from different ranges). In accordance with the ratio of transverse and longitudinal gauge field components, which is $3:1$, we choose $N_{\text{instanton}} : N_{\text{antiinstanton}} : N_{\text{akyron}} = 3:3:2$ ($N_{\text{instanton}}$, $N_{\text{antiinstanton}}$ and N_{akyron} are the corresponding pseudoparticle numbers). We consider an equal number of instantons and antiinstantons so that the ensemble is symmetric with respect to the topological charge (c.f. (2.5)).

The color orientations $\mathcal{C}^{ab}(i)$ are chosen randomly and uniformly on S^3.

The integration over all gauge field configurations in the path integral is approximated by

$$\int DA \ldots \;\propto\; \int \left(\prod_i d\mathcal{A}(i)\right) \ldots \tag{2.7}$$

We refer to such ensembles as $\mathcal{A}$-ensembles (integration over $\underline{\mathcal{A}}$mplitudes).

2.2.2 $\mathcal{AC}$-ensembles

We consider ensembles, which are extensions of $\mathcal{A}$-ensembles.

As before, the gauge field is given by (2.6) but the integration is performed not only over amplitudes but also over color orientations:

$$\int DA \ldots \;=\; \int \left(\prod_i d\mathcal{A}(i)\, d\mathcal{C}(i)\right) \ldots \tag{2.8}$$

We refer to such ensembles as $\mathcal{AC}$-ensembles (integration over $\underline{\mathcal{A}}$mplitudes and $\underline{\mathcal{C}}$olor orientations).

2.2.3 $\mathcal{S}^{12}$-ensembles

We consider ensembles, where nine instantons and three akyrons at a time share the same spacetime point. The gauge field is given by

$$\begin{aligned} A^a_\mu(x) \;&= \\ &= \sum_i \Bigg(\underbrace{\sum_{j=1}^{9} \mathcal{A}(i,j)\mathcal{C}^{ab}(i,j)}_{=\mathcal{S}^{ab}(i)}\, a^b_{\mu,\text{instanton}}(x - z(i)) + \\ &\quad \underbrace{\sum_{k=10}^{12} \mathcal{A}(i,k)\mathcal{C}^{a1}(i,k)}_{=\mathcal{S}^{a0}(i)}\, a^1_{\mu,\text{akyron}}(x - z(i)) \Bigg) \;= \end{aligned}$$

$$= \sum_i \left(\mathcal{S}^{ab}(i) a^b_{\mu,\text{instanton}}(x - z(i)) + \mathcal{S}^{a0}(i) a^1_{\mu,\text{akyron}}(x - z(i)) \right) =$$
$$= \sum_i \mathcal{S}^{aB}(i) a^B_{\mu,\mathcal{S}^{12}}(x - z(i)), \tag{2.9}$$

where

$$a^B_{\mu,\mathcal{S}^{12}}(x) = \begin{cases} a^B_{\mu,\text{instanton}}(x) & \text{if } B = 1,2,3 \\ a^1_{\mu,\text{akyron}}(x) & \text{if } B = 0 \end{cases} . \tag{2.10}$$

We refer to $a^B_{\mu,\mathcal{S}^{12}}$ as a pseudoparticle cluster (such a cluster is equivalent to a sum of nine instantons and three akyrons). Note that there is no difference for the gauge field whether a pseudoparticle cluster is made up from instantons or from antiinstantons.

The functions $\mathcal{S}^{aB}(i) = (\mathcal{S}^{a0}(i), \mathcal{S}^{ab}(i))$, which we have defined in (2.9), are the "amplitudes" of the i-th pseudoparticle cluster. It can be shown that any $\mathcal{S}^{aB}(i)$ can be realized by suitably chosen amplitudes $\mathcal{A}(i,j)$ and $\mathcal{A}(i,k)$ and color orientation matrices $\mathcal{C}^{ab}(i,j)$ and $\mathcal{C}^{a1}(i,k)$ (c.f. Appendix C). The integration over all field configurations (F.9) is approximated by

$$\int DA \ldots \propto \int \left(\prod_{i,a,B} d\mathcal{S}^{aB}(i) \right) \ldots \tag{2.11}$$

We refer to such ensembles as $\mathcal{S}^{12}$-ensembles (a pseudoparticle cluster is a $\underline{\mathcal{S}}$um of $\underline{12}$ pseudoparticles).

Numerically it is less time consuming to calculate observables in an $\mathcal{S}^{12}$-ensemble than in an $\mathcal{A}$-ensemble or an $\mathcal{AC}$-ensemble with the same number of pseudoparticles.

2.2.4 Ultraviolet regulators and the role of the coupling constant

In lattice calculations there is one ultraviolet regulator, the lattice spacing. In physical units it can be adjusted by choosing appropriate values for the coupling constant g. The scale is usually set by identifying the string tension σ with the physical value $4.2/\text{fm}^2$.

In the pseudoparticle approach the minimum size of ultraviolet fluctuations is determined by the pseudoparticle size λ and the average pseudoparticle distance $\bar{d} = 1/n^{1/4}$. Therefore, there are two ultraviolet regulators. We expect that a variation of the coupling constant g has a similar effect in the pseudoparticle approach as it has in lattice calculations: λ and $\bar{d}$ in physical units are changed (as is any other dimensionful quantity) but their ratio remains constant.

However, in contrast to lattice calculations we also have to specify the ratio $\lambda/\bar{d}$. A priori it is not clear how to choose that ratio. A sensible requirement is certainly that λ and $\bar{d}$ are of the same order of magnitude. For our standard choice, $\lambda = 0.5$ and $\bar{d} = 1/n^{1/4} = 1.0$, this is the case. Ultimately, numerical calculations are necessary to check whether a certain ratio yields meaningful results. For $\lambda/\bar{d} = \lambda n^{1/4} = 0.2 \ldots 1.1$ numerical calculations have shown that physical quantities are pretty stable with respect to a variation of $\lambda/\bar{d}$ and that there is qualitative agreement with lattice results (c.f. section 4.2).

2.3 Numerical realization of pseudoparticle ensembles

We approximate path integral expectation values by ensemble averages of either an $\mathcal{A}$-ensemble, an $\mathcal{AC}$-ensemble or an $\mathcal{S}^{12}$-ensemble (c.f. section 2.2.1 to 2.2.3). In each of the three cases the integral over all field configurations is replaced by a finite dimensional integral (c.f. (2.7), (2.8) and (2.11)), which can be computed by Monte-Carlo simulations. Only the action inside the spacetime hypersphere is considered for such a "path integral".

Putting everything together, the ensemble average of a quantity $\mathcal{O}$ in an $\mathcal{A}$-ensemble is given by

$$\left\langle \mathcal{O} \right\rangle \;=\; \frac{1}{Z} \int \left(\prod_{i=1}^{N} d\mathcal{A}(i) \right) \mathcal{O}(\mathcal{A}(i)) e^{-S(\mathcal{A}(i))} \quad , \quad Z \;=\; \int \left(\prod_{i=1}^{N} d\mathcal{A}(i) \right) e^{-S(\mathcal{A}(i))} \tag{2.12}$$

$$S(\mathcal{A}(i)) \;=\; \int_{V_{\text{spacetime}}} d^4x \, s(\mathcal{A}(i)) \tag{2.13}$$

(the quantity $\mathcal{O}$, the action S and the action density s can be expressed in terms of $\mathcal{A}(i)$ via (2.6)). Analogous formulas hold for $\mathcal{AC}$-ensembles and for $\mathcal{S}^{12}$-ensembles.

2.3.1 Monte-Carlo simulations

In order to calculate multidimensional integrals like (2.12), we resort to Monte-Carlo simulations. A Monte-Carlo simulation is a stochastic method for obtaining an "adequate approximation" of such a multidimensional integral in a "reasonable time".

The idea behind a Monte-Carlo simulation is to generate a representative set of field configurations. Such a representative set of field configurations is a set, where the elements "seem to be distributed" according to the probability density e^{-S}/Z. Once a representative set of n field configurations is available, which is of the form

$$\Big\{ (\mathcal{A}(i))_1 \;,\; (\mathcal{A}(i))_2 \;,\; \ldots \;,\; (\mathcal{A}(i))_n \Big\} \tag{2.14}$$

when considering an $\mathcal{A}$-ensemble, an estimate for $\langle \mathcal{O} \rangle$ can be obtained by

$$\left\langle \mathcal{O} \right\rangle \;\approx\; \frac{1}{n} \sum_{j=1}^{n} \mathcal{O}((\mathcal{A}(i))_j). \tag{2.15}$$

If the field configurations in (2.14) are stochastic independent, which is often a plausible assumption, the maximum likelihood estimate for the standard deviation of $\langle \mathcal{O} \rangle$ is given by

$$\sigma(\mathcal{O}) \;\approx\; \left(\frac{1}{n(n-1)} \sum_{j=1}^{n} \Big(\mathcal{O}((\mathcal{A}(i))_j) - \left\langle \mathcal{O} \right\rangle \Big)^2 \right)^{1/2} . \tag{2.16}$$

For large n this quantity decreases like $1/\sqrt{n}$.

There exist many different Monte-Carlo algorithms. In this work we apply the Metropolis algorithm (c.f. e.g. [13]).

2.3.1.1 A single Monte-Carlo step in the Metropolis algorithm

In a single Monte-Carlo step the pseudoparticles or, in the case of an $\mathcal{S}^{12}$-ensemble, the pseudoparticle clusters are updated one by one in fixed order.

A Metropolis update is performed as follows: let A_μ^a be the current field configuration. A new field configuration $A_\mu^{a\prime}$ is generated randomly according to certain rules, which will be specified below. If $S[A] \geq S[A']$ the current field configuration is replaced by the new field configuration. If $S[A] < S[A']$ the current field configuration is replaced by the new field configuration with probability $e^{-S[A']}/e^{-S[A]}$.

In the following we specify the rules for generating new field configurations.

Updating amplitudes $\mathcal{A}(i)$ ($\mathcal{A}$-ensemble and $\mathcal{AC}$-ensemble): when updating a pseudoparticle with an amplitude $\mathcal{A}(i)$, a new amplitude $\mathcal{A}(i)' = \mathcal{A}(i) + \delta\mathcal{A}$ is generated, where $\delta\mathcal{A}$ is a random number chosen uniformly in $[\mathcal{A}(i) - \Delta\mathcal{A}, \mathcal{A}(i) + \Delta\mathcal{A}]$.

Updating color orientation matrices $\mathcal{C}^{ab}(i)$ ($\mathcal{AC}$-ensemble): as already explained, a color orientation matrix $\mathcal{C}^{ab}(i)$ can be specified by $(c_0(i), \ldots, c_3(i)) \in S^3$ (c.f. Appendix C). When updating a pseudoparticle with a variable color orientation given by $(c_0(i), \ldots, c_3(i))$, a point $(\delta c_0, \ldots, \delta c_3)$ is chosen uniformly inside a 4-dimensional hypersphere with radius $\Delta\mathcal{C}$. $(\delta c_0, \ldots, \delta c_3)$ is added to $(c_0(i), \ldots, c_3(i))$ and the result is normalized so that it is an element of S^3 again. This is the new color orientation, i. e.

$$(c_0(i)', \ldots, c_3(i)') \quad = \quad \frac{(c_0(i), \ldots, c_3(i)) + (\delta c_0, \ldots, \delta c_3)}{|(c_0(i), \ldots, c_3(i)) + (\delta c_0, \ldots, \delta c_3)|}. \tag{2.17}$$

Updating pseudoparticle clusters ($\mathcal{S}^{12}$-ensemble): when updating a pseudoparticle cluster with "amplitudes" $\mathcal{S}^{aB}(i)$, new "amplitudes" $\mathcal{S}^{aB}(i)' = \mathcal{S}^{aB}(i) + \delta\mathcal{S}^{aB}$ are generated, where $\delta\mathcal{S}^{aB}$ are random numbers chosen uniformly in $[\mathcal{S}^{aB}(i) - \Delta\mathcal{S}, \mathcal{S}^{aB}(i) + \Delta\mathcal{S}]$.

It can be shown that a Metropolis algorithm with these update rules generates a representative set of field configurations after a sufficiently long thermalization phase.

The amount of time, needed to generate a representative set of field configurations, is highly dependent on $\Delta\mathcal{A}$, $\Delta\mathcal{C}$ and $\Delta\mathcal{S}$. These parameters in turn depend on the details of the considered ensemble, e.g. the number of pseudoparticles or the coupling constant. A heuristic criterion for choosing "optimal" parameters is to adjust them so that the acceptance rate of new field configurations roughly 50% [14]. To achieve that, we multiply the parameters $\Delta\mathcal{A}$, $\Delta\mathcal{C}$ and $\Delta\mathcal{S}$ after every Monte-Carlo step with 1.5 if the acceptance rate has been greater than 70%, and we divide by 1.5 if the acceptance rate has been less than 30%. To assure that this heuristic does not spoil the generation of a representative set of field configurations, we only employ it during the first part of the thermalization phase. Reasonable initial values are $\Delta\mathcal{A} = 1.0$, $\Delta\mathcal{C} = 0.4$, $\Delta\mathcal{S} = 1.0$.

2.3.1.2 Calculating the action numerically

In order to decide whether to accept or to reject a randomly generated new field configuration, it is necessary to determine the action of the current and the new field configuration

(c.f. section 2.3.1.1). As already mentioned, we only consider the action inside the spacetime hypersphere (c.f. (2.13)). An approximate value of this action can be obtained by ordinary Monte-Carlo integration.

To this end, sample points are chosen randomly and uniformly inside the spacetime hypersphere

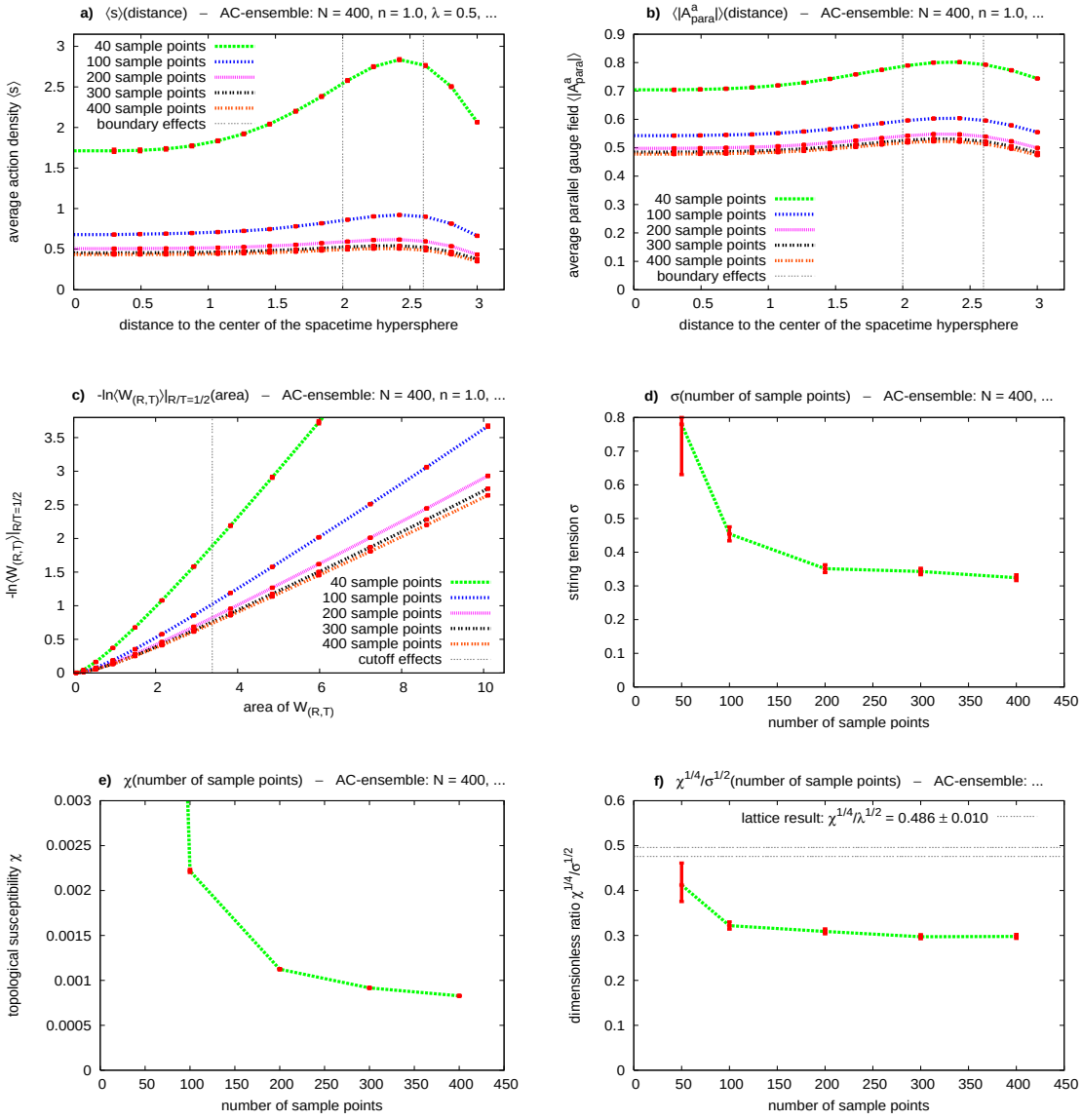

Figure 2.3: $\mathcal{AC}$-ensemble, $N = 400$, $n = 1.0$, $\lambda = 0.5$, $g = 4.0$, for $40 \ldots 400$ sample points. **a)** $\langle s \rangle$ plotted against the distance to the center of the spacetime hypersphere. **b)** $\langle |A^a_{\|}| \rangle$ plotted against the distance to the center of the spacetime hypersphere. **c)** $-\ln\langle W_{(R,T)} \rangle|_{R/T=1/2}$ plotted against the area. **d)** σ obtained by area perimeter fits plotted against the number of sample points ($R/T = 1/2$, $d_{\text{cutoff}} = 1.3$, $r_{\text{boundary}} = 2.6$; c.f. section 3.1.1.1). **e)** χ plotted against the number of sample points ($r_{\text{boundary}} = 2.0$). **f)** $\chi^{1/4}/\sigma^{1/2}$ plotted against the number of sample points.

at the beginning of each Monte-Carlo simulation. In order to save computation time, these sample points are never changed during a Monte-Carlo simulation. The number of sample points is chosen as small as possible but large enough so that effects arising from insufficient sampling are negligible. Numerical calculations have shown that 400 sample points are an acceptable tradeoff for most ensembles.

Figure 2.3 shows for a typical ensemble how certain quantities are affected by the number of sample points. For more than 200 sample points the results appear to be stable. For a detailed explanation of how the quantities shown in Figure 2.3 have been obtained, we refer to section 2.3.2 and to Chapter 3.

2.3.1.3 A single Monte-Carlo simulation

A single Monte-Carlo simulation is composed of a sequence of n_{MC} Monte-Carlo steps. The first $n_{\mathrm{MC,thermalization}}$ Monte-Carlo steps are thermalization steps, that is field configurations generated during these steps are not used for calculating ensemble averages. Even after the thermalization phase is complete, only field configurations separated by $n_{\mathrm{MC,out}}$ Monte-Carlo steps are considered for the representative set (2.14). We do not consider field configurations after every Monte-Carlo step, because such field configurations are usually very similar and, therefore, do not provide a significant amount of new information.

In order to speed up thermalization, we only use a small number of sample points for the Monte-Carlo integration of the action density at the beginning of each Monte-Carlo simulation. During the thermalization phase this number is increased until the total number of sample points, typically 400, is reached. To be more specific, we use the following heuristic rules:

- Monte-Carlo step 1 to $n_{\mathrm{MC},1}$:
  number of sample points used $= (1/16)\times$ total number of sample points.
- Monte-Carlo step $n_{\mathrm{MC},1}+1$ to $n_{\mathrm{MC},2}$:
  number of sample points used $= (1/8)\times$ total number of sample points.
- Monte-Carlo step $n_{\mathrm{MC},2}+1$ to $n_{\mathrm{MC},3}$:

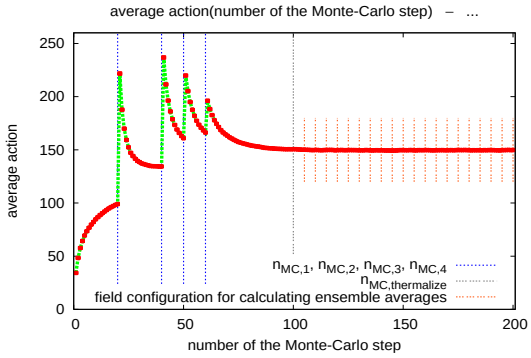

Figure 2.4: $\mathcal{AC}$-ensemble, $N = 400$, $n = 1.0$, $\lambda = 0.5$, $g = 4.0$. The average action inside the spacetime hypersphere plotted against the number of the Monte-Carlo step.

number of sample points used = (1/4)× total number of sample points.

- Monte-Carlo step $n_{\mathrm{MC},3}+1$ to $n_{\mathrm{MC},4}$:
  number of sample points used = (1/2)× total number of sample points.
- Monte-Carlo step $n_{\mathrm{MC},4}+1$ to n_{MC}:
  number of sample points used = total number of sample points.

Most of the results presented throughout this work have been generated with $n_{\mathrm{MC}} = 200$, $n_{\mathrm{MC,thermalization}} = 100$, $n_{\mathrm{MC,out}} = 5$, $n_{\mathrm{MC},1} = 20$, $n_{\mathrm{MC},2} = 40$, $n_{\mathrm{MC},3} = 50$ and $n_{\mathrm{MC},4} = 60$.

Halfway between Monte-Carlo step $n_{\mathrm{MC},4}$ and $n_{\mathrm{MC,thermalization}}$, that is several steps before generating field configurations that will be used for calculating ensemble averages, the parameters $\Delta\mathcal{A}$, $\Delta\mathcal{C}$ and $\Delta\mathcal{S}$ are no longer updated by the method explained in section 2.3.1.1.

In Figure 2.4 we plotted the average action inside the spacetime hypersphere against the number of the Monte-Carlo step for a typical ensemble. For the averaging we considered 6,000 independent Monte-Carlo simulations. From such plots we can determine when Monte-Carlo simulations have reached approximate thermal equilibrium. For the example shown in Figure 2.4 this is the case after roughly 100 Monte-Carlo steps.

2.3.1.4 The whole procedure for generating field configurations

In order to average over pseudoparticle positions and in the case of an $\mathcal{AC}$-ensemble also over color orientations, we perform a large number of independent Monte-Carlo simulations. At the beginning of each of these Monte-Carlo simulations the positions $z(i)$ of the pseudoparticles are chosen randomly and uniformly inside the spacetime hypersphere, as are the color orientation matrices $\mathcal{C}^{ab}(i)$ on S^3. All amplitudes $\mathcal{A}(i)$ and $\mathcal{S}^{aB}(i)$ are set to zero.

Most of the time we have calculated ensemble averages from 6,000 independent Monte-Carlo simulations. Together with our standard choice of parameters, $n_{\mathrm{MC}} = 200$, $n_{\mathrm{MC,thermalization}} = 100$ and $n_{\mathrm{MC,out}} = 5$, this amounts to a total of $6,000 \times 20 = 120,000$ field configurations for the representative set (2.14).

2.3.2 Boundary effects and how to exclude them

In principle we would like to consider ensembles of infinite spatial and temporal extension. However, due to numerical reasons we have to restrict spacetime to hyperspheres of finite size. The question arises whether there is a region inside a finite spacetime hypersphere, where physics is approximately the same as it is in a system of infinite extension. A necessary requirement for such a region, which can be checked numerically, is translational invariance of physically meaningful quantities. To put it another way, we have to assure that there is a spacetime region, where boundary effects are negligible. Samples of physically meaningful quantities may not be taken outside this region.

In order to check whether there is such a region, we calculate the quantities $\langle s\rangle$, $\langle|A^a_{\parallel}|\rangle$ and $\langle|A^a_{\perp}|\rangle$ as functions of the distance to the center of the spacetime hypersphere:

- $\langle s\rangle$ is the average action density.

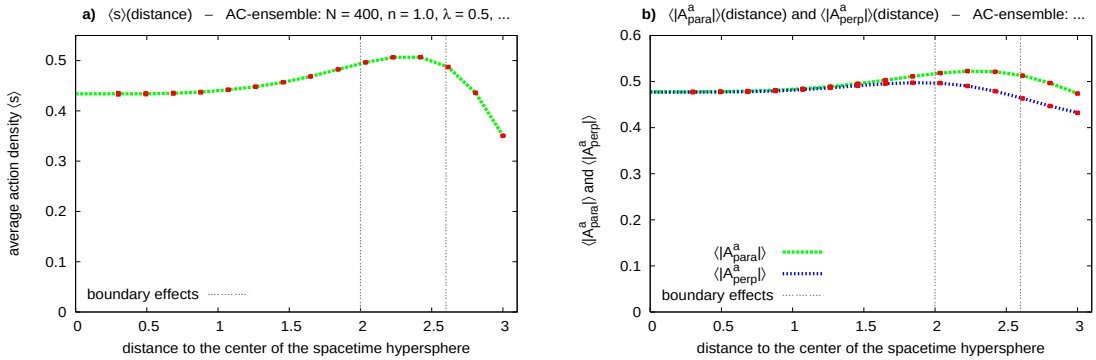

Figure 2.5: $\mathcal{AC}$-ensemble, $N = 400$, $n = 1.0$, $\lambda = 0.5$, $g = 4.0$. **a)** $\langle s \rangle$ plotted against the distance to the center of the spacetime hypersphere. **b)** $\langle |A^a_\parallel| \rangle$ and $\langle |A^a_\perp| \rangle$ plotted against the distance to the center of the spacetime hypersphere.

- $\langle |A^a_\parallel| \rangle$ is the average absolute value of those gauge field components tangential to a spherical surface centered around the origin.
- $\langle |A^a_\perp| \rangle$ is the average absolute value of those gauge field components perpendicular to a spherical surface centered around the origin.

Although the quantities $\langle |A^a_\parallel| \rangle$ and $\langle |A^a_\perp| \rangle$ are not gauge invariant and, therefore, not physically meaningful, we nevertheless expect them to be constant in regions where border effects are negligible. As long as $\langle s \rangle$, $\langle |A^a_\parallel| \rangle$ and $\langle |A^a_\perp| \rangle$ are approximately constant, we consider the corresponding hyperspherical spacetime region to be equivalent to a spacetime of infinite extension. That is in such a spacetime region boundary effects are considered to be negligible. In the following we denote the corresponding radius by r_{boundary} (c.f. Figure 2.2).

A typical example is shown in Figure 2.5 ($\mathcal{AC}$-ensemble, $N = 400$, $n = 1.0$, $\lambda = 0.5$ and $g = 4.0$). We consider the spacetime region inside a hypersphere of radius $r_{\text{boundary}} = 2.0 \ldots 2.6$ to be a region where boundary effects are negligible.

2.4 Varying the number of pseudoparticles

An important issue is to check the stability of physical quantities in the pseudoparticle approach against a variation of the pseudoparticle number N, while the pseudoparticle density $n = N/V_{\text{spacetime}}$ is kept constant. This is tantamount to studying identical ensembles of different size. One might suspect that due to the long range nature of instantons, antiinstantons and akyrons such a variation will lead to considerable changes in numerical results. However, numerical calculations have shown that this is not the case. Apparently the action forces the pseudoparticles to chose their amplitudes and color orientations such that physical quantities remain stable.

In Figure 2.6 we considered a typical example, $\mathcal{AC}$-ensembles with $n = 1.0$, $\lambda = 0.5$, $g = 4.0$ and different pseudoparticle numbers $N \in \{100\ ,\ 200\ ,\ \ldots\ ,\ 800\}$.

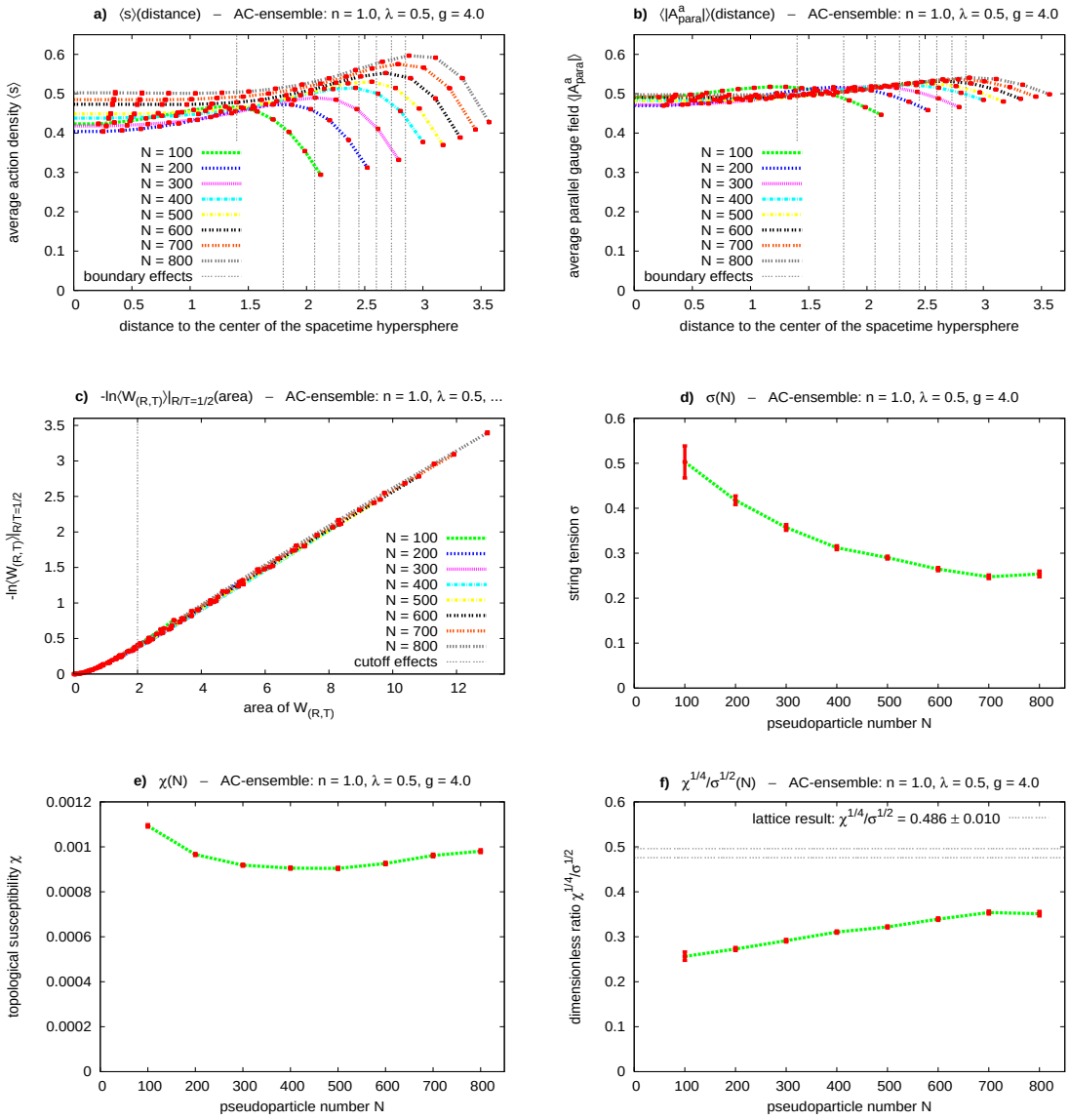

Figure 2.6: $\mathcal{AC}$-ensemble, $n = 1.0$, $\lambda = 0.5$, $g = 4.0$, for different pseudoparticle numbers $N \in \{100\ ,\ 200\ ,\ \ldots\ ,\ 800\}$. **a)** $\langle s \rangle$ plotted against the distance to the center of the spacetime hypersphere. **b)** $\langle |A^a_\parallel| \rangle$ plotted against the distance to the center of the spacetime hypersphere. **c)** $-\ln\langle W_{(R,T)} \rangle|_{R/T=1/2}$ plotted against the area. **d)** σ plotted against N. **e)** χ plotted against N. **f)** $\chi^{1/4}/\sigma^{1/2}$ plotted against N.

Figure 2.6a shows that the average action density $\langle s \rangle$ near the center of the spacetime hypersphere varies by less than 25%, although the number of pseudoparticles has been increased by a factor of 8. $\langle |A^a_\parallel| \rangle$ is even more stable with respect to N (c.f. Figure 2.6b). Figure 2.6c demonstrates that varying the pseudoparticle number has essentially no effect on Wilson loops. In order to determine the string tension, we performed area perimeter fits to $-\ln\langle W_{(R,T)} \rangle|_{R/T=1/2}$ ($R/T = 1/2$, $d_{\text{cutoff}} = 1.0$, r_{boundary} has been chosen individually so that the width of the

boundary is 0.72 for all N; c.f. section 3.1.1.1). The results are shown in Figure 2.6d. Although ensemble averages of Wilson loops are essentially independent of the pseudoparticle number, the string tension σ is increasing for decreasing N. This is the case, because for small N the area perimeter fit can only be performed to data points with small Wilson loop areas. Such data points include cutoff effects, which give rise to an unphysically large value of σ. The topological susceptibility χ is pretty stable with respect to the pseudoparticle number, as is the dimensionless ratio $\chi^{1/4}/\sigma^{1/2}$ (c.f. Figure 2.6e and Figure 2.6f).

2.5 Compact degrees of freedom versus non-compact degrees of freedom

In this section we illustrate that there is a big difference between non-compact degrees of freedom (amplitudes $\mathcal{A}(i)$ and $\mathcal{S}^{aB}(i)$) and compact degrees of freedom (color orientation matrices $\mathcal{C}^{ab}(i)$). We demonstrate that ensemble averages mainly depend on non-compact degrees of freedom, whereas compact degrees of freedom play a subdominant role. To this end, we compare the following ensembles with $N = 360$, $n = 1.0$, $\lambda = 0.5$ and $g = 4.0$:

- $\mathcal{A}$-ensemble (360 non-compact degrees of freedom).
- $\mathcal{AC}$-ensemble (360 non-compact and $360 \times 3 = 1080$ compact degrees of freedom).
- $\mathcal{S}^{12}$-ensemble ($30 \times 12 = 360$ non-compact degrees of freedom).

Note that all three ensembles have the same number of non-compact degrees of freedom.

Figure 2.7a and 2.7b show $\langle s \rangle$ and $\langle |A^a_{\|}| \rangle$ plotted against the distance to the center of the spacetime hypersphere. Although the number of degrees of freedom in the $\mathcal{AC}$-ensemble is four times the number of degrees of freedom in the $\mathcal{A}$-ensemble (there is a difference of 1080 compact degrees of freedom), the results for these ensembles are indistinguishable within statistical errors. The implication is that compact degrees of freedom have little effect. $\langle s \rangle$ and $\langle |A^a_{\|}| \rangle$ in the $\mathcal{S}^{12}$-ensemble are roughly 10% smaller. This is due to the clustering of pseudoparticles (recall, that an $\mathcal{S}^{12}$-ensemble is identical to an $\mathcal{A}$-ensemble with the exception that twelve pseudoparticles at a time share the same spacetime point). Figure 2.7c shows $-\ln\langle W_{(R,T)} \rangle|_{R/T=1/2}$ as a function of the area. For all three ensembles the results are nearly identical. The topological susceptibility is within statistical errors the same in the $\mathcal{A}$-ensemble and the $\mathcal{AC}$-ensemble, but it is larger by a factor of approximately 1.7 in the $\mathcal{S}^{12}$-ensemble. Although clustering pseudoparticles reduces the average action, it seems to have an opposite effect on the topological charge.

Our findings have been supported by a couple of similar computations, which have also shown that numerical results mainly depend on the number of non-compact degrees of freedom, i.e. the number of instantons, antiinstantons and akyrons. On the other hand, there is little difference whether we consider an $\mathcal{A}$-ensemble, an $\mathcal{AC}$-ensemble or an $\mathcal{S}^{12}$-ensemble.

We conclude that in our pseudoparticle ensembles non-compact degrees of freedom play the dominant role, whereas compact degrees of freedom are nearly negligible. Since the computation time for a Monte-Carlo update of a pseudoparticle cluster is significantly less then the time needed to update nine instantons or antiinstantons and three akyrons, we resort to $\mathcal{S}^{12}$-ensembles

whenever we want to study systems with a large number of non-compact degrees of freedom (c.f. e.g. section 4.5).

Since within statistical errors we have not observed any differences between results obtained in $\mathcal{A}$-ensembles and results obtained in $\mathcal{AC}$-ensembles, we do do not consider $\mathcal{A}$-ensembles any further. We exclusively concentrate on $\mathcal{AC}$-ensembles and $\mathcal{S}^{12}$-ensembles.

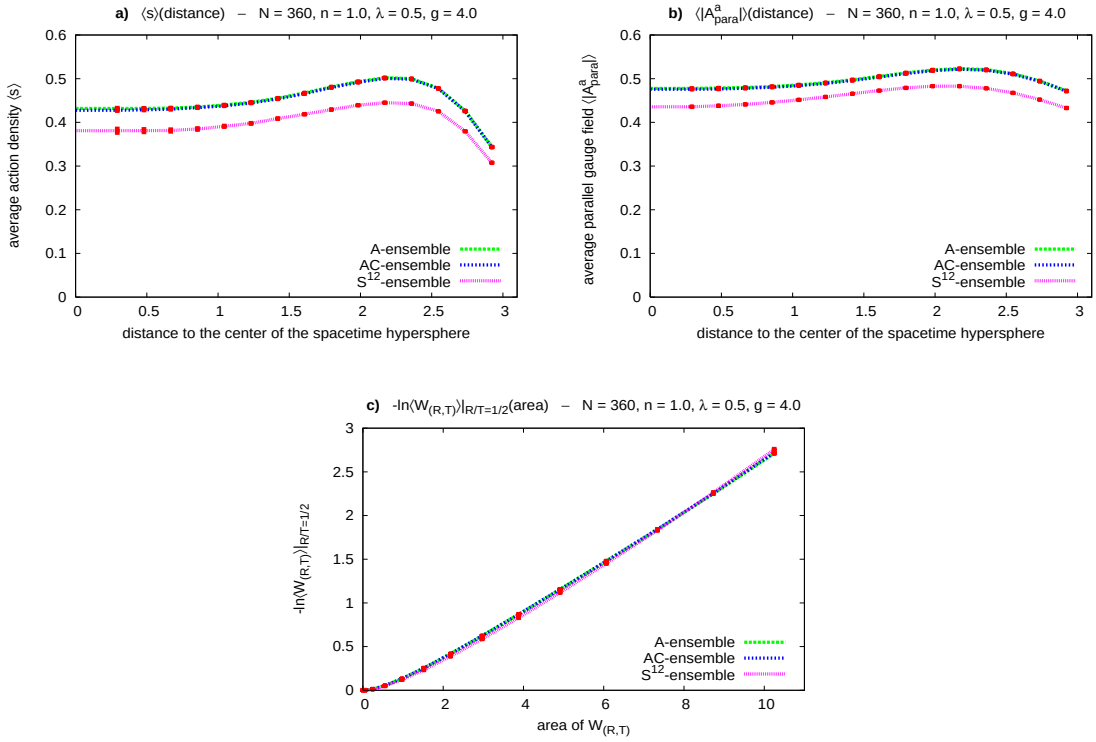

Figure 2.7: $\mathcal{A}$-ensemble, $\mathcal{AC}$-ensemble and $\mathcal{S}^{12}$-ensemble, $N = 360$, $n = 1.0$, $\lambda = 0.5$, $g = 4.0$. **a)** $\langle s \rangle$ plotted against the distance to the center of the spacetime hypersphere. **b)** $\langle |A^a_{||}| \rangle$ plotted against the distance to the center of the spacetime hypersphere. **c)** $-\ln\langle W_{(R,T)} \rangle|_{R/T=1/2}$ plotted against the area.

Chapter 3

Calculating observables

3.1 The static quark antiquark potential

For large separations the potential of a pair of infinitely heavy quarks cannot be obtained in perturbation theory. Therefore, one has to resort to numerical methods. Lattice results (c.f. e.g. [15, 16, 17]) strongly indicate that this potential is linear for large separations with an attractive $1/R$-correction as predicted by the bosonic string picture [18, 19]. It is an interesting quantity, which is closely connected to the striking phenomenon of confinement.

The common tool for studying the quark antiquark potential at zero temperature are Wilson loops. A Wilson loop W_z is defined by

$$W_z[A] \;=\; \frac{1}{2}\mathrm{Tr}\left(P\left\{\exp\left(i\oint dz_\mu\, A_\mu(z)\right)\right\}\right), \tag{3.1}$$

where z is a closed spacetime curve and P denotes path ordering (in the Taylor expansion of the exponential function gauge field matrices are ordered from right to left according to their appearance in the loop). In this work we mainly consider rectangular Wilson loops with spatial extension R and temporal extension T, which we denote by $W_{(R,T)}$. For a detailed discussion of how to calculate Wilson loops numerically we refer to Appendix G.

It is well known that the potential of a static quark antiquark pair $V_{\mathrm{q\bar{q}}}$ with separation R at zero temperature can be related to ensemble averages of rectangular Wilson loops:

$$V_{\mathrm{q\bar{q}}}(R) \;=\; -\lim_{T\to\infty}\frac{1}{T}\ln\left\langle W_{(R,T)}\right\rangle \tag{3.2}$$

(c.f. e.g. [13, 20, 21]). Of course, in numerical calculations it is impossible to consider Wilson loops of infinite temporal extension. However, there is numerical evidence that even for Wilson loops of limited size (3.2) is still an accurate approximation. This allows us to determine the quark antiquark potential numerically.

In the following we assume that for large separations the quark antiquark potential can be parameterized by

$$V_{\mathrm{q\bar{q}}}(R) \;=\; V_0 - \frac{\alpha}{R} + \sigma R. \tag{3.3}$$

This ansatz is based on the bosonic string picture [18, 19] and various numerical results from lattice calculations (c.f. e.g. [15, 16, 17]). There are three parameters:

- V_0 is a constant shift of the potential, which has no physical relevance.
- α is the coefficient in front of the attractive $1/R$-correction of the potential. We refer to α as Coulomb coefficient.
- The string tension σ is the force between a quark and an antiquark at infinite separation.

There are two basically different approaches to determine the potential of a quark antiquark pair. The first is to employ (3.2) to calculate the potential approximately from ensemble averages of Wilson loops with sufficiently large temporal extension. To get quantitative results for the linear part and the $1/R$-correction, one usually performs a fit with (3.3) to determine the parameters σ and α. This approach will be discussed in section 3.1.2.

In the second approach (c.f. section 3.1.1) one makes an assumption about the functional dependence of ensemble averages of Wilson loops, which has to fulfill the following necessary requirements:

- $\langle W_{(R,T)} \rangle \geq 0$ (c.f. (3.2)). For the following it is convenient to define $\langle W_{(R,T)} \rangle = e^{-F(R,T)}$.
- $\langle W_{(R,T)} \rangle = \langle W_{(T,R)} \rangle$ since in Euclidean spacetime there is no difference between space and time. This implies $F(R,T) = F(T,R)$.
- $\lim_{T\to\infty} F(R,T) = V_{\mathrm{q\bar{q}}}(R)T$ (c.f. (3.2)).

A possible but not unique candidate is

$$-\ln\Big\langle W_{(R,T)}\Big\rangle \;=\; F(R,T) \;=\; V_0\Big(R+T\Big) - \alpha\left(\frac{R}{T}+\frac{T}{R}\right) + \beta + \sigma RT \tag{3.4}$$

[16]. It is a simple and plausible choice, which is consistent with existing numerical results. This Wilson loop ansatz is fitted to Monte-Carlo data for $-\ln\langle W_{(R,T)}\rangle$, to determine the parameters V_0, α, β and σ.

Since (3.4) reproduces the quark antiquark potential (3.3) when inserted in (3.2), it is only trustworthy for sufficiently large R or T. Moreover, pseudoparticle ensembles are not able to reproduce physical properties for Wilson loops with spatial and temporal extension not significantly larger than the pseudoparticle size λ and the average distance between neighboring pseudoparticles $\bar{d} = 1/n^{1/4}$. The reason is that λ and $\bar{d}$ determine the minimal size of the ultraviolet fluctuations and, therefore, act as a cutoff. They play a similar role as the lattice spacing in lattice calculations (c.f. section 2.2.4). Therefore, in the pseudoparticle approach the ansatz (3.4) is only valid for $R, T \gtrsim \lambda, \bar{d}$.

Before we explain how to calculate V_0, α, β and σ in the pseudoparticle approach, we discuss some general properties of these parameters and review some lattice results:

- Lattice calculations yield a positive value of the string tension σ, which implies the presence of confinement (c.f. e.g. [5, 6, 15, 16]). Furthermore, σ is a monotonically increasing function of the coupling constant g. When the scale is set by the string tension, the physical extension of the lattice can be adjusted by choosing appropriate values for g.

- The Coulomb coefficient α is a dimensionless quantity, which is independent of the coupling constant. The bosonic string picture predicts $\alpha_{\text{string}} = \pi/12 \approx 0.26$ [18, 19]. In lattice calculations $\alpha_{\text{lattice}} \approx 0.22 \ldots 0.32$ has been observed [16, 17].
- V_0 and β are unphysical cutoff dependent constants. Since V_0 is a dimensionful quantity, it also depends on the coupling constant. V_0 and β contain information about the overlap between the ground state and a state containing a static quark antiquark pair at separation R connected by a Wilson line [16]. Lattice calculations yield $V_0 > 0$ and $\beta < 0$.

As will be shown in the following sections, we observe similar properties in the pseudoparticle approach.

3.1.1 Calculating the string tension σ and the Coulomb coefficient α

In the following we apply four different methods to determine the string tension, which are all based on the Wilson loop ansatz (3.4). Two of these methods are well known from literature, area perimeter fits [5] and Creutz ratios [6]. The other two are generalizations, which have been developed in the context of this work. With their help we are able to determine both the string tension and the Coulomb coefficient.

Whenever we use physical units, we have set the scale by identifying the numerical value of the string tension with the physical value $4.2/\text{fm}^2$.

3.1.1.1 Method 1: area perimeter fits

We consider ensemble averages of rectangular Wilson loops with $R/T = c =$ constant as functions of the area RT. The Wilson loop ansatz (3.4) reduces to an area perimeter function:

$$-\ln\Big\langle W_{(R,T)}\Big\rangle\Big|_{R/T=c} \;=\; F(R,T)\Big|_{R/T=c} \;=\; V_0\Big(R+T\Big)\underbrace{-\alpha\left(c+\frac{1}{c}\right)+\beta}_{=\tilde{\beta}}+\sigma RT \;=$$

$$=\; V_0\left(\sqrt{c}+\frac{1}{\sqrt{c}}\right)\sqrt{RT}+\tilde{\beta}+\sigma RT. \tag{3.5}$$

The parameters V_0, $\tilde{\beta}$ and σ are obtained by fitting this area perimeter function to Monte-Carlo data for $-\ln\langle W_{(R,T)}\rangle|_{R/T=c}$ (c.f. Appendix B.3).

Results: $\mathcal{AC}$-ensemble, $N = 400$, $n = 1.0$, $\lambda = 0.5$

Figure 3.1a shows $-\ln\langle W_{(R,T)}\rangle_{R/T=1/2}$ plotted against the area for different coupling constants $g \in \{1.0\ ,\ 2.0\ ,\ \ldots\ ,\ 5.0\}$ (the Wilson loops have been centered around the origin). All curves clearly exhibit an area law, which amounts to a positive value of the string tension σ. This in turn is an unambiguous sign of confinement. Furthermore, it is obvious from the figure that σ is an increasing function of the coupling constant.

We obtained numerical values for V_0, $\tilde{\beta}$ and σ by fitting (3.5) to the Monte-Carlo data of Figure 3.1a (c.f. Appendix B.3). For σ these values are shown in Figure 3.1b. To avoid cutoff

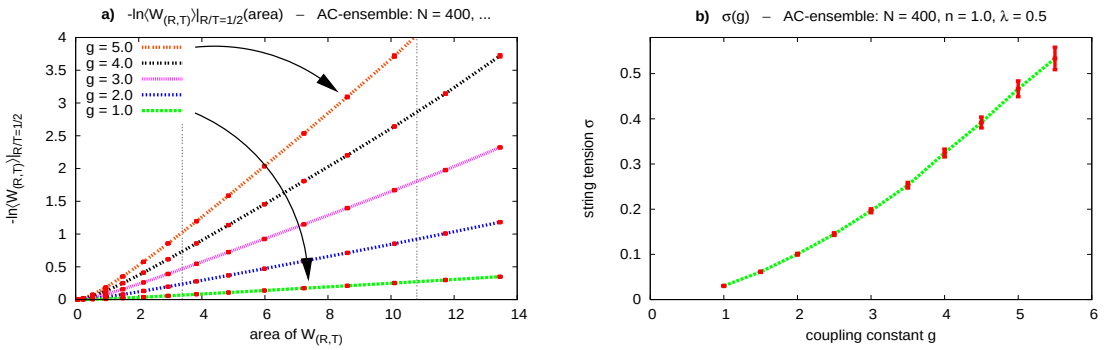

Figure 3.1: $\mathcal{AC}$-ensemble, $N = 400$, $n = 1.0$, $\lambda = 0.5$, for different coupling constants $g \in \{1.0\ ,\ 1.5\ ,\ \ldots\ ,\ 5.5\}$. **a)** $-\ln\langle W_{(R,T)}\rangle|_{R/T=1/2}$ plotted against the area. **b)** σ plotted against g.

effects, only Wilson loops with $R \geq d_{\text{cutoff}} = 1.3$ have been considered for the fitting. For $R/T = 1/2$ this corresponds to Wilson loop areas $RT \geq 3.38$. Likewise, we have discarded Wilson loops, which are not entirely inside a hypersphere of radius $r_{\text{boundary}} = 2.6$ to exclude boundary effects (c.f. section 2.3.2). For $R/T = 1/2$ this amounts to Wilson loop areas $RT \leq 10.82$. The interval $3.38 \leq RT \leq 10.82$ is indicated by the dashed gray lines in Figure 3.1a.

As already mentioned above, the numerical value of the string tension is identified with $4.2/\text{fm}^2$ and, therefore, determines the physical size of the spacetime hypersphere. From $g = 1.0$ to $g = 5.5$ its diameter ranges approximately between 0.5 fm and 2.1 fm.

To test the stability of this method, we considered different ratios R/T for $g = 4.0$. As before, $d_{\text{cutoff}} = 1.3$ and $r_{\text{boundary}} = 2.6$. Especially for small ratios R/T this leaves only a narrow window of permissable Wilson loop areas (c.f. Table 3.1). Figure 3.2a shows $-\ln\langle W_{(R,T)}\rangle|_{R/T=\text{constant}}$ as a function of the area for $R/T \in \{1.0/1.0\ ,\ 1.0/1.5\ ,\ \ldots\ ,\ 1.0/3.0\}$ (for the sake of clarity the curves have been shifted by suitably chosen constants). All curves exhibit approximately the same area law, although they correspond to different ratios R/T.

R/T	1.0/1.0	1.0/1.5	1.0/2.0	1.0/2.5	1.0/3.0
minimum Wilson loop area	1.69	2.54	3.38	4.23	5.07
maximum Wilson loop area	13.52	12.48	10.82	9.32	8.11

Table 3.1: minimum and maximum Wilson loop areas for $d_{\text{cutoff}} = 1.3$, $r_{\text{boundary}} = 2.6$ and different $R/T \in \{1.0/1.0\ ,\ 1.0/1.5\ ,\ \ldots\ ,\ 1.0/3.0\}$.

Figure 3.2b shows the string tension σ as a function of T/R. From $T/R = 1.0/1.0$ to $T/R = 3.0/1.0$ it varies between $\sigma = 0.25$ and $\sigma = 0.48$. This variation is probably due to a combination of cutoff and boundary effects, which have an especially strong influence on curves $-\ln\langle W_{(R,T)}\rangle|_{R/T=\text{constant}}$ with large values T/R. Both effects increase the curvature of $-\ln\langle W_{(R,T)}\rangle|_{R/T=\text{constant}}$. For cutoff effects this is obvious when considering

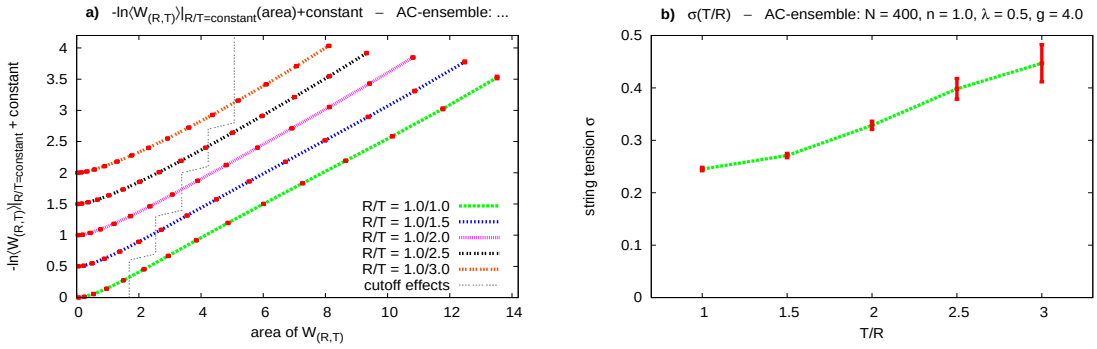

Figure 3.2: $\mathcal{AC}$-ensemble, $N = 400$, $n = 1.0$, $\lambda = 0.5$, $g = 4.0$. Different ratios $R/T \in \{1.0/1.0\ ,\ 1.0/1.5\ ,\ \ldots\ ,\ 1.0/3.0\}$. **a)** $-\ln\langle W_{(R,T)}\rangle|_{R/T=\text{constant}}+\text{constant}$ plotted against the area. **b)** σ plotted against T/R.

$-\ln\langle W_{(R,T)}\rangle|_{R/T=\text{constant}}$ for small areas (c.f. e.g. Figure 3.2a). In regions, where boundary effects become relevant, the absolute value of the gauge field is larger on the average than in regions without boundary effects (c.f. e.g. Figure 2.5). Due to the periodicity of the exponential function in (3.1) this will result in a smaller value of $\langle W_{(R,T)}\rangle|_{R/T=\text{constant}}$, i.e. for large Wilson loops we expect $-\ln\langle W_{(R,T)}\rangle|_{R/T=\text{constant}}$ to get an additional positive but unphysical contribution. This in turn increases the curvature. Therefore, cutoff and boundary effects give rise to a smaller or even negative perimeter coefficient V_0. Assuming that the slope is roughly the same for all values of R/T, which is confirmed by Figure 3.2a, this will result in a significantly larger string tension σ (c.f. (3.5)). To conclude, for $g = 4.0$ we expect the physical value of the string tension to be rather $\sigma \approx 0.20 \ldots 0.25$ instead of e.g. $\sigma \approx 0.45$ as obtained for $T/R = 3.0/1.0$. This result is in agreement with what we have obtained by other methods, which will be discussed in the following sections.

3.1.1.2 Method 2: Creutz ratios

Another method to determine the string tension from ensemble averages of rectangular Wilson loops is to consider Creutz ratios, which are defined by

$$C(R,T,a) \quad = \quad \frac{\Big\langle W_{(R,T)}\Big\rangle\Big\langle W_{(R-a,T-a)}\Big\rangle}{\Big\langle W_{(R-a,T)}\Big\rangle\Big\langle W_{(R,T-a)}\Big\rangle}, \tag{3.6}$$

where $a < R, T$ is an arbitrary length, usually much smaller than R and T (in lattice calculations a is the lattice spacing). When applying the Creutz ratio method, one usually makes the assumption that ensemble averages of rectangular Wilson loops can be parameterized by

$$\Big\langle W_{(R,T)}\Big\rangle \quad = \quad e^{-\tilde{F}(R,T)} \quad , \quad \tilde{F}(R,T) \quad = \quad V_0\Big(R+T\Big) + \beta + \sigma RT. \tag{3.7}$$

This leads to

$$C(R,T,a) \quad = \quad \exp(-\sigma a^2). \tag{3.8}$$

Note that (3.7) is merely a simplification of our previously discussed Wilson loop ansatz (3.4). Using the latter instead of (3.7) yields

$$C(R,T,a) \quad = \quad \exp\left(-\sigma a^2 - \alpha\left(\frac{a^2}{T(T-a)} + \frac{a^2}{R(R-a)}\right)\right). \tag{3.9}$$

In the limit $a/R, a/T \to 0$ (3.8) and (3.9) become identical.

Solving (3.8) for σ results in

$$\sigma \quad = \quad -\frac{\ln(C(R,T,a))}{a^2}. \tag{3.10}$$

In the presence of confinement σ should approach a finite constant at least for sufficiently large a/R and a/T, where the parameterization (3.7) is considered to be most trustworthy. This constant is the "true value" of the string tension.

To calculate Creutz ratios for a large set of different values (R,T), we resort to "Wilson loop grids", which are an efficient tool. An example is shown in Figure 3.3. The "links" of these grids are ordinary Wilson lines of length a. From the links of an $N \times N$-Wilson loop grid with spacing a we can calculate ensemble averages of rectangular Wilson loops $\langle W_{(R,T)} \rangle$ with $R,T \in \{a\ ,\ 2a\ ,\ \ldots\ ,\ Na\}$. In general, there are many possibilities to construct a Wilson loop of size (R,T). We average over all combinations. The advantage of this method is that every link contributes to several Wilson loops but has to be calculated only once, which in turn speeds up the computation significantly.

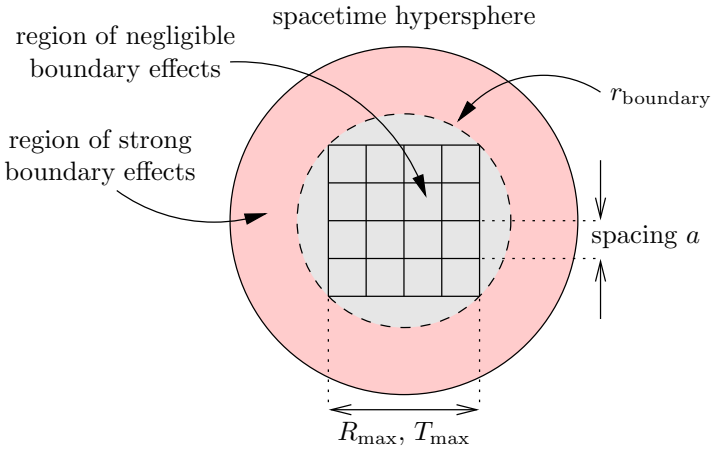

Figure 3.3: a 4×4-Wilson loop grid inside the spacetime hypersphere.

Results: $\mathcal{AC}$-ensemble, $N = 400$, $n = 1.0$, $\lambda = 0.5$, $g = 4.0$

We calculated Creutz ratios from 12×12-Wilson loop grids. Choosing $r_{\text{boundary}} = 2.6$ results in $R_{\text{max}} = T_{\text{max}} = \sqrt{2}\, r_{\text{boundary}} = 3.68$ and $a = R_{\text{max}}/12 = T_{\text{max}}/12 = 0.31$ (c.f. Figure 3.3).

Figure 3.4a shows different estimates for the string tension σ obtained from Creutz ratios via (3.10). Estimates calculated with the same T but different R are connected. The results indicate a positive value of the string tension, which in turn is a clear signal of confinement. The qualitative shape of

$$\sigma|_{T=\text{constant}} \quad = \quad -\frac{\ln(C(R,T,a))}{a^2}\bigg|_{T=\text{constant}} \tag{3.11}$$

as a function of RT is the same for all values of T. This shape can be explained as follows:

- For small values of RT the ensemble averages of Wilson loops, from which the Creutz ratios are calculated, are subject to strong cutoff effects. Therefore, we cannot trust these Creutz ratios when calculating the string tension. In Figure 3.4b we have discarded all estimates for the string tension, where Wilson loops with $R, T < d_{\text{cutoff}} = 1.3$ are involved.

- For large values of RT the ensemble averages of Wilson loops from which the Creutz ratios are calculated contain certain boundary effects, i.e. by choosing $r_{\text{boundary}} = 2.6$ we may have slightly overestimated the region where boundary effects are negligible. Therefore, in Figure 3.4b we have also discarded all estimates for the string tension, for which the corresponding curves $\sigma|_{T=\text{constant}}$ in Figure 3.4a are increasing again.

- All remaining estimates for the string tension are plotted in Figure 3.4b. The fact that the curves $\sigma(R, T = \text{constant})$ are decreasing for increasing R can be explained by a positive Coulomb coefficient α (c.f. (3.9)). This is a first indication that the pseudoparticle approach is not only able to reproduce the linear long range part of the quark antiquark potential but also its $1/R$-correction.

From Figure 3.4b we expect the string tension to be $\sigma \approx 0.20 \ldots 0.25$. This is in excellent agreement with the result obtained by area perimeter fits (c.f. section 3.1.1.1).

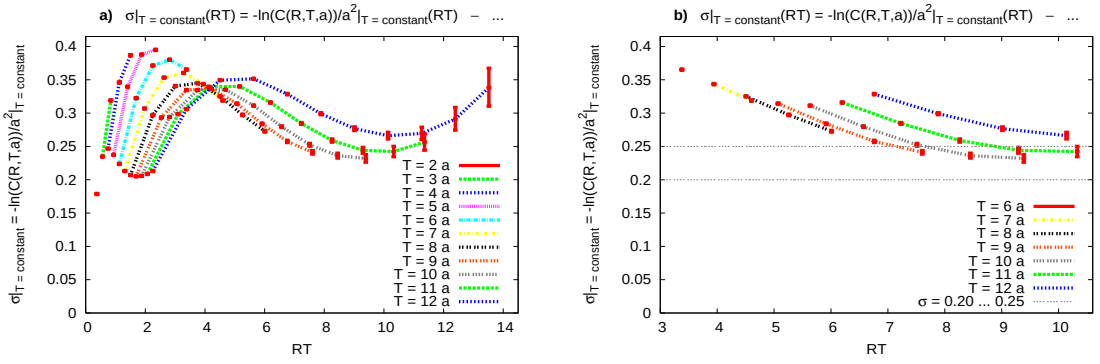

Figure 3.4: $\mathcal{AC}$-ensemble, $N = 400$, $n = 1.0$, $\lambda = 0.5$, $g = 4.0$. **a)** Estimates for σ obtained from Creutz ratios $C(R, T, a)$, $R \leq T$, via (3.10) plotted against RT for different $T \in \{2a\ ,\ 3a\ ,\ \ldots\ ,\ 12a\}$, $a = 0.31$. **b)** The same as a) but only "physically meaningful data points" are shown.

3.1.1.3 Method 3: generalized Creutz ratios

Generalized Creutz ratios are a natural extension of Creutz ratios.

The starting point is a set of ensemble averages of rectangular Wilson loops $\langle W_{(R,T)} \rangle$ with different ratios R/T:

$$\left\{ \left\langle W_{(R_1,T_1)} \right\rangle \, , \, \left\langle W_{(R_2,T_2)} \right\rangle \, , \, \ldots \, , \, \left\langle W_{(R_n,T_n)} \right\rangle \right\}. \tag{3.12}$$

Such a set can be obtained in an efficient way by resorting to Wilson loop grids (c.f. section 3.1.1.2).

A generalized Creutz ratio Γ_X is defined by

$$\begin{aligned} &\Gamma_X(R_{i_1}, T_{i_1}, \ldots, R_{i_4}, T_{i_4}) \quad = \\ &\quad = \quad \left\langle W_{(R_{i_1},T_{i_1})} \right\rangle^{c_{1,X}} \left\langle W_{(R_{i_2},T_{i_2})} \right\rangle^{c_{2,X}} \left\langle W_{(R_{i_3},T_{i_3})} \right\rangle^{c_{3,X}} \left\langle W_{(R_{i_4},T_{i_4})} \right\rangle^{c_{4,X}} \end{aligned} \tag{3.13}$$

with $X \in \{V_0, \alpha, \beta, \sigma\}$ and weights $c_{1,X} = c_{1,X}(R_{i_1}, T_{i_1}, \ldots, R_{i_4}, T_{i_4}), \ldots,$
$c_{4,X} = c_{4,X}(R_{i_1}, T_{i_1}, \ldots, R_{i_4}, T_{i_4})$, which will be specified below. Inserting the Wilson loop ansatz (3.4) and considering the negative logarithm yields

$$\begin{aligned} &- \ln \Big(\Gamma_X(R_{i_1}, T_{i_1}, \ldots, R_{i_4}, T_{i_4}) \Big) \quad = \\ &\quad = \quad V_0 \Big(c_{1,X} \Big(R_{i_1} + T_{i_1} \Big) + \ldots + c_{4,X} \Big(R_{i_4} + T_{i_4} \Big) \Big) + \\ &\qquad \alpha \Big(c_{1,X} \left(- \frac{R_{i_1}}{T_{i_1}} - \frac{T_{i_1}}{R_{i_1}} \right) + \ldots + c_{4,X} \left(- \frac{R_{i_4}}{T_{i_4}} - \frac{T_{i_4}}{R_{i_4}} \right) \Big) + \\ &\qquad \beta \Big(c_{1,X} + \ldots + c_{4,X} \Big) + \\ &\qquad \sigma \Big(c_{1,X} \Big(R_{i_1} T_{i_1} \Big) + \ldots + c_{4,X} \Big(R_{i_4} T_{i_4} \Big) \Big). \end{aligned} \tag{3.14}$$

The weights $c_{1,X}, \ldots, c_{4,X}$ are chosen so that (3.14) reduces to

$$- \ln \Big(\Gamma_X(R_{i_1}, T_{i_1}, \ldots, R_{i_4}, T_{i_4}) \Big) \quad = \quad X. \tag{3.15}$$

That is $c_{1,X}, \ldots, c_{4,X}$ can be obtained by solving the following linear system:

$$\begin{aligned} &\begin{pmatrix} R_{i_1} + T_{i_1} & \ldots & R_{i_4} + T_{i_4} \\ -R_{i_1}/T_{i_1} - T_{i_1}/R_{i_1} & \ldots & -R_{i_4}/T_{i_4} - T_{i_4}/R_{i_4} \\ 1 & \ldots & 1 \\ R_{i_1} T_{i_1} & \ldots & R_{i_4} T_{i_4} \end{pmatrix} \begin{pmatrix} c_{1,V_0} & c_{1,\alpha} & c_{1,\beta} & c_{1,\sigma} \\ c_{2,V_0} & c_{2,\alpha} & c_{2,\beta} & c_{2,\sigma} \\ c_{3,V_0} & c_{3,\alpha} & c_{3,\beta} & c_{3,\sigma} \\ c_{4,V_0} & c_{4,\alpha} & c_{4,\beta} & c_{4,\sigma} \end{pmatrix} \quad = \\ &\quad = \quad \begin{pmatrix} 1 & 0 & 0 & 0 \\ 0 & 1 & 0 & 0 \\ 0 & 0 & 1 & 0 \\ 0 & 0 & 0 & 1 \end{pmatrix}. \end{aligned} \tag{3.16}$$

To determine V_0, α, β and σ, we consider all subsets of (3.12) containing four elements with exception of those, for which the left matrix in (3.16) is singular. For every subset we calculate V_0, α, β and σ via (3.15). Although there will be fluctuations due to systematical and statistical errors, most of these estimates should be similar.

There is numerical evidence that estimates for V_0, α, β and σ with large $c_{1,X}^2 + \ldots + c_{4,X}^2$ exhibit stronger fluctuations than estimates with small $c_{1,X}^2 + \ldots + c_{4,X}^2$ (c.f. e.g. Figure 3.5). Therefore, we sort the estimates according to $c_{1,X}^2 + \ldots + c_{4,X}^2$ and keep only the "smaller half". The average of these remaining estimates is the final result for V_0, α, β or σ.

Results: $\mathcal{S}^{12}$-ensemble, $N = 35 \times 12$, $n = 1.0$, $\lambda = 0.5$

We calculated ensemble averages of rectangular Wilson loops $\langle W_{(R,T)} \rangle$ by considering 12×12-Wilson loop grids with $r_{\text{boundary}} = 2.0$. This corresponds to $R_{\max} = T_{\max} = \sqrt{2} r_{\text{boundary}} = 2.83$ and $a = R_{\max}/12 = T_{\max}/12 = 0.24$ (c.f. Figure 3.3).

We determined all possible generalized Creutz ratios $\Gamma_X(R_1, \ldots, T_4)$ with $R_1, \ldots, T_4 \in \{7a\ ,\ 8a\ ,\ \ldots\ ,\ 12a\}$. This amounts to a minimum spatial or temporal Wilson loop extension of 1.65. In total, there are 5877 generalized Creutz ratios for each of the quantities V_0, α, β and σ.

In Figure 3.5 the corresponding estimates for σ and α are plotted for $g = 4.0$. These estimates have been sorted according to $c_{1,X}^2 + \ldots + c_{4,X}^2$ and are shown in increasing order from left to right (for the sake of clarity only every tenth estimate is shown). In both plots estimates in the left half clearly exhibit a smaller variance than estimates in the right half. This indicates that estimates with small $c_{1,X}^2 + \ldots + c_{4,X}^2$ are more trustworthy than estimates with large $c_{1,X}^2 + \ldots + c_{4,X}^2$. Since for both σ and α all estimates exhibit similar values, we can extract reliable and consistent values by calculating the average and the standard deviation from the "smaller half". The results are $\sigma = 0.268 \pm 0.015$ and $\alpha = 0.151 \pm 0.023$.

By proceeding in the same way, we obtained numerical results for σ and α for different coupling constants $g \in \{2.0\ ,\ 2.5\ ,\ \ldots\ ,\ 5.5\}$.

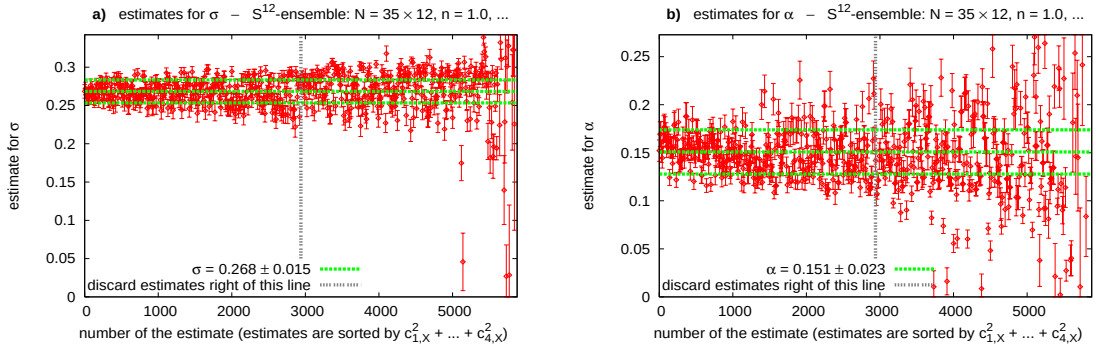

Figure 3.5: $\mathcal{S}^{12}$-ensemble, $N = 35 \times 12$, $n = 1.0$, $\lambda = 0.5$, $g = 4.0$. **a)** Estimates for σ sorted according to $c_{1,X}^2 + \ldots + c_{4,X}^2$. **b)** Estimates for α sorted according to $c_{1,X}^2 + \ldots + c_{4,X}^2$.

In Figure 3.6a the string tension σ is plotted against the coupling constant g. σ is not only positive but also an increasing function of g. This is precisely what one would expect to be the case for the string tension.

Figure 3.6b shows the Coulomb coefficient α as a function of the coupling constant g. For large g the value of α is of the right order of magnitude when compared to lattice results, while for small coupling constants its value is too small. Furthermore, α is not a constant with respect to g as a dimensionless quantity should be. On the other hand, this is hardly surprising. Lattice calculations indicate that the $1/R$-correction to the potential as predicted by the bosonic string picture sets in for quark antiquark separations around 0.5 fm. But for $g = 2.0$ we have considered Wilson loops with temporal and spatial extensions between 0.23 fm and 0.40 fm. From such Wilson loops it is impossible to determine the correct coefficient of the $1/R$-correction of the potential. Increasing the coupling constant increases the size of the Wilson loops until for $g = 5.5$ their extension ranges between 0.55 fm and 0.95 fm. As already mentioned, from these Wilson loops we obtained results, which are in qualitative agreement with lattice results.

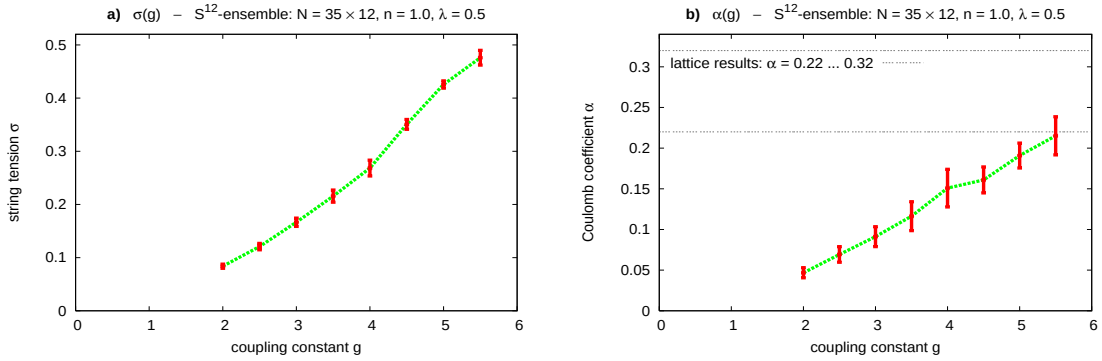

Figure 3.6: $\mathcal{S}^{12}$-ensemble, $N = 35 \times 12$, $n = 1.0$, $\lambda = 0.5$. **a)** σ plotted against g. **b)** α plotted against g.

3.1.1.4 Method 4: fitting the Wilson loop ansatz to $-\ln\langle W_{(R,T)}\rangle$

Instead of resorting to generalized Creutz ratios to determine the string tension σ and the Coulomb coefficient α, we can as well perform a least squares fit of the Wilson loop ansatz (3.4) to Monte-Carlo data for $-\ln\langle W_{(R,T)}\rangle$ (c.f. Appendix B.3). Different ratios R/T are required.

Results: $\mathcal{S}^{12}$-ensemble, $N = 35 \times 12$, $n = 1.0$, $\lambda = 0.5$

We applied the same Monte-Carlo data for the fitting procedure as we considered to produce the generalized Creutz ratios results of Figure 3.5 and 3.6: $-\ln\langle W_{(R,T)}\rangle$ with
$R, T \in \{7a\ ,\ 8a\ ,\ \ldots\ ,\ 12a\}$, $a = 0.24$.

In Figure 3.7 the least squares fit of the Wilson loop ansatz (3.4) to Monte-Carlo data for $-\ln\langle W_{(R,T)}\rangle$ is shown for $g = 4.0$. The ansatz is consistent with pseudoparticle results.

In Figure 3.8 σ and α obtained by least squares fitting as well as σ and α obtained from

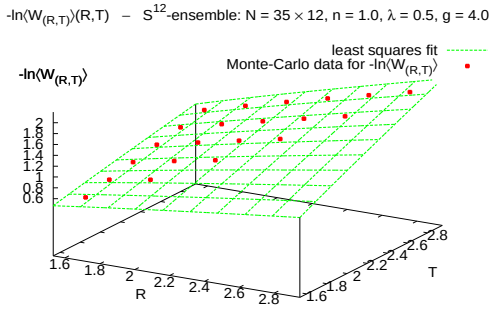

Figure 3.7: $\mathcal{S}^{12}$-ensemble, $N = 35 \times 12$, $n = 1.0$, $\lambda = 0.5$, $g = 4.0$. The least squares fit of the Wilson loop ansatz (3.4) to Monte-Carlo data for $-\ln\langle W_{(R,T)}\rangle$ plotted against R and T.

generalized Creutz ratios are plotted against the coupling constant. The results of both methods are identical within statistical errors.

3.1.1.5 Comparison of method 1 to 4

We have four methods at our disposal to determine the string tension. Two of them are also capable of extracting the Coulomb coefficient. All four methods produce similar results. Nevertheless, generalized Creutz ratios have a couple of advantages compared to the other three methods:

- Generalized Creutz ratios can be used to determine the string tension and the Coulomb coefficient, whereas area perimeter fits and Creutz ratios only yield the string tension.
- Generalized Creutz ratios are well suited to detect systematic errors, i.e. inconsistencies

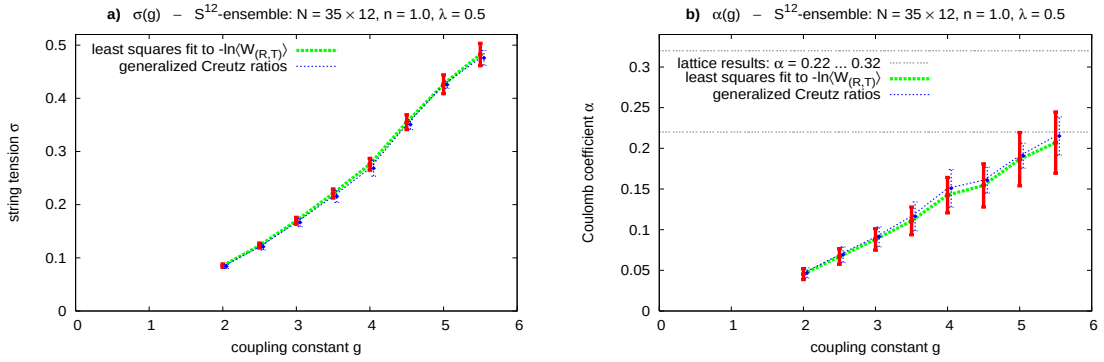

Figure 3.8: $\mathcal{S}^{12}$-ensemble, $N = 35 \times 12$, $n = 1.0$, $\lambda = 0.5$, for different coupling constants $g \in \{2.0\ ,\ 2.5\ ,\ \ldots\ ,\ 5.5\}$. **a)** σ obtained by least squares fitting and σ obtained from generalized Creutz ratios plotted against g. **b)** α obtained by least squares fitting and α obtained from generalized Creutz ratios plotted against g.

between the Wilson loop ansatz (3.4) and Monte-Carlo data for $\langle W_{(R,T)} \rangle$. One just has to take a look at plots like Figure 3.5 and check whether all estimates are similar or not. The other methods yield comparable results but it is not obvious how trustworthy these results are.

- In contrast to Creutz ratios, the Coulomb term is eliminated when calculating the string tension via generalized Creutz ratios.

3.1.2 Calculating the static quark antiquark potential

The starting point to calculate the static quark antiquark potential is (3.2), which we write as

$$V_{q\bar{q}}(R)T \quad \approx \quad -\ln\left\langle W_{(R,T)} \right\rangle. \tag{3.17}$$

We calculate ensemble averages of Wilson loops $\langle W_{(R,T)} \rangle$ for fixed R but different T to obtain a curve $-\ln\langle W_{(R=\text{constant},T)} \rangle$. Examples are shown in Figure 3.9a. According to (3.17) such a curve will exhibit a linear behavior for sufficiently large T. From the slope, which we obtain by

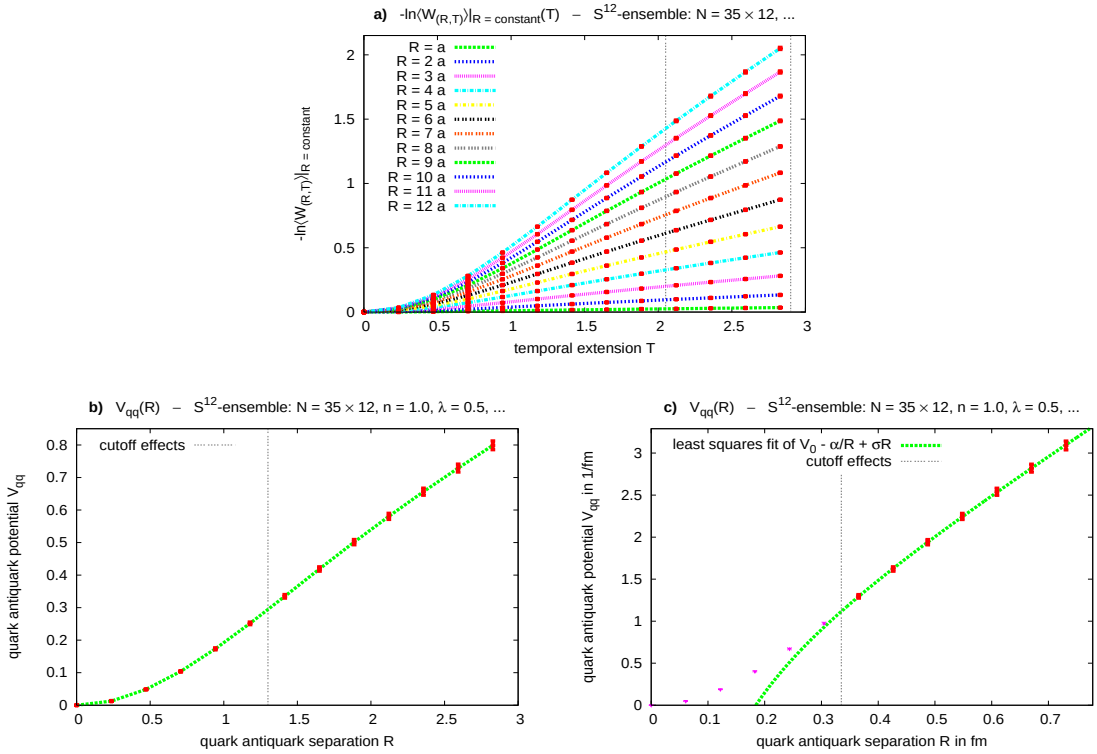

Figure 3.9: $\mathcal{S}^{12}$-ensemble, $N = 35 \times 12$, $n = 1.0$, $\lambda = 0.5$, $g = 4.0$. **a)** $-\ln\langle W_{(R,T)} \rangle|_{R=\text{constant}}$ plotted against T for different $R \in \{a\ ,\ 2a\ ,\ \ldots\ ,\ 12a\}$, $a = 0.24$. **b)** $V_{q\bar{q}}$ plotted against the separation of the quarks. **c)** $V_0 - \alpha/R + \sigma R$ fitted to the data of b) (only the red data points have been included in the fitting procedure). The axes have been rescaled to physical units by identifying σ with $4.2/\text{fm}^2$.

fitting a straight line (c.f. Appendix B.3), we can read off $V_{q\bar{q}}(R)$. Iterating this procedure for a number of different R yields an approximation of the quark antiquark potential.

Results: $\mathcal{S}^{12}$-ensemble, $N = 35 \times 12$, $n = 1.0$, $\lambda = 0.5$, $g = 4.0$

We calculated ensemble averages of Wilson loops from 12×12-Wilson loop grids with $r_{\text{boundary}} = 2.0$. This corresponds to $R_{\max} = T_{\max} = \sqrt{2}\, r_{\text{boundary}} = 2.83$ and $a = R_{\max}/12 = T_{\max}/12 = 0.24$ (c.f. Figure 3.3).

Figure 3.9a shows $-\ln\langle W_{(R=\text{constant},T)}\rangle$ as a function of T for different $R \in \{a\ ,\ 2a\ ,\ \ldots\ ,\ 12a\}$. To determine the slope of these curves for large T we fitted straight lines to the data points at $T \in \{9a\ ,\ 10a\ ,\ 11a\ ,\ 12a\}$ as indicated by the dashed gray lines.

The corresponding potential as a function of the quark antiquark separation is plotted in Figure 3.9b. For large separations it clearly exhibits a linear behavior.

To obtain numerical values for the string tension σ and the Coulomb coefficient α, we performed a least squares fit of the potential parameterization (3.3) to the data points from Figure 3.9b (c.f. Appendix B.3). Only data points with $R \geq 1.3$ have been considered, because cutoff effects are expected to render the potential unphysical for smaller separations. The results, $\sigma = 0.281 \pm 0.019$ and $\alpha = 0.198 \pm 0.068$, are in agreement with the results obtained by generalized Creutz ratios (c.f. section 3.1.1.3). The fit is shown in Figure 3.9c. The axes have been rescaled to physical units by identifying σ with $4.2/\text{fm}^2$.

Note that we did not make any assumptions about the functional dependence of ensemble averages of Wilson loops to calculate the quark antiquark potential. Therefore, the agreement of the results for σ and α with results obtained by generalized Creutz ratios shows again the consistency of the Wilson loop ansatz (3.4) and Monte-Carlo data for $\langle W_{(R,T)}\rangle$.

3.2 The topological susceptibility

In order to produce quantitative results involving the string tension, we need other dimensionful quantities so that we can consider dimensionless ratios. One such quantity, which has been studied extensively on the lattice (c.f. e.g. [22, 23, 24, 25]), is the topological susceptibility χ. The topological susceptibility is closely related to the mass of the η' meson [26]. It is defined by

$$\chi \;=\; \lim_{V\to\infty} \frac{1}{V}\left\langle Q_V^2 \right\rangle, \tag{3.18}$$

where Q_V is the topological charge inside the spacetime volume V.

In our numerical calculations we approximate the limit $V \to \infty$ by a large but finite volume. To be more specific, we consider a hyperspherical spacetime region with radius r_{boundary}, which is centered inside the spacetime hypersphere (c.f. Figure 2.2). To assure that this volume is sufficiently large, we evaluate $\langle Q_V^2\rangle/V$ for several smaller hyperspherical spacetime regions. A typical example, an $\mathcal{AC}$-ensemble with $N = 400$, $n = 1.0$, $\lambda = 0.5$ and $g = 4.0$, is shown in Figure 3.10. $\chi^{1/4} = (\langle Q_V^2\rangle/V)^{1/4}$, which we will ultimately consider to calculate the dimensionless ratio $\chi^{1/4}/\sigma^{1/2}$, seems to have converged to a stable value for $V \gtrsim 12.0$, which corresponds to $r_{\text{boundary}} \gtrsim 1.25$.

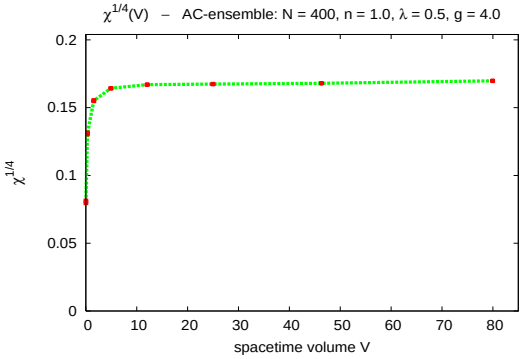

Figure 3.10: $\mathcal{AC}$-ensemble, $N = 400$, $n = 1.0$, $\lambda = 0.5$, $g = 4.0$. $\chi^{1/4} = (\langle Q_V^2 \rangle / V)^{1/4}$ plotted against V.

Results: $\mathcal{AC}$-ensemble, $N = 400$, $n = 1.0$, $\lambda = 0.5$, and $\mathcal{S}^{12}$-ensemble, $N = 35 \times 12$, $n = 1.0$, $\lambda = 0.5$

Figure 3.11 shows the dimensionless ratio $\chi^{1/4}/\sigma^{1/2}$ as a function of the coupling constant g for the following two ensembles:

- $\mathcal{AC}$-ensemble, $N = 400$, $n = 1.0$, $\lambda = 0.5$: $r_{\text{boundary}} = 2.0$, σ has been obtained by area perimeter fits (c.f. Figure 3.1b).
- $\mathcal{S}^{12}$-ensemble, $N = 35 \times 12$, $n = 1.0$, $\lambda = 0.5$: $r_{\text{boundary}} = 2.0$, σ has been obtained by generalized Creutz ratios (c.f. Figure 3.6a).

As expected $\chi^{1/4}/\sigma^{1/2}$ is nearly independent of g, i.e. the string tension and the topological susceptibility exhibit consistent scaling behaviors with respect to the coupling constant. This success strongly indicates that sensible physics can be extracted from the pseudoparticle approach. The values for both ensembles, $\chi^{1/4}/\sigma^{1/2} = 0.29 \ldots 0.31$ ($\mathcal{AC}$-ensemble) and

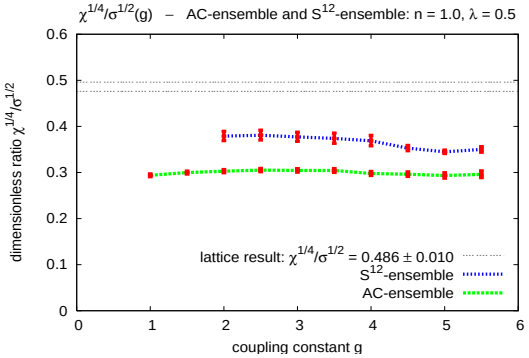

Figure 3.11: $\mathcal{AC}$-ensemble, $N = 400$, $n = 1.0$, $\lambda = 0.5$, and $\mathcal{S}^{12}$-ensemble, $N = 35 \times 12$, $n = 1.0$, $\lambda = 0.5$. $\chi^{1/4}/\sigma^{1/2}$ plotted against g.

$\chi^{1/4}/\sigma^{1/2} = 0.34 \ldots 0.39$ ($\mathcal{S}^{12}$-ensemble), are in qualitative agreement with the lattice result $\chi^{1/4}_{\text{lattice}}/\sigma^{1/2}_{\text{lattice}} = 0.486 \pm 0.010$ [27]. The discrepancy between the two pseudoparticle results is partly due to fact that $\mathcal{S}^{12}$-ensembles exhibit larger values for the topological susceptibility than $\mathcal{AC}$-ensembles (c.f. section 2.5), and partly because different methods have been applied to determine the string tension.

3.3 The critical temperature of the confinement deconfinement phase transition

Whereas at low temperature quarks are bound to each other by the mechanism of confinement, at high temperature a deconfining phase is expected. In this phase one can observe isolated quarks. The temperature, at which the corresponding phase transition takes place, is called critical temperature and denoted by T_{critical}. In this section we explain how to calculate this quantity in the pseudoparticle approach.

3.3.1 The pseudoparticle approach in finite temperature SU(2) Yang-Mills theory

In finite temperature SU(2) Yang-Mills theory thermodynamic expectation values of quantities $\mathcal{O}$ at temperature $T = 1/\beta$ are given by

$$\left\langle \mathcal{O} \right\rangle_\beta \;=\; \text{Tr}\left(e^{-\beta H} \mathcal{O} \right) \;=\; \frac{1}{Z} \int DA\, \mathcal{O}[A] e^{-S_\beta[A]} \quad , \quad Z \;=\; \int DA\, e^{-S_\beta[A]}, \tag{3.19}$$

where

$$S_\beta[A] \;=\; \int_0^\beta dx_0 \int d^3x \left(\frac{1}{4g^2} F^a_{\mu\nu} F^a_{\mu\nu} \right). \tag{3.20}$$

$\int DA$ is an integration over all gauge fields which are periodic in x_0-direction with period β.

3.3.1.1 Periodic pseudoparticles

Since in finite temperature calculations the gauge field is periodic, we need a method to make our building blocks periodic as well. For singular gauge instantons this has already been done in form of calorons [28, 29], which are periodic solutions to the classical Yang-Mills equations of motion. However, there is no straightforward generalization to arbitrary pseudoparticles. Therefore, we introduce a different method, which resorts to a blending technique from computer aided geometric design [30]. Note that in general the resulting periodic pseudoparticles are no solutions to the classical Yang-Mills equations of motion.

To begin with, we define blending functions B and $\overline{B}$:

$$B(\lambda) \;=\; -2\lambda^3 + 3\lambda^2 \quad , \quad \overline{B}(\lambda) \;=\; 1 - B(\lambda) \tag{3.21}$$

(c.f. Figure 3.12b). These blending functions have the following properties:

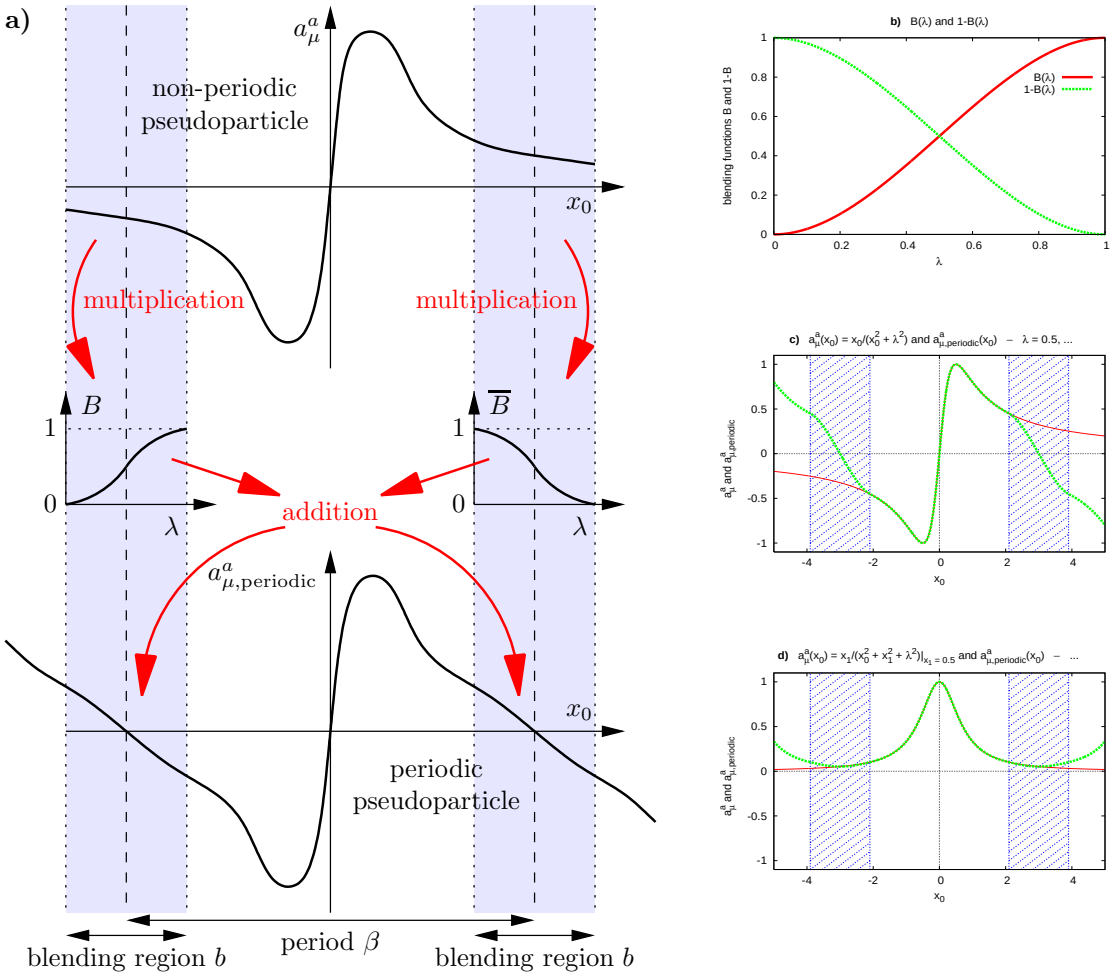

Figure 3.12: **a)** The basic principle of the blending method. **b)** B and $\overline{B} = 1 - B$ plotted against λ. **c)** $a^a_\mu = x_0/(x_0^2 + \lambda^2)$ and $a^a_{\mu,\text{periodic}}$ plotted against x_0 ($\lambda = 0.5$, $\beta = 6.0$, $b = 0.3 \times \beta$; the blending region is hatched in blue). **d)** $a^a_\mu = x_1/(x_0^2 + x_1^2 + \lambda^2)|_{x_1=0.5}$ and $a^a_{\mu,\text{periodic}}$ plotted against x_0 ($\lambda = 0.5$, $\beta = 6.0$, $b = 0.3 \times \beta$; the blending region is hatched in blue).

- C^1-continuity: B and $\overline{B}$ form smooth, C^1-continuous connections between 0 at $\lambda = 0$ and 1 at $\lambda = 1$ and vice versa.
- Partition of 1: $B(\lambda) + \overline{B}(\lambda) = 1$, i.e. B and $\overline{B}$ are suitable weight functions.
- Reflection symmetry: $\overline{B}(\lambda) = B(1-\lambda)$, i.e. reflection at $\lambda = 1/2$ transforms B into $\overline{B}$ and vice versa.

Of course the blending functions are not uniquely defined by these three requirements. Other reasonable definitions of blending functions exist, e.g. degree-5-polynomials, which can be chosen to form C^2-continuous connections between 0 and 1. However, numerical experiments have shown that physical results are fairly independent of the concrete choice of B and $\overline{B}$.

To make a non-periodic pseudoparticle a^a_μ with its center at the origin periodic in x_0-direction,

we multiply "both ends" with blending functions and add the results (c.f. Figure 3.12a):

$$a^a_{\mu,\text{periodic}}(x) \quad = \quad \begin{cases} a^a_\mu(x_0,\mathbf{x}) & \text{if} \quad -\frac{\beta-b}{2} \le x_0 \le \frac{\beta-b}{2} \\ B(\lambda)a^a_\mu(x_0-\beta,\mathbf{x}) + \overline{B}(\lambda)a^a_\mu(x_0,\mathbf{x}) & \text{if} \quad \frac{\beta-b}{2} \le x_0 \le \frac{\beta+b}{2} \end{cases}, \tag{3.22}$$

where

$$\lambda \quad = \quad \frac{x_0-(\beta-b)/2}{b}. \tag{3.23}$$

To evaluate $a^a_{\mu,\text{periodic}}$ at $(x_0,\mathbf{x})$ with $x_0 \notin [-(\beta-b)/2,(\beta+b)/2]$ one just has to combine (3.22) and

$$a^a_{\mu,\text{periodic}}(x_0,\mathbf{x}) = a^a_{\mu,\text{periodic}}(x_0+n\beta,\mathbf{x}) \tag{3.24}$$

with a suitably chosen integer n. b is the width of the blending region. In our numerical calculations we chose $b=\mathcal{B}\beta$ with a β-independent blending factor $\mathcal{B}=0.3$.

Two examples of periodic functions, which were generated by our blending technique, are shown in Figure 3.12c and 3.12d. These periodic functions are typical pseudoparticle profiles in x_0-direction.

3.3.1.2 The spacetime region

In zero temperature calculations spacetime is bounded by a 4-dimensional hypersphere. At finite temperature that region is replaced by a spacetime with a periodic time direction of extension β and a spatial part, which is bounded by an ordinary 3-dimensional sphere of radius r_{space} (c.f. Figure 3.13). As in the zero temperature case, we have to assure that samples of physically

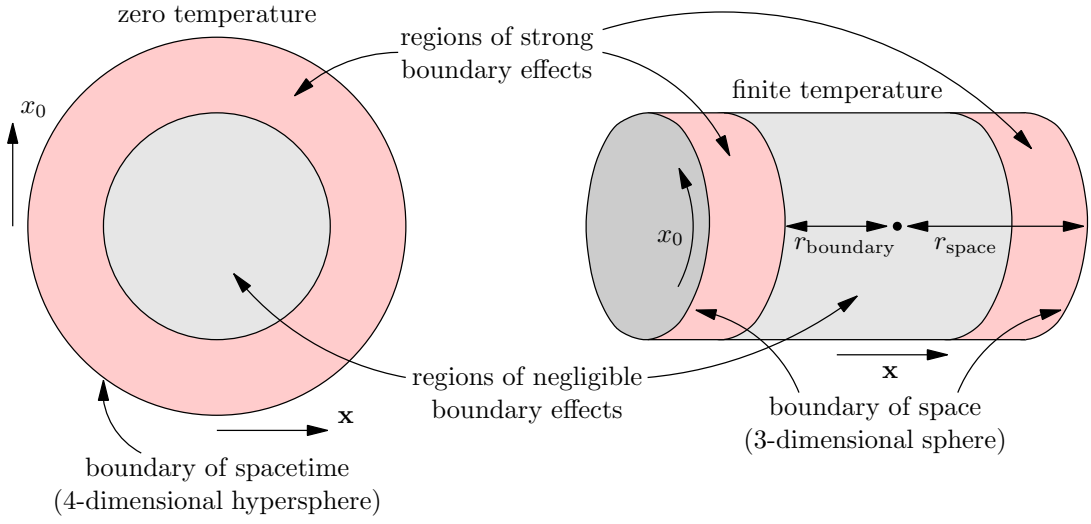

Figure 3.13: spacetime at zero temperature and at finite temperature.

meaningful quantities are always taken inside a spacetime region, where boundary effects are negligible. The spatial part of such a region is the interior of a sphere of radius r_{boundary}, whereas the time direction is not restricted (the light gray region in the right part of Figure 3.13).

3.3.1.3 The pseudoparticle density

For finite temperature calculations we use the same pseudoparticle density as for the corresponding zero temperature calculation (we always perform a corresponding zero temperature calculation with identical parameters to obtain the string tension, which is used to set the scale). This is a reasonable choice, because in the limit $\beta \to \infty$, $r_{\text{space}} \to \infty$ and $r_{\text{spacetime}} \to \infty$ finite temperature ensembles and zero temperature ensembles become identical.

Furthermore, there is a close analogy to lattice calculations. To set the scale, a zero temperature calculation with the same number of lattice sites in all four spacetime directions is carried out. For finite temperature calculations the number of lattice sites in the temporal direction is significantly reduced. However, since the lattice spacing remains unchanged, the density of lattice sites is still the same, i.e. a smaller number of link variables in a smaller spacetime volume.

The pseudoparticle approach offers two possibilities to change the temperature:

- Varying β while the coupling constant g is kept constant changes the physical temperature directly.
- Varying the coupling constant g (while β is kept constant) changes the numerical value of the string tension σ. This leads to a different physical extension of the periodic time direction and, therefore, alters the physical temperature.

We applied both methods and obtained results, which are in excellent agreement (c.f. Figure 3.14c).

3.3.2 The ensemble average of the Polyakov loop as order parameter

A Polyakov loop is a Wilson loop around the periodic x_0-direction:

$$L_{\mathbf{z}}[A] \;=\; \frac{1}{2}\mathrm{Tr}\left(P\left\{\exp\left(i\oint dz_0\, A_0(z)\right)\right\}\right). \tag{3.25}$$

Due to spatial translational invariance $\langle L_{\mathbf{z}}\rangle_\beta$ is $\mathbf{z}$-independent. Therefore, from a numerical point of view it is convenient to consider spatial averages of Polyakov loops. We define

$$\Big\langle L\Big\rangle_\beta \;=\; \left\langle \frac{1}{V}\int_V d^3z\, L_{\mathbf{z}}\right\rangle_\beta. \tag{3.26}$$

It can be shown that $\langle L\rangle_\beta$ is an order parameter, which indicates whether there is confinement or not [13, 31]:

$$\Big\langle L\Big\rangle_\beta \;=\; 0 \quad\leftrightarrow\quad \text{Confinement} \tag{3.27}$$

$$\Big\langle L\Big\rangle_\beta \;\neq\; 0 \quad\leftrightarrow\quad \text{Deconfinement.} \tag{3.28}$$

This criterion is closely related to center symmetry, which is spontaneously broken in the deconfinement phase. The temperature, at which the symmetry breaking takes place, is called critical temperature and denoted by T_{critical}.

In the center symmetric phase of SU(2) Yang-Mills theory for every field configuration $A_\mu^{a,+}$ there is a corresponding field configuration $A_\mu^{a,-}$ with $L_{\mathbf{z}}[A^+] = -L_{\mathbf{z}}[A^-]$, which is physically equivalent. In particular, both field configurations have the same action: $S[A^+] = S[A^-]$. $\langle L \rangle_\beta = 0$ follows immediately.

The spontaneous breakdown of center symmetry at $T = T_{\text{critical}}$ comes along with a splitting of the Hilbert space of states $\mathcal{H}$ in two independent spaces $\mathcal{H}^+$ and $\mathcal{H}^-$: $\mathcal{H} \to \mathcal{H}^+ \oplus \mathcal{H}^-$. The same applies for the set of field configurations considered in the path integral. Whereas in the center symmetric phase the integration extends over the set of all field configurations $\mathcal{A}$, in the broken phase this set is split in two, $\mathcal{A} \to \mathcal{A}^+ \oplus \mathcal{A}^-$, and the path integral is restricted to either $\mathcal{A}^+$ or $\mathcal{A}^-$. For $T > T_{\text{critical}}$ the above field configurations $A_\mu^{a,+}$ and $A_\mu^{a,-}$ split up: $A_\mu^{a,+} \in \mathcal{A}^+$ and $A_\mu^{a,-} \in \mathcal{A}^-$ or vice versa. The ensemble average of the Polyakov loop depends on which Hilbert space was chosen during the spontaneous breakdown of center symmetry: $\langle L \rangle_{\beta,\mathcal{H}^+} = +\overline{l}$ and $\langle L \rangle_{\beta,\mathcal{H}^-} = -\overline{l}$.

In the broken phase two field configurations, which are related by center symmetry, cannot be connected continuously by a set of field configurations of finite action. This implies that during a Monte-Carlo simulation only field configurations either from $\mathcal{A}^+$ or from $\mathcal{A}^-$ are generated, assuming an infinite system and a local and continuous update mechanism. In numerical calculations these assumptions are only approximately fulfilled. Nevertheless, one can at least expect that there are long sequences of steps, where only field configurations corresponding to one of the two Hilbert spaces are generated. This has been observed in lattice Monte-Carlo simulations (c.f. e.g. [31, 32]). Therefore, it is possible to measure the ensemble average of the Polyakov loop numerically.

Since our pseudoparticle ensembles are finite systems, which are only approximately center symmetric, and due to a certain bias discussed in the following paragraphs, one cannot expect an exact phase transition. Instead $\langle L \rangle_\beta \approx 0$ can be observed well below the critical temperature. For $\beta \approx \beta_{\text{critical}}$ the ensemble average of the Polyakov loop quickly rises to a non-zero value. For high temperatures $\langle L \rangle_\beta \approx 1$ (c.f. Figure 3.14a). Therefore, we define the critical temperature T_{critical} (or equivalently its inverse β_{critical}) to be that temperature, where the ensemble average of the Polyakov loop crosses a certain value ξ, e.g. $\xi = 0.5$:

$$\Big\langle L \Big\rangle_{\beta_{\text{critical}}} \quad = \quad \xi. \tag{3.29}$$

$\langle L \rangle_\beta$ in the pseudoparticle approach versus $\langle L \rangle_\beta$ in lattice calculations

The main difference between our results and lattice results is that even in the deconfinement phase we have never observed $\langle L \rangle_\beta < 0$. We conclude that in the pseudoparticle approach the low action field configurations corresponding to $\mathcal{H}^-$ are underrepresented, i.e. there are more low action field configurations corresponding to $\mathcal{H}^+$ than to $\mathcal{H}^-$. This bias always forces the system to chose the Hilbert space $\mathcal{H}_+$ when undergoing a spontaneous symmetry breakdown.

The bias can be explained by the following qualitative argument: for field configurations close to zero $L_{\mathbf{z}} \approx 1$ (c.f. (3.25)). Therefore, we expect these field configurations to be elements of

$\mathcal{A}^+$. Furthermore, all of these field configurations are low action field configurations, which contribute significantly to the path integral, since their exponential damping factors e^{-S} are close to 1. The set of these field configurations is denoted by $\mathcal{A}_{A\approx 0}$. Loosely speaking, all other low action field configurations are large enough so that $L_{\mathbf{z}}$ can pick up exponents, which are significantly different from zero. They are either elements of $\mathcal{A}^+$ or of $\mathcal{A}^-$. The set of these field configurations is denoted by $\mathcal{A}_{A\gg 0}$. However, there is numerical evidence that in the pseudoparticle approach with around 400 pseudoparticles most low action field configurations have small gauge fields, i.e. are elements of $\mathcal{A}_{A\approx 0}$. This is closely related to the fact that our ensembles are only approximately gauge invariant: a gauge transformed field configuration from $\mathcal{A}_{A\approx 0}$, which is a field configuration in $\mathcal{A}_{A\gg 0}$, can only be approximated when using around 400 pseudoparticles; such an approximation usually has a higher action. Therefore, there are proportionally more field configurations in $\mathcal{A}_{A\approx 0}$ than in $\mathcal{A}_{A\gg 0}$. This is manifested in form of a bias.

Results: $\mathcal{AC}$-ensemble, $n = 1.0$, $\lambda = 0.5$

In Figure 3.14a the ensemble average of the Polyakov loop $\langle L\rangle_\beta$ is plotted against the temperature T for different coupling constants $g \in \{4.0\ ,\ 5.0\ ,\ \ldots\ ,\ 8.0\}$ ($r_{\text{space}} = 3.0$, $r_{\text{boundary}} = 1.0$). The dashed gray lines correspond to a determination of the critical temperature T_{critical} with $\xi = 0.5$.

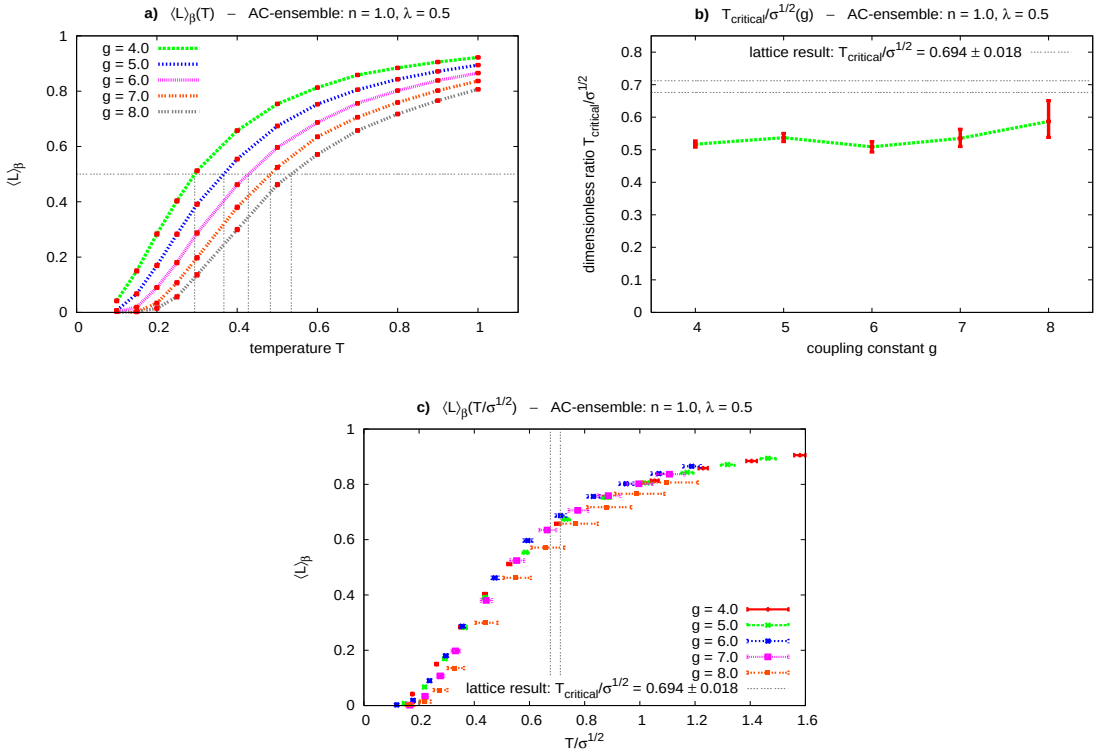

Figure 3.14: $\mathcal{AC}$-ensemble, $N \in \{113, \ldots, 1130\}$, $n = 1.0$, $\lambda = 0.5$, for different $g \in \{4.0\ ,\ 5.0\ ,\ \ldots\ ,\ 8.0\}$. **a)** $\langle L\rangle_\beta$ plotted against T. **b)** $T_{\text{critical}}/\sigma^{1/2}$ plotted against g. **c)** $\langle L\rangle_\beta$ plotted against $T/\sigma^{1/2}$.

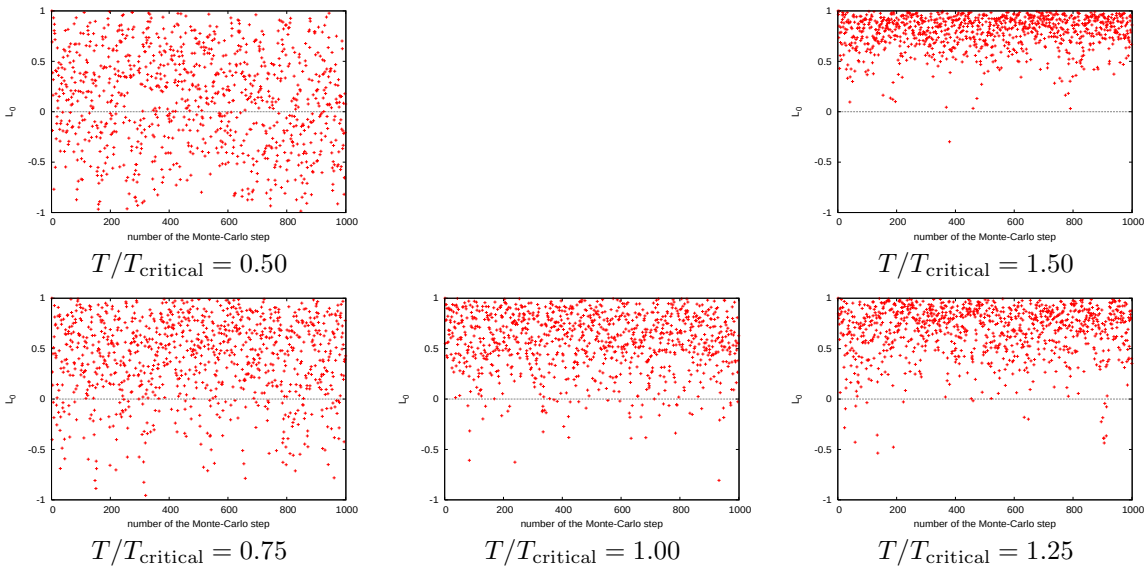

Figure 3.15: $\mathcal{AC}$-ensemble, $N \in \{516\ ,\ \ldots\ ,\ 172\}$, $n = 1.0$, $\lambda = 0.5$, $g = 6.0$. $L(\vec{0})$ plotted against the number of the Monte-Carlo step for different ratios $T/T_{\text{critical}} \in \{0.50\ ,\ 0.75\ ,\ \ldots\ ,\ 1.50\}$.

Figure 3.14b shows that the dimensionless ratio $T_{\text{critical}}/\sigma^{1/2}$ is nearly independent of the coupling constant g (σ has been obtained by area perimeter fits; c.f. Figure 3.1b). The implication is that the string tension and the critical temperature scale consistently with respect to g. We would like to stress again that such a scaling behavior, although mandatory for any sensible numerical method, is far from obvious. The value of $T_{\text{critical}}/\sigma^{1/2}$, $0.49 \ldots 0.65$, is in qualitative agreement with the lattice result $T_{\text{critical}}/\sigma^{1/2} = 0.694 \pm 0.018$ [27].

As we have explained in section 3.3.1.3, there are two methods to adjust the physical value of the temperature: varying β or varying g. Figure 3.14c shows $\langle L \rangle_\beta$ as a function of $T/\sigma^{1/2}$ for different coupling constants g. The fact that all sample points scale to a single curve demonstrates that both methods yield consistent results.

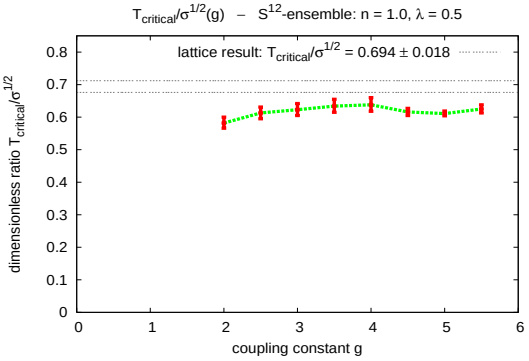

Figure 3.16: $\mathcal{S}^{12}$-ensemble, $n = 1.0$, $\lambda = 0.5$, for different $g \in \{2.0\ ,\ 2.5\ ,\ \ldots\ ,\ 5.5\}$. $T_{\text{critical}}/\sigma^{1/2}$ plotted against g.

Figure 3.15 shows the evolution of $L_{\vec{0}}$ during a single Monte-Carlo simulation (1,000 Monte-Carlo steps) for $g = 6.0$ and different $T/T_{\text{critical}} = \{0.50\ ,\ 0.75\ ,\ldots\ ,\ 1.50\}$ ($T_{\text{critical}} = 0.43$; c.f. Figure 3.14a). These plots demonstrate that in the confinement phase ($T < T_{\text{critical}}$) $L_{\mathbf{z}}$ assumes approximately an equal number of positive and negative values, whereas in the deconfinement phase ($T > T_{\text{critical}}$) the values of $L_{\mathbf{z}}$ are mainly positive.

Results: $\mathcal{S}^{12}$-ensemble, $n = 1.0$, $\lambda = 0.5$

Figure 3.16 shows the dimensionless ratio $T_{\text{critical}}/\sigma^{1/2}$ as a function of the coupling constant g (σ has been obtained by generalized Creutz ratios; c.f. Figure 3.6a). As before, it is nearly independent of g. Its value, $T_{\text{critical}}/\sigma^{1/2} = 0.57 \ldots 0.66$, is in qualitative agreement with the lattice result $T_{\text{critical}}/\sigma^{1/2} = 0.694 \pm 0.018$ [27].

Chapter 4

Applications

4.1 Pseudoparticle excitations and gauge field distributions

In this section we study instanton, antiinstanton and akyron excitations as well as the distribution of the transverse part and the longitudinal part of the gauge field. The intention is to get a better idea of how typical gauge field configurations look like in the pseudoparticle approach.

4.1.1 The distribution of instanton, antiinstanton and akyron amplitudes

We consider histograms of instanton, antiinstanton and akyron amplitudes. Histograms obtained from sufficiently many gauge field configurations approximate after a proper normalization the probability density of the pseudoparticle amplitudes.

Figure 4.1 shows the probability density of instanton amplitudes and of akyron amplitudes $\mathcal{A}(i)$ in an $\mathcal{AC}$-ensemble with $N = 400$, $n = 1.0$, $\lambda = 0.5$ and $g = 4.0$ (c.f. (2.6)). We read off from the figure that the Monte-Carlo algorithm allows for significantly larger akyron than instanton amplitudes. Note that the distribution of antiinstanton amplitudes is identical to that

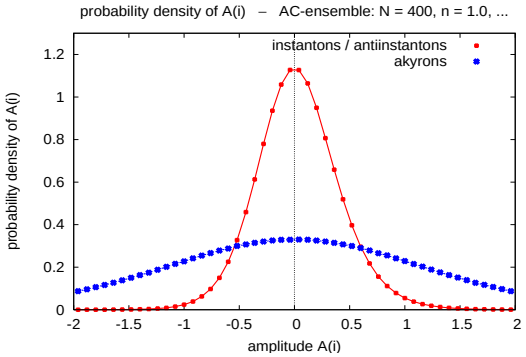

Figure 4.1: $\mathcal{AC}$-ensemble, $N = 400$, $n = 1.0$, $\lambda = 0.5$, $g = 4.0$. Probability density of $\mathcal{A}(i)$ for instantons/antiinstantons and for akyrons.

of instantons.

In Figure 4.2a the same has been done for an $\mathcal{S}^{12}$-ensemble with $N = 30 \times 12$, $n = 1.0$, $\lambda = 0.5$ and $g = 4.0$. Note that $\mathcal{S}^{ab}(i)$ corresponds to instanton/antiinstanton excitations, whereas $\mathcal{S}^{a0}(i)$ corresponds to akyron excitations (c.f. (2.9)). As in the $\mathcal{AC}$-ensemble, akyron excitations are stronger on the average than instanton/antiinstanton excitations.

In Figure 4.2b we turned off instantons/antiinstantons ("akyron ensemble") and in Figure 4.2c we turned off akyrons ("instanton ensemble"). This amounts to setting $\mathcal{S}^{ab}(i) = 0$ and $\mathcal{S}^{a0}(i) = 0$. Akyron excitations in the akyron ensemble are significantly stronger than in the "standard $\mathcal{S}^{12}$-ensemble". The implication is that instantons and antiinstantons suppress akyron excitations. On the other hand, instanton/antiinstanton excitations in the instanton ensemble and instanton/antiinstanton excitations in the "standard $\mathcal{S}^{12}$-ensemble" are nearly identical, i.e. instantons and antiinstantons are essentially unaffected by akyrons.

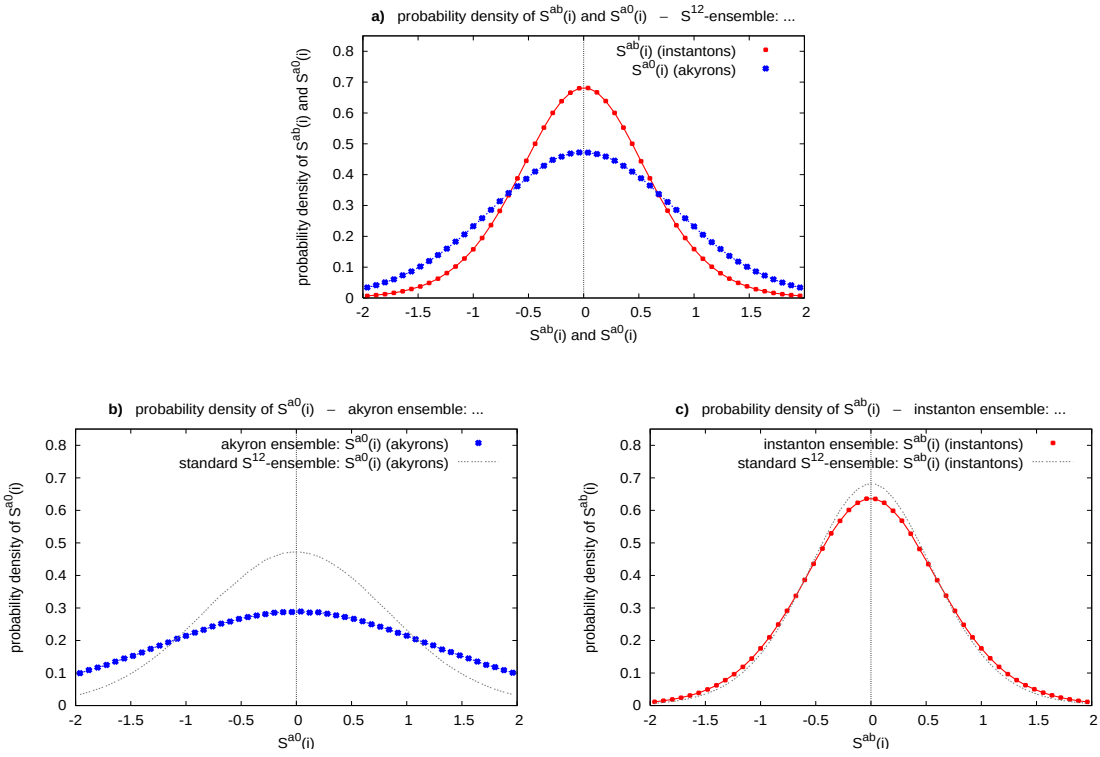

Figure 4.2: $\lambda = 0.5$, $g = 4.0$. **a)** $\mathcal{S}^{12}$-ensemble, $N = 30 \times 12$, $n = 1.0$. Probability density of $\mathcal{S}^{ab}(i)$ and $\mathcal{S}^{a0}(i)$. **b)** Akyron ensemble, $N = 30 \times 3$, $n = 1.0/4.0$. Probability density of $\mathcal{S}^{a0}(i)$. **c)** Instanton ensemble, $N = 30 \times 9$, $n = 3.0/4.0$. Probability density of $\mathcal{S}^{ab}(i)$.

4.1.2 The distribution of the transverse part and the longitudinal part of the gauge field

A gauge field configuration can be decomposed in a transverse and a longitudinal part. Superpositions of instantons and antiinstantons form transverse gauge fields, whereas akyrons form

longitudinal gauge fields (c.f. Appendix E.1). In an $\mathcal{AC}$-ensemble these parts are given by

$$A^a_{\mu,\text{transverse}}(x) = \\ = \sum_i \mathcal{A}(i)\mathcal{C}^{ab}(i)a^b_{\mu,\text{instanton}}(x - z(i)) + \sum_j \mathcal{A}(j)\mathcal{C}^{ab}(j)a^b_{\mu,\text{antiinstanton}}(x - z(j)) \tag{4.1}$$

$$A^a_{\mu,\text{longitudinal}}(x) = \sum_k \mathcal{A}(k)\mathcal{C}^{ab}(k)a^b_{\mu,\text{akyron}}(x - z(k)), \tag{4.2}$$

whereas in an $\mathcal{S}^{12}$-ensemble they are of the form

$$A^a_{\mu,\text{transverse}}(x) = \sum_i \mathcal{S}^{ab}(i)a^b_{\mu,\text{instanton}}(x - z(i)) \tag{4.3}$$

$$A^a_{\mu,\text{longitudinal}}(x) = \sum_i \mathcal{S}^{a0}(i)a^1_{\mu,\text{akyron}}(x - z(i)). \tag{4.4}$$

Figure 4.3a shows the probability density of a single component of $A^a_{\mu,\text{transverse}}$ and $A^a_{\mu,\text{longitudinal}}$ in an $\mathcal{AC}$-ensemble with $N = 400$, $n = 1.0$, $\lambda = 0.5$ and $g = 4.0$. The same has been done for an $\mathcal{S}^{12}$-ensemble with $N = 30 \times 12$, $n = 1.0$, $\lambda = 0.5$ and $g = 4.0$ in Figure 4.3b. In both cases the probability density of the transverse part is nearly identical to the probability density of the longitudinal part. However, there are three times as many transverse gauge field components than there are longitudinal gauge field components. Therefore, the longitudinal part of the gauge field exhibits proportionally stronger excitations than the transverse part. This is in accordance with our results from section 4.1.1, where we found that akyron amplitudes are larger on the average than instanton and antiinstanton amplitudes.

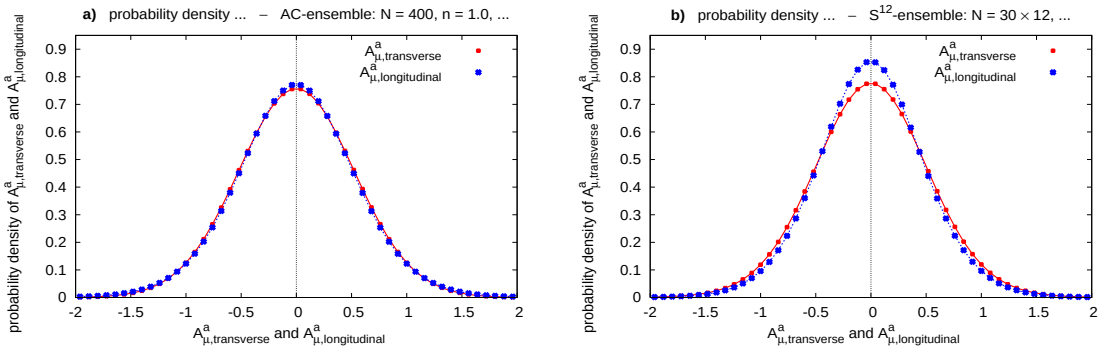

Figure 4.3: $n = 1.0$, $\lambda = 0.5$, $g = 4.0$. **a)** $\mathcal{AC}$-ensemble, $N = 400$. Probability density of $A^a_{\mu,\text{transverse}}$ and of $A^a_{\mu,\text{longitudinal}}$. **b)** $\mathcal{S}^{12}$-ensemble, $N = 30 \times 12$. Probability density of $A^a_{\mu,\text{transverse}}$ and of $A^a_{\mu,\text{longitudinal}}$.

4.2 Pseudoparticles of different size

In this section we explore how pseudoparticle results are affected by a variation of the pseudoparticle size λ, while the pseudoparticle density n or equivalently the average pseudoparticle distance

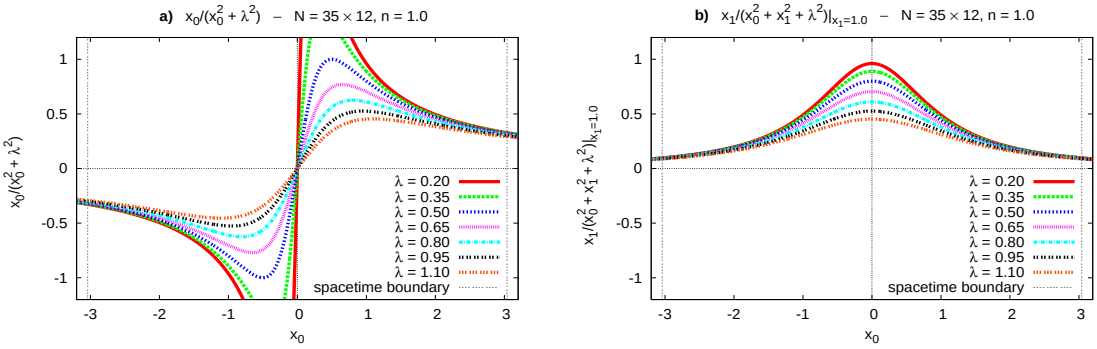

Figure 4.4: typical pseudoparticle profiles for $\lambda \in \{0.20\ ,\ 0.35\ ,\ \ldots\ ,\ 1.10\}$. **a)** $x_0/(x_0^2+\lambda^2)$ plotted against x_0. **b)** $x_1/(x_0^2+x_1^2+\lambda^2)|_{x_1=1.0}$ plotted against x_0.

$\bar{d} = 1/n^{1/4}$ is kept constant. In other words, we consider different ratios of the two ultraviolet regulators λ and $\bar{d}$ (c.f. section 2.3). In detail, we consider $\mathcal{S}^{12}$-ensembles with $N = 35 \times 12$, $n = 1.0$, $g = 4.0$ and $\lambda \in \{0.20\ ,\ 0.35\ ,\ \ldots\ ,\ 1.10\}$.

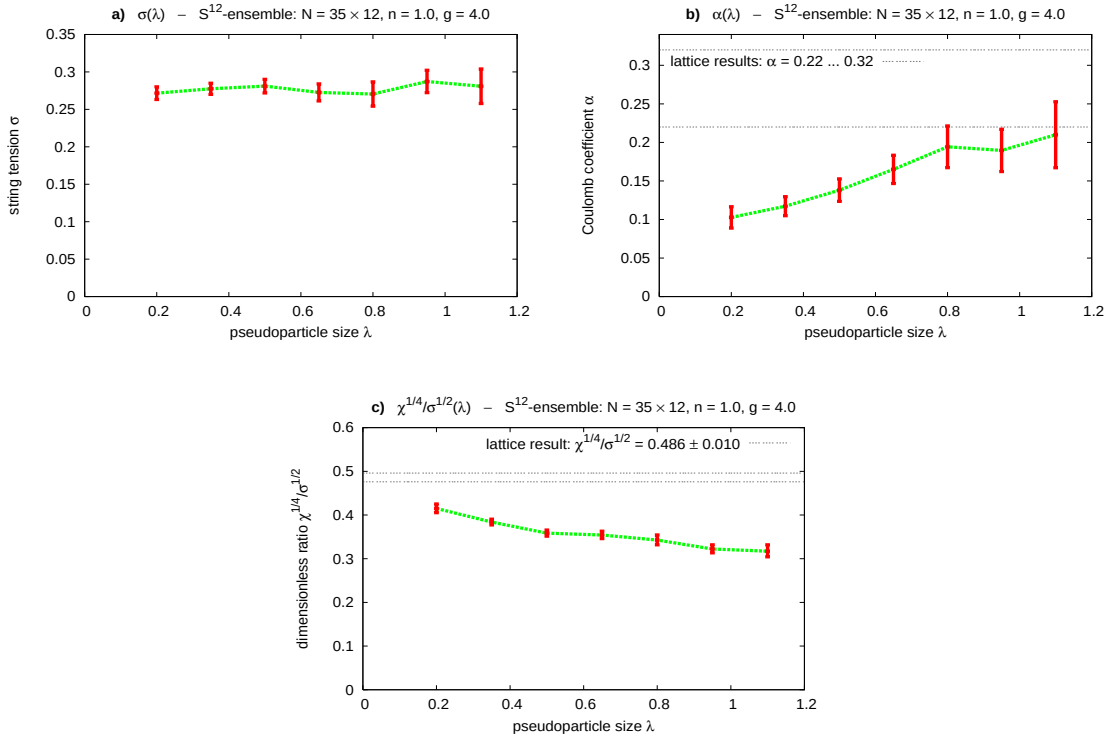

Figure 4.5: $\mathcal{S}^{12}$-ensemble, $N = 35 \times 12$, $n = 1.0$, $g = 4.0$, for different pseudoparticle sizes $\lambda \in \{0.20\ ,\ 0.35\ ,\ \ldots\ ,\ 1.10\}$. **a)** σ plotted against λ. **b)** α plotted against λ. **c)** $\chi^{1/4}/\sigma^{1/2}$ plotted against λ.

To get a better idea of the λ-dependent shape of a pseudoparticle, we plotted typical pseudoparticle profiles in Figure 4.4. Figure 4.4a shows $x_0/(x_0^2+\lambda^2)$ as a function of x_0 for different λ. The same has been done for $x_1/(x_0^2+x_1^2+\lambda^2)|_{x_1=1.0}$ in Figure 4.4b. The boundary of the spacetime hypersphere is indicated by the dotted gray lines, assuming profiles right through the center ($N = 35 \times 12$ and $n = 1.0$ amounts to $V_{\text{spacetime}} = 420.0$ and this in turn to $r_{\text{spacetime}} = 3.04$). λ strongly affects the shape of a pseudoparticle near its center. In contrast to that, the pseudoparticle size has essentially no effect on the long range behavior of a pseudoparticle, which is proportional to $1/x_0$ and $1/x_0^2$ in Figure 4.4a and 4.4b.

We obtained the string tension σ and the Coulomb coefficient α from generalized Creutz ratios (12×12-Wilson loop grids, $r_{\text{boundary}} = 2.0$, $R_1, \ldots, T_4 \in \{7a\ ,\ 8a\ ,\ \ldots\ ,\ 12a\}$, $a = 0.24$; c.f. section 3.1.1.3). They are shown as functions of the pseudoparticle size λ in Figure 4.5a and 4.5b. The Coulomb coefficient is λ-dependent but the range of values, $\alpha = 0.09 \ldots 0.25$, is of the right order of magnitude when compared to lattice results, $\alpha_{\text{lattice}} = 0.22 \ldots 0.32$ [16, 17]. The string tension σ, however, shows no λ-dependence at all. The implication is the following: confinement is connected to the $1/|x|$ long range behavior of the pseudoparticles, which is the same for all values of λ. The shape of the pseudoparticles near their center, which is λ-dependent, has no effect on the string tension and, therefore, is of no relevance to confinement.

The topological susceptibility is roughly three times larger for small pseudoparticle sizes than for large pseudoparticle sizes: $\chi = 0.0022 \ldots 0.0008$ between $\lambda = 0.20 \ldots 1.10$. However, $\chi^{1/4}$ is pretty stable with respect to λ, as is the dimensionless ratio $\chi^{1/4}/\sigma^{1/2}$ (c.f. Figure 4.5c). The range of values of the latter, $\chi^{1/4}/\sigma^{1/2} = 0.41 \ldots 0.33$ between $\lambda = 0.20 \ldots 1.10$, is in qualitative agreement with the lattice result $\chi^{1/4}_{\text{lattice}}/\sigma^{1/2}_{\text{lattice}} = 0.486 \pm 0.010$ [27].

4.3 Gaussian localized pseudoparticles of different size

To learn more about the interrelation between the long range behavior of the pseudoparticles and confinement, we study Gaussian localized pseudoparticles of different size. The corresponding ensembles are $\mathcal{S}^{12}$-ensembles, where $1/(x^2+\lambda^2)$ appearing in the definitions of instantons, anti-

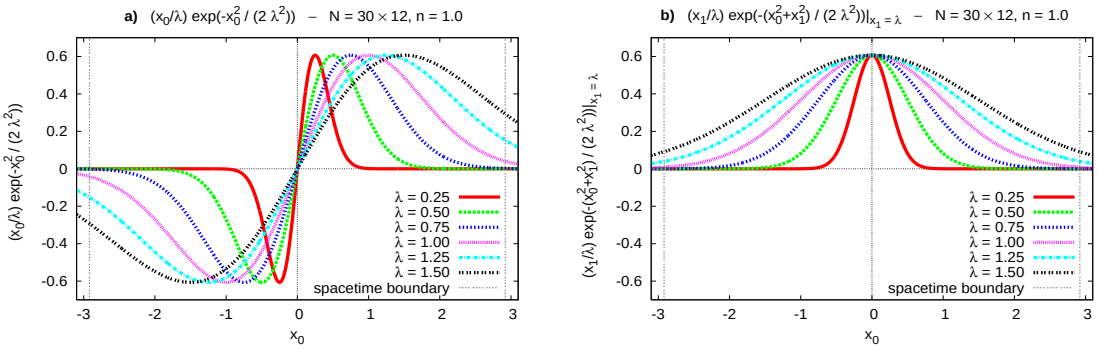

Figure 4.6: typical profiles of Gaussian localized pseudoparticles for $\lambda \in \{0.25\ ,\ 0.50\ ,\ \ldots\ ,\ 1.50\}$. **a)** $(x_0/\lambda)\exp(-x_0^2/(2\lambda^2))$ plotted against x_0. **b)** $(x_1/\lambda)\exp(-(x_0^2+x_1^2)/(2\lambda^2))|_{x_1=\lambda}$ plotted against x_0.

instantons and akyrons ((2.1) to (2.3)) is replaced by $e^{-x^2/(2\lambda^2)}$. We refer to them as $\mathcal{S}^{12,\mathrm{Gauss}}$-ensembles. The main difference between $\mathcal{S}^{12}$-ensembles and $\mathcal{S}^{12,\mathrm{Gauss}}$-ensembles is the long range behavior of their building blocks: in contrast to our standard choice of pseudoparticles, (2.1) to (2.3), Gaussian localized pseudoparticles have a strictly limited range of interaction, which is proportional to their size λ.

We consider $\mathcal{S}^{12,\mathrm{Gauss}}$-ensembles with $N = 30 \times 12$, $n = 1.0$, $g = 4.0$ and $\lambda \in \{0.25\ ,\ 0.50\ ,\ \ldots\ ,\ 1.50\}$. Typical profiles of Gaussian localized pseudoparticles, $(x_0/\lambda)\exp(-x_0^2/(2\lambda^2))$ and $(x_1/\lambda)\exp(-(x_0^2+x_1^2)/(2\lambda^2))|_{x_1=\lambda}$, are shown in Figure 4.6 for different λ. The boundary of the spacetime hypersphere is indicated by the dotted gray lines, assuming profiles right through the center ($N = 30 \times 12$ and $n = 1.0$ amounts to $V_{\mathrm{spacetime}} = 360.0$ and this in turn to $r_{\mathrm{spacetime}} = 2.92$).

Figure 4.7a shows $-\ln\langle W_{(R,T)}\rangle|_{R/T=1/2}$ for different λ (for the sake of clarity the curves have been shifted by suitably chosen constants). Ensembles with $\lambda \gtrsim 1.0$ clearly exhibit an area law, whereas for $\lambda \lesssim 0.5$ they do not indicate confinement.

We obtained numerical values for the string tension σ from area perimeter fits to the data of Figure 4.7a ($d_{\mathrm{cutoff}} = \lambda$, $r_{\mathrm{boundary}} = 2.0$; c.f. section 3.1.1.1) and from generalized Creutz ratios (12×12-Wilson loop grids, $r_{\mathrm{boundary}} = 2.0$, $R_1, \ldots, T_4 \in \{7a\ ,\ 8a\ ,\ \ldots\ ,\ 12a\}$, $a = 0.24$;

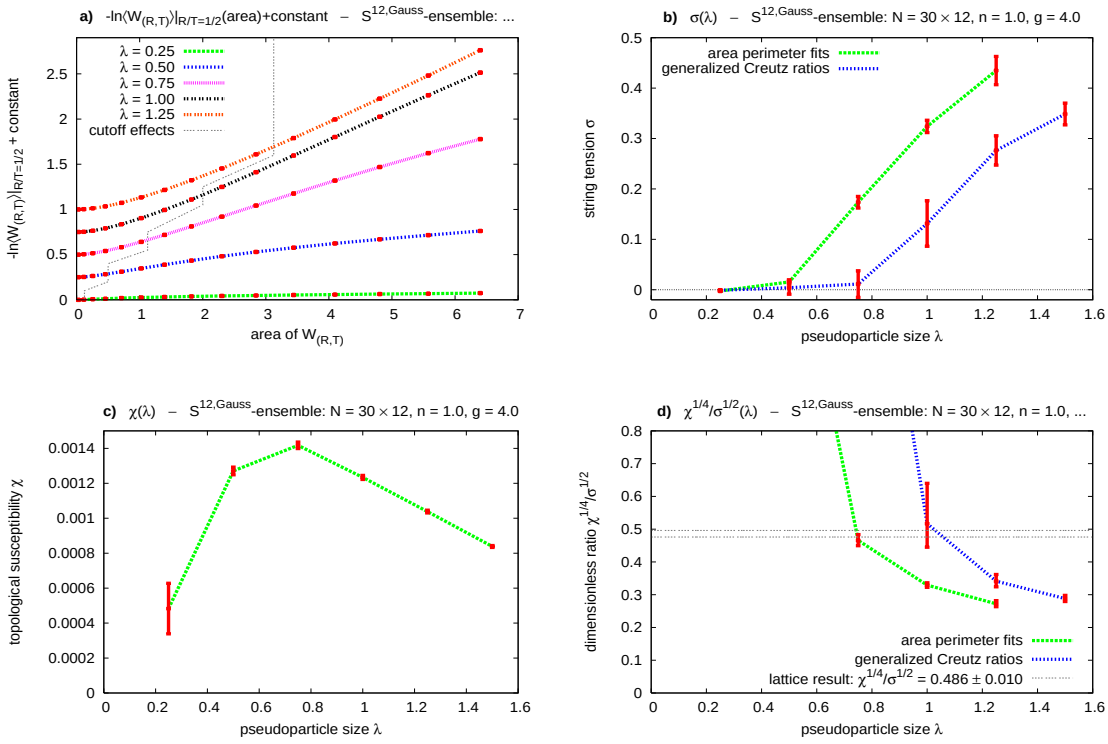

Figure 4.7: $\mathcal{S}^{12,\mathrm{Gauss}}$-ensemble, $N = 30 \times 12$, $n = 1.0$, $g = 4.0$, for different pseudoparticle sizes $\lambda \in \{0.25\ ,\ 0.50\ ,\ \ldots\ ,\ 1.50\}$. **a)** $-\ln\langle W_{(R,T)}\rangle|_{R/T=1/2}$+constant plotted against the area. **b)** σ, obtained by area perimeter fits, and σ, obtained by generalized Creutz ratios, plotted against λ. **c)** χ plotted against λ. **d)** $\chi^{1/4}/\sigma^{1/2}$ plotted against λ.

c.f. section 3.1.1.3). The results are plotted in Figure 4.7b against the pseudoparticle size λ. Both methods agree that there is no confinement for $\lambda \lesssim 0.5$ and confinement for $\lambda \gtrsim 1.0$. The onset of confinement takes place somewhere around $\lambda \approx 0.75$. This is precisely the width at which neighboring pseudoparticles start to overlap significantly (this can be seen by assigning each pseudoparticle an appropriate volume, e.g. the volume of a hypersphere of radius λ, $(\pi^2/2)\lambda^4 \approx 4.93 \times \lambda^4$, and comparing that volume with the maximum volume non-overlapping pseudoparticles can cover, i.e. $1/n = 1.0$). The implication is the following: pseudoparticle ensembles only exhibit confinement if their building blocks cover sufficiently large spacetime regions. For a positive value of the string tension significant overlaps between neighboring pseudoparticles are required. This is reminiscent of "percolation" of pseudoparticles. Note that percolation phenomena have been related to confinement in a variety of ways, e.g. percolation of center vortices [33] or percolation of monopole loops [34] in lattice gauge theory or random percolation of bonds or sites on a three dimensional lattice [35].

Figure 4.7c shows the λ-dependence of the topological susceptibility χ, which is weaker as the λ-dependence of the string tension σ. Therefore, the dimensionless ratio $\chi^{1/4}/\sigma^{1/2}$ (Figure 4.7d) is dominated by σ. The range of values for $\lambda \geq 1.0$, $\chi^{1/4}/\sigma^{1/2} = 0.27 \ldots 0.64$, is of the right order of magnitude when compared to the lattice result $\chi^{1/4}_{\text{lattice}}/\sigma^{1/2}_{\text{lattice}} = 0.486 \pm 0.010$ [27].

We also calculated the quark antiquark potential for different λ ($V_{\mathrm{q\bar{q}}}(R)$ via fitting straight lines to data points $-\ln\langle W_{(R,T)}\rangle|_{R=\text{constant}}$ at $R \in \{9a\ ,\ 10a\ ,\ 11a\ ,\ 12a\}$, $a = 0.24$; c.f. section 3.1.2). The results are shown as functions of the quark antiquark separation in Figure 4.8. For $\lambda \geq 1.25$ the potential is clearly confining, whereas for $\lambda \leq 0.50$ it is unambiguously not confining. These results are in agreement with previous results from this section.

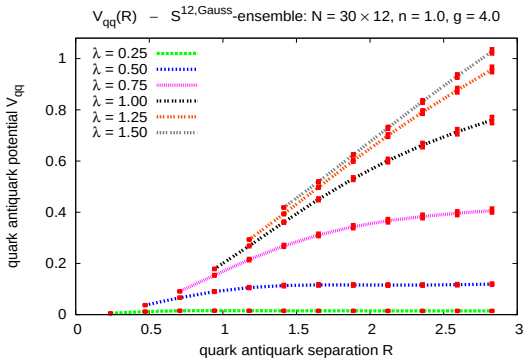

Figure 4.8: $\mathcal{S}^{12,\text{Gauss}}$-ensemble, $N = 30 \times 12$, $n = 1.0$, $g = 4.0$, for different pseudoparticle sizes $\lambda \in \{0.25\ ,\ 0.50\ ,\ \ldots\ ,\ 1.50\}$. $V_{\mathrm{q\bar{q}}}$ plotted against the separation of the quarks.

4.4 The effect of instantons, antiinstantons and akyrons

In this section we study the effect of instantons, antiinstantons and akyrons. We demonstrate that confinement arises due to instantons and antiinstantons, whereas akyrons do not produce confinement. We consider $\mathcal{AC}$-ensembles with the same number of pseudoparticles but with different ratios $N_{\text{instanton}} : N_{\text{antiinstanton}} : N_{\text{akyron}}$. In detail, we compare the following ensembles

with $N = 400$, $n = 1.0$, $\lambda = 0.5$ and $g = 4.0$:

- "Akyron ensemble": $\mathcal{AC}$-ensemble without instantons and antiinstantons, i.e. a pure akyron ensemble containing 400 akyrons.
- "Standard ensemble": $\mathcal{AC}$-ensemble containing 150 instantons, 150 antiinstantons and 100 akyrons ($N_{\text{instanton}} : N_{\text{antiinstanton}} : N_{\text{akyron}} = 3 : 3 : 2$).
- "Instanton ensemble": $\mathcal{AC}$-ensemble without akyrons, i.e. a pure instanton-like ensemble containing 200 instantons and 200 antiinstantons ($N_{\text{instanton}} : N_{\text{antiinstanton}} = 1 : 1$).

Figure 4.9a shows $-\ln\langle W_{(R,T)}\rangle|_{R/T=1/2}$ as a function of the area for all three ensembles. The standard ensemble and the instanton ensemble exhibit an area law, which is a clear sign of confinement. The akyron curve on the other hand has a significantly smaller slope and additionally exhibits a negative curvature, which might indicate a perimeter law.

We applied generalized Creutz ratios to determine the string tension for all three ensembles (12×12-Wilson loop grids, $r_{\text{boundary}} = 1.8$, $R_1, \ldots, T_4 \in \{7a\ ,\ 8a\ ,\ \ldots\ ,\ 12a\}$, $a = 0.21$; c.f. section 3.1.1.3). The results are $\sigma_{\text{akyron}} = 0.019 \pm 0.08$, $\sigma_{\text{standard}} = 0.236 \pm 0.013$ and $\sigma_{\text{instanton}} = 0.512 \pm 0.023$. The ratio of these values is given by $\sigma_{\text{akyron}} : \sigma_{\text{standard}} : \sigma_{\text{instanton}} \approx 1 : 12 : 27$.

The quark antiquark potential as a function of the separation is shown in Figure 4.9b ($V_{\text{q}\bar{\text{q}}}(R)$ via fitting straight lines to data points $-\ln\langle W_{(R,T)}\rangle|_{R=\text{constant}}$ at $R \in \{9a\ ,\ 10a\ ,\ 11a\ ,\ 12a\}$, $a = 0.21$; c.f. section 3.1.2). The qualitative picture is the same.

To compare dimensionless ratios, we calculated the topological susceptibility χ and the critical temperature T_{critical} in the standard ensemble and in the instanton ensemble:

- $(\chi^{1/4}/\sigma^{1/2})_{\text{standard}} = 0.35$.
  $(\chi^{1/4}/\sigma^{1/2})_{\text{instanton}} = 0.26$.
  $\rightarrow \quad (\chi^{1/4}/\sigma^{1/2})_{\text{standard}} : (\chi^{1/4}/\sigma^{1/2})_{\text{instanton}} = 1.33$.

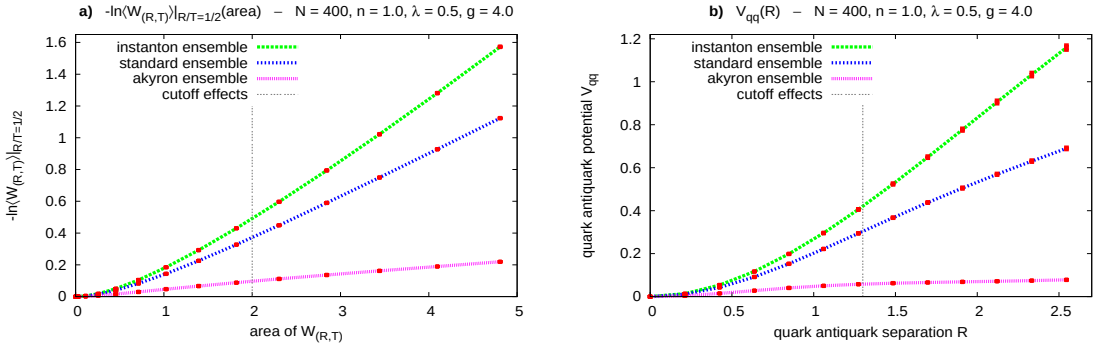

Figure 4.9: akyron ensemble (400 akyrons), standard ensemble (150 instantons, 150 antiinstantons and 100 akyrons) and instanton ensemble (200 instantons and 200 antiinstantons), $N = 400$, $n = 1.0$, $\lambda = 0.5$, $g = 4.0$. **a)** $-\ln\langle W_{(R,T)}\rangle|_{R/T=1/2}$ plotted against the area. **b)** $V_{\text{q}\bar{\text{q}}}$ plotted against the separation of the quarks.

- $(T_{\text{critical}}/\sigma^{1/2})_{\text{standard}} = 0.61.$
  $(T_{\text{critical}}/\sigma^{1/2})_{\text{instanton}} = 0.59.$
  $\rightarrow \quad (T_{\text{critical}}/\sigma^{1/2})_{\text{standard}} : (T_{\text{critical}}/\sigma^{1/2})_{\text{instanton}} = 1.02.$

When the scale is set by the string tension, akyrons have the effect of increasing the topological susceptibility, i.e. the value of $\chi^{1/4}/\sigma^{1/2}$ in the standard ensemble is larger by a factor of 1.33 than the value in the instanton ensemble. The critical temperature is essentially unaffected by akyrons. Since $(\chi^{1/4}/\sigma^{1/2})_{\text{standard}} = 0.35$ is closer to the lattice result $\chi^{1/4}_{\text{lattice}}/\sigma^{1/2}_{\text{lattice}} = 0.486 \pm 0.010$ [27] than $(\chi^{1/4}/\sigma^{1/2})_{\text{instanton}} = 0.26$, it is beneficial with respect to quantitative results to consider ensembles containing instantons and antiinstantons as well as akyrons instead of pure instanton/antiinstanton ensembles.

For the akyron ensemble the dimensionless ratios $\chi^{1/4}/\sigma^{1/2}$ and $T_{\text{critical}}/\sigma^{1/2}$ are not meaningful: the topological susceptibility χ vanishes identically (c.f. Appendix D) and the critical temperature T_{critical} is extremely small, somewhere within a range, which is barely accessible with the numerical techniques presented throughout this work. The latter might be an indication that in the akyron ensemble there is no confinement deconfinement phase transition at all. From that and the above results for the string tension, i.e. the fact that σ is more than ten times smaller in the akyron ensemble than in the other two ensembles, we conclude that gauge field configurations made up solely of akyrons are not suited to produce confinement. On the other hand, gauge field configurations, which are responsible for confinement, necessarily contain instantons and antiinstantons.

It is interesting to note that any linear superposition of akyrons and, therefore, any field configuration in a pure akyron ensemble has zero topological charge density (c.f. Appendix D). This supports the common expectation that confinement and topological charge are closely related.

We performed similar calculations in $\mathcal{S}^{12}$-ensembles with 30 pseudoparticle clusters. The akyron ensemble has been realized by turning off instantons, i.e. by setting $\mathcal{S}^{ab} = 0$, and likewise the instanton ensemble has been realized by turning off akyrons, i.e. by setting $\mathcal{S}^{a0} = 0$. We obtained qualitatively the same results as in the $\mathcal{AC}$-ensembles.

4.5 Very large pseudoparticle ensembles

In section 2.4 we have shown that pseudoparticle results are pretty stable for pseudoparticle numbers N in the range $100 \ldots 800$. In the following we demonstrate that the pseudoparticle approach is not anymore a successful effective model when $N \gtrsim 5,000$.

We applied generalized Creutz ratios to determine the string tension in an $\mathcal{S}^{12}$-ensemble with $N = 35 \times 12$ and in another identical $\mathcal{S}^{12}$-ensemble with $N = 400 \times 12$ ($n = 1.0$, $\lambda = 0.5$, $g = 2.0$). The results are $\sigma_{N=35\times12} = 0.084 \pm 0.004$ (12×12-Wilson loop grids, $r_{\text{boundary}} = 2.0$, $R_1, \ldots, T_4 \in \{7a\ ,\ 8a\ ,\ \ldots\ ,\ 12a\}$, $a = 0.24$; c.f. section 3.1.1.3) and $\sigma_{N=400\times12} = 0.010 \pm 0.009$ (12×12-Wilson loop grids, $r_{\text{boundary}} = 3.24$, $R_1, \ldots, T_4 \in \{7a\ ,\ 8a\ ,\ \ldots\ ,\ 12a\}$, $a = 0.38$; c.f. section 3.1.1.3). Figure 4.10a shows that the ensemble with $N = 35 \times 12$ clearly exhibits confinement, while Figure 4.10b indicates that there is no confinement when using $N = 400 \times 12$ pseudoparticles.

We performed similar calculations for a wide range of coupling constants $g \in \{1.0\ ,\ 1.5\ ,\ \ldots\ 4.0\}$

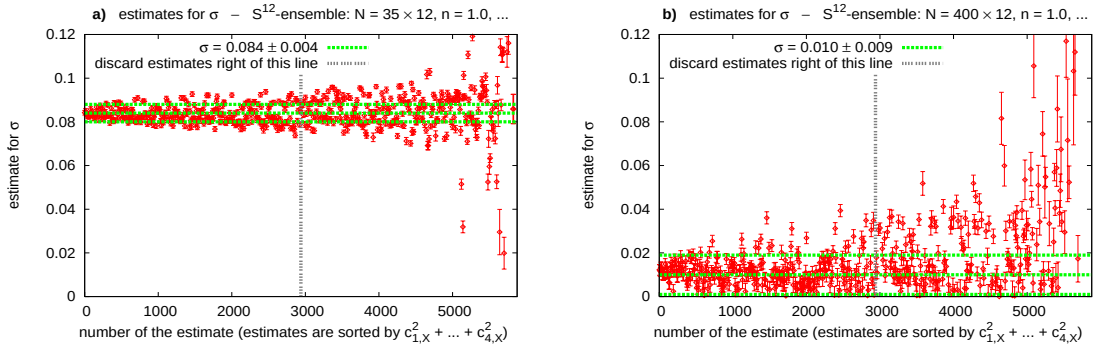

Figure 4.10: $\mathcal{S}^{12}$-ensemble, $n = 1.0$, $\lambda = 0.5$, $g = 2.0$. **a)** Estimates for σ sorted according to $c^2_{1,X} + \ldots + c^2_{4,X}$ for $N = 35 \times 12$. **b)** Estimates for σ sorted according to $c^2_{1,X} + \ldots + c^2_{4,X}$ for $N = 400 \times 12$.

and for different pseudoparticle sizes $\lambda \in \{0.5\,,\, 1.5\}$. For all these calculations the qualitative picture is the same. It seems that the loss of confinement is solely a consequence of the large pseudoparticle number.

On the other hand, this result is hardly surprising. One can show that in the continuum limit, i.e. in the limit of infinitely many pseudoparticles, the gauge field and the integration measure in an $\mathcal{A}$-ensemble as well as in an $\mathcal{S}^{12}$-ensemble are almost identical to those in continuum SU(2) Yang-Mills theory (c.f. Appendix F). In other words, $\mathcal{A}$-ensembles and $\mathcal{S}^{12}$-ensembles have the correct naive continuum limit with respect to SU(2) Yang-Mills theory. Therefore, we expect the pseudoparticle approach to behave similar to non-compact lattice gauge theory when the number of pseudoparticles is sufficiently large, i.e. the number of degrees of freedom is of the same order of magnitude as on small lattices. Since non-compact lattice gauge theory has shown no sign of quark confinement (c.f. e.g. [36]), we do not expect it for the pseudoparticle approach either when a large number of pseudoparticles is used.

According to the common expectation the reason why non-compact lattice gauge theory fails to produce confinement is the lack of exact gauge invariance, which we do not have in the pseudoparticle approach either. It has been shown that establishing a certain kind of exact gauge invariance in non-compact lattice calculations restores confinement [37]. Whether something similar can be done in the pseudoparticle approach, is an interesting but presently open question. An obvious step in this direction would be to impose a gauge fixing, e.g. Lorentz gauge $\partial_\mu A_\mu = 0$, which can be realized by simply turning off akyrons. However, such a gauge fixing comes along with the difficult and time consuming task of computing Faddeev Popov determinants. Furthermore, it is not clear whether such a procedure is sufficient to restore confinement and to turn the pseudoparticle approach into a general numerical technique. There might still be other problems, e.g. arising from improper handling of Gribov copies. We have not pursued this matter further yet.

To summarize, the pseudoparticle approach is a successful effective model for SU(2) Yang-Mills theory when around 400 pseudoparticles are employed. However, at this stage the pseudoparticle approach is not a general numerical technique, which can be applied with an arbitrary large number of pseudoparticles.

4.6 The pseudoparticle approach in quantum mechanics

The pseudoparticle approach is in no way restricted to SU(2) Yang-Mills theory. With minor modifications it can be applied to "any other quantum field theory". In this section we give an example. We apply the pseudoparticle approach to a well known and analytically solvable problem from quantum mechanics, the 1-dimensional harmonic oscillator.

4.6.1 Calculating energy levels in the path integral formalism

The Euclidean action of the 1-dimensional harmonic oscillator is given by

$$S[X] = \int dt \left(\frac{m}{2} \dot{X}^2 + \frac{m\omega^2}{2} X^2 \right). \tag{4.5}$$

Our goal in this section is to calculate the energy levels of the first excitation with negative parity and the first excitation with positive parity with respect to the ground state via the pseudoparticle approach. The results, $E_- - E_0 = \omega$ and $E_+ - E_0 = 2\omega$, are well known and can be obtained analytically in a couple of different ways. Here we have to resort to the path integral formalism so that the pseudoparticle approach can be applied.

To this end, we consider time ordered correlation functions:

$$C_-(t) = \Big\langle X(t)X(0) \Big\rangle = \frac{1}{Z} \int DX\, X(t)X(0) e^{-S[X]} \tag{4.6}$$

$$\begin{aligned} C_+(t) &= \Big\langle \Big(X(t)^2 - \langle X^2 \rangle \Big) \Big(X(0)^2 - \langle X^2 \rangle \Big) \Big\rangle = \\ &= \frac{1}{Z} \int DX \Big(X(t)^2 - \langle X^2 \rangle \Big) \Big(X(0)^2 - \langle X^2 \rangle \Big) e^{-S[X]} \end{aligned} \tag{4.7}$$

with

$$Z = \int DX\, e^{-S[X]} \tag{4.8}$$

($\langle \mathcal{O} \rangle$ denotes the ensemble average of $\mathcal{O}$ which is equivalent to the ground state expectation value of the time ordered product of $\mathcal{O}$). Inserting complete sets of energy eigenstates and considering parity yields

$$\lim_{t \to \infty} -\ln(C_-(t)) = \Big(E_- - E_0 \Big) t + C_{-,0} \tag{4.9}$$

$$\lim_{t \to \infty} -\ln(C_+(t)) = \Big(E_+ - E_0 \Big) t + C_{+,0} \tag{4.10}$$

($C_{-,0}$ and $C_{+,0}$ are irrelevant constants). We can read off the energy differences $E_- - E_0$ and $E_+ - E_0$ from the slopes of $-\ln(C_-(t))$ and $-\ln(C_+(t))$ for large t.

For later comparison we state the analytical results for C_- and C_+:

$$C_-(t) = \frac{1}{2m\omega} e^{-\omega |t|} \tag{4.11}$$

$$C_+(t) = \frac{1}{2m^2\omega^2} e^{-2\omega |t|}. \tag{4.12}$$

4.6.2 Application of the pseudoparticle approach

In analogy to (2.1) to (2.3) we consider pseudoparticles

$$x(t) \quad = \quad \frac{t}{t^2 + \lambda^2} \tag{4.13}$$

(c.f. Figure 4.11a). Paths X are represented by a superposition of N pseudoparticles and a constant C:

$$X(t) \quad = \quad \sum_{i=1}^{N} \mathcal{A}(i) x(t - z(i)) + C \tag{4.14}$$

(the i-th pseudoparticle has amplitude $\mathcal{A}(i)$ and position $z(i)$). The integration over all paths is approximated by

$$\int DX \ \ldots \quad \approx \quad \int \left(\prod_{i=1}^{N} d\mathcal{A}(i) \right) dC \ \ldots \tag{4.15}$$

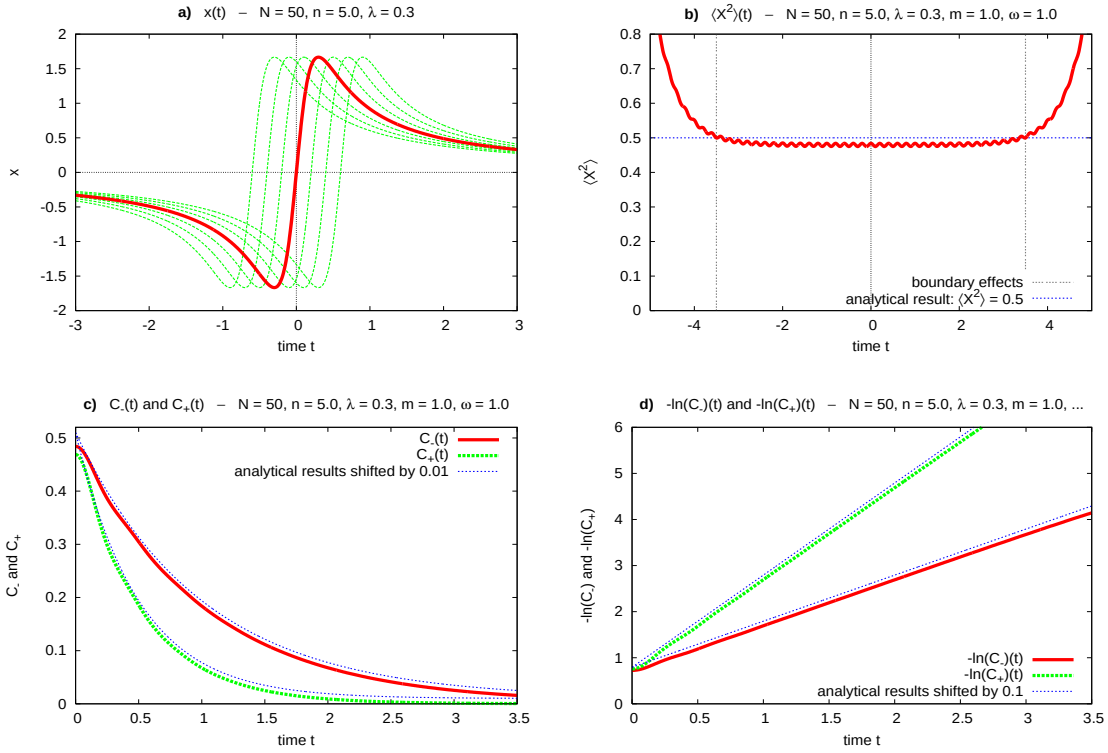

Figure 4.11: the 1-dimensional harmonic oscillator in the pseudoparticle approach, $N = 50$, $n = 5.0$, $\lambda = 0.3$, $m = 1.0$, $\omega = 1.0$. **a)** A couple of pseudoparticles plotted against t. **b)** $\langle X^2 \rangle$ plotted against t. **c)** C_- and C_+ plotted against t and the corresponding analytical results shifted by 0.01 for the sake of clarity. **d)** $-\ln(C_-)$ and $-\ln(C_+)$ plotted against t and the corresponding analytical results shifted by 0.1 for the sake of clarity.

This time there is no need for Monte-Carlo simulations, since the action is a quadratic expression in $\mathcal{A}(i)$ and C. We can compute "path integrals" by inverting the "action matrix" numerically.

Note that there is a strong analogy to $\mathcal{A}$-ensembles (c.f. section 2.2.1).

Results: $N = 50$**,** $n = 5.0$**,** $\lambda = 0.3$**,** $m = 1.0$**,** $\omega = 1.0$

We employed $N = 50$ pseudoparticles with positions $z(i)$ chosen uniformly inside a "time volume" $[-5.0, 5.0]$, i.e. $z(i) = (N - 25.5)/5.0$, $i = 1, \ldots, 50$.

Figure 4.11b shows $\langle X^2 \rangle$ as a function of t. For $-3.5 \leq t \leq 3.5$ the pseudoparticle result is very close to the analytical result $\langle X^2 \rangle_{\text{analytical}} = 1/2m\omega = 0.5$. We expect boundary effects to be negligible in this region.

In Figure 4.11c and 4.11d the pseudoparticle results for the correlation functions (4.6) and (4.7) and their negative logarithms are plotted against t. They are nearly identical to the analytical results (4.11) and (4.12). Therefore, we are able to extract very accurate numerical values for the energy differences $E_- - E_0$ and $E_+ - E_0$.

Considering the quality of these results, we conclude that the pseudoparticle approach in quantum mechanics with $N = 50$ is rather a trustworthy numerical technique than an effective model, as it is the case for SU(2) Yang-Mills theory.

Chapter 5

Summary and outlook

In this work we have presented the pseudoparticle approach, a numerical method to approximate path integrals in SU(2) Yang-Mills theory. We calculated the static quark antiquark potential, the topological susceptibility and the critical temperature of the confinement deconfinement phase transition in different pseudoparticle ensembles. When applied with around 400 instantons, antiinstantons and akyrons, the pseudoparticle approach reproduces many essential features of SU(2) Yang-Mills theory. The number of degrees of freedom is significantly smaller than it is in typical lattice calculations.

5.1 The pseudoparticle approach as a successful effective model for SU(2) Yang-Mills theory

Within error tolerance the quark antiquark potential in the pseudoparticle approach can by parameterized by $V_{\mathrm{q\bar{q}}}(R) = V_0 - \alpha/R + \sigma R$, i.e. it is linear for large separations with an attractive $1/R$-correction as predicted by the bosonic string picture [18, 19]. Additionally we have applied four different methods to determine numerical values for the string tension σ and the Coulomb coefficient α, which are all based on "guessing" the functional dependence of ensemble averages of rectangular Wilson loops $\langle W_{(R,T)} \rangle$. We obtained consistent results. The method of generalized Creutz ratios, which has been developed in the context of this work, is particularly well suited to check the consistency of the Wilson loop ansatz (3.4) and Monte Carlo data for $\langle W_{(R,T)} \rangle$, and therefore the quality of the resulting string tension and the resulting Coulomb coefficient.

The string tension is unambiguously positive, which is a clear indication of confinement. Furthermore, it is an increasing function of the coupling constant g. When the scale is set by the string tension, i.e. by identifying σ with the physical value $4.2/\mathrm{fm}^2$, one can adjust the physical size of the spacetime hypersphere by choosing appropriate values for g.

The value of the Coulomb coefficient for large coupling constants, i.e. for quark antiquark separations $\gtrsim 0.5\,\mathrm{fm}$, is of the right order of magnitude, i.e. $\alpha \approx 0.2$, when compared to the prediction from the bosonic string picture, $\alpha_{\mathrm{string}} = \pi/12 \approx 0.26$ [18, 19], and to lattice results, $\alpha_{\mathrm{lattice}} = 0.22 \ldots 0.32$ [16, 17].

We also calculated the the topological susceptibility χ and the critical temperature of the

confinement deconfinement phase transition T_{critical}. The dimensionless ratios $\chi^{1/4}/\sigma^{1/2}$ and $T_{\text{critical}}/\sigma^{1/2}$ are constant for a wide range of coupling constants, i.e. σ, χ and T_{critical} exhibit consistent scaling behaviors with respect to g. This success strongly indicates that one can extract sensible physics from the pseudoparticle approach. The values of these dimensionless ratios, $\chi^{1/4}/\sigma^{1/2} = 0.29 \ldots 0.39$ and $T_{\text{critical}}/\sigma^{1/2} = 0.49 \ldots 0.66$, are in qualitative agreement with the lattice results, $\chi^{1/4}_{\text{lattice}}/\sigma^{1/2}_{\text{lattice}} = 0.486 \pm 0.010$ and $T_{\text{critical}}/\sigma^{1/2} = 0.694 \pm 0.018$ [27].

For the near future we plan to calculate other temperature dependent quantities, e.g. the energy density and the pressure, as well as glueball masses. Furthermore, we intend to include fermions in the pseudoparticle approach.

5.2 Applications of the pseudoparticle approach

We explored the effect of the pseudoparticle size λ on the string tension and on confinement. For ensembles of instantons, antiinstantons and akyrons the string tension shows no sign of a λ-dependence at all. The conclusion is that confinement is solely a consequence of the long range behavior of the building blocks, which is in this case unaffected by the pseudoparticle size. This has been confirmed by considering ensembles of Gaussian localized pseudoparticles, for which the size parameter strongly affects the long range behavior. For small λ there is only little overlap between neighboring pseudoparticles. Confinement is completely lost. Increasing λ to a value, where pseudoparticles overlap and interact significantly, restores quark confinement. We deduce that in order to exhibit confinement, pseudoparticle ensembles require building blocks, which are able to interact over sufficiently large distances. On the other hand, gauge field configurations with only localized excitations do not produce confinement. It seems that gauge field configurations, which are responsible for confinement, contain extended structures and large area excitations.

Comparing our "standard ensembles" with pure instanton/antiinstanton ensembles and pure akyron ensembles led to the conclusion that confinement arises due to instantons and antiinstantons and not because of akyrons. Keeping in mind that gauge field configurations made up solely of akyrons have vanishing topological charge density, our findings support the common expectation that topological charge and confinement are closely related. For the quality of quantitative results akyrons seem to play an important role. The dimensionless ratio $\chi^{1/4}/\sigma^{1/2}$ is significantly closer to the lattice result when there are not only instantons and antiinstantons but also akyrons. $T_{\text{critical}}/\sigma^{1/2}$ on the other hand is unaffected by akyrons.

We have also shown that the pseudoparticle approach is limited to a small number of pseudoparticles. While numerical results are stable and in agreement with lattice results for ensembles containing between 100 and 800 pseudoparticles, the qualitative picture changes significantly when applying around $5,000$ pseudoparticles. Especially confinement seems to get lost. This indicates a connection to non-compact lattice gauge theory, where a similar behavior has been observed [36]. Whether the pseudoparticle approach can be improved so that it is a general numerical technique, which can be applied with an arbitrary large number of pseudoparticles, e.g. by imposing a gauge fixing, is an interesting but open question.

Finally we modified the pseudoparticle approach for quantum mechanics and applied it to the 1-dimensional harmonic oscillator. The resulting energy levels are in excellent agreement with analytical results.

5.3 Concluding remarks

The results presented throughout this work have shown that the pseudoparticle approach is a technique with many interesting aspects, which are worth further investigations. There are two essentially different starting points for future research. The first is to keep working with around 400 pseudoparticles and to extend the effective model for SU(2) Yang-Mills theory, as it has been considered for the major part of this work, e.g. by calculating other observables or by including fermions. This might lead to further insights into the mechanisms of the Yang-Mills path integral and the relevance of its field configurations with respect to confinement. The other starting point is to improve the pseudoparticle approach so that it can cope with very large pseudoparticle numbers, e.g. by imposing a gauge fixing. The intention would be to develop a general numerical method to compute path integrals in Yang-Mills theory without discretizing spacetime.

Appendix A

Euclidean SU(2) Yang-Mills theory

In this appendix we review some essential elements of SU(2) Yang-Mills theory.

Throughout the whole work, spacetime is considered to be Euclidean with metric $\eta_{\mu\nu} = \mathrm{diag}(1,1,1,1)$.

The SU(2) Yang-Mills action is given by

$$S = \int d^4x\, s \tag{A.1}$$

with action density

$$s = \frac{1}{4g^2} F^a_{\mu\nu} F^a_{\mu\nu} \tag{A.2}$$

(g is the dimensionless coupling constant) and field strength

$$F^a_{\mu\nu} = \partial_\mu A^a_\nu - \partial_\nu A^a_\mu + \epsilon^{abc} A^b_\mu A^c_\nu \tag{A.3}$$

($\epsilon_{123} = 1$).

The gauge field A^a_μ can also be written in matrix form:

$$A_\mu = A^a_\mu \frac{\sigma^a}{2} \tag{A.4}$$

(σ^a are the Pauli matrices).

The action (A.1) and the action density (A.2) are invariant under gauge transformations

$$A_\mu(x) \;\rightarrow\; A'_\mu(x) = U(x) A_\mu(x) U^{-1}(x) - i\Big(\partial_\mu U(x)\Big) U^{-1}(x) \quad , \quad U(x) \in \mathrm{SU}(2). \tag{A.5}$$

The topological charge is defined by

$$Q = \int d^4x\, q \tag{A.6}$$

with topological charge density

$$q = \frac{1}{32\pi^2} F^a_{\mu\nu} \tilde{F}^a_{\mu\nu} \tag{A.7}$$

and dual field strength

$$\tilde{F}^a_{\mu\nu} = \frac{1}{2} \epsilon_{\mu\nu\alpha\beta} F^a_{\alpha\beta} \tag{A.8}$$

($\epsilon_{0123} = -1$).

The classical equations of motion can be obtained from (A.1) via the principle of least action. They are given by

$$\partial_\mu F^a_{\mu\nu} + \epsilon^{abc} A^b_\mu F^c_{\mu\nu} = 0. \tag{A.9}$$

Regular gauge instantons,

$$A^a_\mu = \mathcal{C}^{ab} \frac{2\eta^b_{\mu\nu}(x_\nu - z_\nu)}{(x-z)^2 + \lambda^2} \quad , \quad \eta^b_{\mu\nu} = \epsilon_{b\mu\nu} + \delta_{b\mu}\delta_{0\nu} - \delta_{b\nu}\delta_{0\mu}, \tag{A.10}$$

($\mathcal{C}^{ab}$: color orientation matrix, c.f. Appendix C, z_μ: position, λ: size) are solutions to the classical equations of motion (A.9) with action $S = 8\pi^2/g^2$ and topological charge $Q = +1$ [38]. The same is true for antiinstantons,

$$A^a_\mu = \mathcal{C}^{ab} \frac{2\bar{\eta}^b_{\mu\nu}(x_\nu - z_\nu)}{(x-z)^2 + \lambda^2} \quad , \quad \bar{\eta}^b_{\mu\nu} = \epsilon_{b\mu\nu} - \delta_{b\mu}\delta_{0\nu} + \delta_{b\nu}\delta_{0\mu}, \tag{A.11}$$

which have topological charge $Q = -1$.

Appendix B

Data analysis and error bars

In this appendix we outline how error bars for various quantities have been calculated throughout this work.

B.1 Error bars for ensemble averages ($\langle s \rangle$, $\langle |A^a_{\parallel}| \rangle$, $\langle |A^a_{\perp}| \rangle$, $\langle W_{(R,T)} \rangle$, $\langle Q_V^2 \rangle$ and $\langle L \rangle_\beta$)

In order to calculate the ensemble average $\langle \mathcal{O} \rangle$, where $\mathcal{O}$ is either s, $|A^a_{\parallel}|$, $|A^a_{\perp}|$, $W_{(R,T)}$, Q_V^2 or L_β,we generate field configurations by performing N independent Monte-Carlo simulations. From each of these Monte-Carlo simulations we take M field configurations, for which we evaluate $\mathcal{O}$ (c.f. section 2.3.1). Taking the average of the resulting M values provides N independent estimates $\mathcal{O}_i$. Assuming a normal distribution for these estimates, the maximum likelihood estimators of the ensemble average $\langle \mathcal{O} \rangle$ and its standard deviation $\sigma(\mathcal{O})$ are given by

$$\left\langle \mathcal{O} \right\rangle = \frac{1}{N} \sum_{i=1}^{N} \mathcal{O}_i \tag{B.1}$$

$$\sigma(\mathcal{O}) = \left(\frac{1}{N(N-1)} \sum_{i=1}^{N} \left(\mathcal{O}_i - \left\langle \mathcal{O} \right\rangle \right)^2 \right)^{1/2} \tag{B.2}$$

[40]. Error bars cover the interval $[\langle \mathcal{O} \rangle - \sigma(\mathcal{O}), \langle \mathcal{O} \rangle + \sigma(\mathcal{O})]$.

Most of the results presented throughout this work have been obtained with $N = 6,000$ and $M = 20$.

B.2 Error bars for $-\ln\langle W_{(R,T)} \rangle$

Error bars for $-\ln\langle W_{(R,T)} \rangle$ cover the interval
$[-\ln(\langle W_{(R,T)} \rangle + \sigma(W_{(R,T)})), -\ln(\langle W_{(R,T)} \rangle - \sigma(W_{(R,T)}))]$.

B.3 Error bars for σ and α (fitting methods) and $V_{\mathrm{q\bar{q}}}(R)$

In order to fit the Wilson loop ansatz (3.4) to Monte-Carlo data for $-\ln\langle W_{(R,T)}\rangle$ to determine σ and/or α (c.f. section 3.1.1.1 and 3.1.1.4), we apply the method of least squares, which is a standard technique from statistics (c.f. e.g. [40]). To check the quality of the resulting fit, we perform a χ^2-Test with a significance value of 5%. If the χ^2-Test fails, we adjust the standard deviations of the fit parameters σ and α by a heuristic method presented in [41]. Error bars cover one standard deviation in both directions.

When determining the quark antiquark potential $V_{\mathrm{q\bar{q}}}(R)$ (c.f. section 3.1.2), fitting is carried out in the same way.

B.4 Error bars for $-\ln(\Gamma_X(R_1,\ldots,T_4))$, σ and α (generalized Creutz ratios)

At first we calculate ten independent estimates for each ensemble average $\langle W_{(R,T)}\rangle$ by considering ten times $N/10$ independent Monte-Carlo simulations. From these results we determine ten independent values for $-\ln(\Gamma_X(R_1,\ldots,T_4))$. Then we apply (B.1) and (B.2) with $N = 10$. Errororbars cover the interval $[\langle\mathcal{O}\rangle - \sigma(\mathcal{O}), \langle\mathcal{O}\rangle + \sigma(\mathcal{O})]$.

To extract a single value for the string tension σ or the Coulomb coefficient α, we sort the corresponding estmates according to $c_{1,X}^2 + \ldots + c_{4,X}^2$ and calculate the average and the standard deviation of the "smaller half". Error bars cover one standard deviation in both directions.

B.5 Error bars for T_{critical}

At first we calculate $\langle L\rangle_{\beta_i}$ and $\sigma(L_{\beta_i})$ for a couple of different temperatures $T_i = 1/\beta_i$.

Let T_- be the largest temperature T_i with $\langle L\rangle_{\beta_i} < \xi$ and T_+ be the next largest temperature T_j, i.e. the smallest temperature T_j with $\langle L\rangle_{\beta_j} > \xi$. The error bar for T_{critical} covers the interval $[T_{\mathrm{critical,min}}, T_{\mathrm{critical,max}}]$, where $T_{\mathrm{critical,min}}$ is that temperature, where a straight line through $(T_-, \langle L\rangle_{\beta_-} + \sigma(L_{\beta_-}))$ and $(T+, \langle L\rangle_{\beta_+} + \sigma(L_{\beta_+}))$ crosses ξ, and $T_{\mathrm{critical,max}}$ is that temperature, where a straight line through $(T_-, \langle L\rangle_{\beta_-} - \sigma(L_{\beta_-}))$ and $(T+, \langle L\rangle_{\beta_+} - \sigma(L_{\beta_+}))$ crosses ξ.

B.6 Error bars for $\chi^{1/4}/\sigma^{1/2}$ and $T_{\mathrm{critical}}/\sigma^{1/2}$

Error bars for $\chi^{1/4}/\sigma^{1/2}$ cover the interval $[(\chi-\Delta\chi)^{1/4}/(\sigma+\Delta\sigma)^{1/2}, (\chi+\Delta\chi)^{1/4}/(\sigma-\Delta\sigma)^{1/2}]$, where $\chi = \langle Q_V^2\rangle/V$, $\Delta\chi = \sigma(Q_V^2)/V$ and errororbars for σ cover the interval $[\sigma-\Delta\sigma, \sigma+\Delta\sigma]$.

Error bars for $T_{\mathrm{critical}}/\sigma^{1/2}$ cover the interval $[T_{\mathrm{critical,min}}/(\sigma+\Delta\sigma)^{1/2}, T_{\mathrm{critical,max}}/(\sigma-\Delta\sigma)^{1/2}]$.

Appendix C

Color orientation matrices

A color orientation is equivalent to a spacetime independent gauge transformation. Such a gauge transformation can be specified by an element of SU(2): $U = c_0 + ic_a\sigma^a$ with $c_0^2 + \mathbf{c}^2 = 1$. Applying this gauge transformation to a gauge field A_μ yields

$$A'_\mu \;=\; UA_\mu U^{-1} \tag{C.1}$$

(c.f. (A.5)) or expressed in components

$$\begin{aligned} A_\mu^{a\prime} \;&=\; \mathrm{Tr}(\sigma^a A'_\mu) \;=\; \mathrm{Tr}\left(\sigma^a\Big(c_0 + ic_c\sigma^c\Big)A_\mu^b\frac{\sigma^b}{2}\Big(c_0 - ic_d\sigma^d\Big)\right) \;= \\ &=\; \underbrace{\Big(\delta^{ab}\Big(c_0^2 - \mathbf{c}^2\Big) + 2c_ac_b + \epsilon^{abc}2c_0c_c\Big)}_{=\mathcal{C}^{ab}} A_\mu^b \;=\; \mathcal{C}^{ab}A_\mu^b. \end{aligned} \tag{C.2}$$

We refer to $\mathcal{C}^{ab}$ as color orientation matrix.

Color orientation matrices fulfill

$$\mathcal{C}\mathcal{C}^T \;=\; \mathcal{C}^T\mathcal{C} \;=\; 1 \tag{C.3}$$

$$\det(\mathcal{C}) \;=\; 1. \tag{C.4}$$

Therefore, they are elements of SO(3).

In the following we prove that there are color orientation matrices $\mathcal{C}^{ab}(i)$, $i = 1, \ldots, 9$, so that any matrix $\mathcal{S}^{ab}$ can be represented according to

$$\mathcal{S}^{ab} \;=\; \sum_{i=1}^{9}\mathcal{A}(i)\mathcal{C}^{ab}(i), \tag{C.5}$$

where $\mathcal{A}(i)$ are suitably chosen amplitudes. We do that by showing that color orientation matrices form a basis of all 3×3-matrices:

$$\frac{1}{2}\mathcal{C}^{ab}(c_0 = 1) + \frac{1}{2}\mathcal{C}^{ab}(c_1 = 1) \;=\; \begin{pmatrix} 1 & 0 & 0 \\ 0 & 0 & 0 \\ 0 & 0 & 0 \end{pmatrix} \tag{C.6}$$

$$\frac{1}{2}\mathcal{C}^{ab}(c_0=1)+\frac{1}{2}\mathcal{C}^{ab}(c_2=1) \;=\; \begin{pmatrix} 0 & 0 & 0 \\ 0 & 1 & 0 \\ 0 & 0 & 0 \end{pmatrix} \tag{C.7}$$

$$\frac{1}{2}\mathcal{C}^{ab}(c_0=1)+\frac{1}{2}\mathcal{C}^{ab}(c_3=1) \;=\; \begin{pmatrix} 0 & 0 & 0 \\ 0 & 0 & 0 \\ 0 & 0 & 1 \end{pmatrix} \tag{C.8}$$

$$\frac{1}{2}\mathcal{C}^{ab}\left(c_1=1/\sqrt{2},c_2=1/\sqrt{2}\right)+\frac{1}{2}\mathcal{C}^{ab}\left(c_0=1/\sqrt{2},c_3=1/\sqrt{2}\right) \;=\; \begin{pmatrix} 0 & 1 & 0 \\ 0 & 0 & 0 \\ 0 & 0 & 0 \end{pmatrix} \tag{C.9}$$

$$\frac{1}{2}\mathcal{C}^{ab}\left(c_1=1/\sqrt{2},c_2=1/\sqrt{2}\right)+\frac{1}{2}\mathcal{C}^{ab}\left(c_0=1/\sqrt{2},c_3=-1/\sqrt{2}\right) \;=\; \begin{pmatrix} 0 & 0 & 0 \\ 1 & 0 & 0 \\ 0 & 0 & 0 \end{pmatrix} \tag{C.10}$$

$$\frac{1}{2}\mathcal{C}^{ab}\left(c_2=1/\sqrt{2},c_3=1/\sqrt{2}\right)+\frac{1}{2}\mathcal{C}^{ab}\left(c_0=1/\sqrt{2},c_1=1/\sqrt{2}\right) \;=\; \begin{pmatrix} 0 & 0 & 0 \\ 0 & 0 & 1 \\ 0 & 0 & 0 \end{pmatrix} \tag{C.11}$$

$$\frac{1}{2}\mathcal{C}^{ab}\left(c_2=1/\sqrt{2},c_3=1/\sqrt{2}\right)+\frac{1}{2}\mathcal{C}^{ab}\left(c_0=1/\sqrt{2},c_1=-1/\sqrt{2}\right) \;=\; \begin{pmatrix} 0 & 0 & 0 \\ 0 & 0 & 0 \\ 0 & 1 & 0 \end{pmatrix} \tag{C.12}$$

$$\frac{1}{2}\mathcal{C}^{ab}\left(c_1=1/\sqrt{2},c_3=1/\sqrt{2}\right)+\frac{1}{2}\mathcal{C}^{ab}\left(c_0=1/\sqrt{2},c_2=1/\sqrt{2}\right) \;=\; \begin{pmatrix} 0 & 0 & 0 \\ 0 & 0 & 0 \\ 1 & 0 & 0 \end{pmatrix} \tag{C.13}$$

$$\frac{1}{2}\mathcal{C}^{ab}\left(c_1=1/\sqrt{2},c_3=1/\sqrt{2}\right)+\frac{1}{2}\mathcal{C}^{ab}\left(c_0=1/\sqrt{2},c_2=-1/\sqrt{2}\right) \;=\; \begin{pmatrix} 0 & 0 & 1 \\ 0 & 0 & 0 \\ 0 & 0 & 0 \end{pmatrix}. \tag{C.14}$$

Of course, there are also color orientation matrices $\mathcal{C}^{ab}(i)$, $i=10,\ldots,12$, so that any vector $\mathcal{S}^{a0}$ can be represented according to

$$\mathcal{S}^{a0} \;=\; \sum_{i=10}^{12}\mathcal{A}(i)\mathcal{C}^{a1}(i). \tag{C.15}$$

Appendix D

Any linear superposition of akyrons has vanishing topological charge density

In this appendix we prove that any linear superposition of akyrons has vanishing topological charge density.

The gauge field of a single akyron with index i, amplitude $\mathcal{A}(i)$, color orientation matrix $\mathcal{C}^{ab}(i)$ and position $z(i)$ is given by

$$A^a_\mu(i) \;=\; \mathcal{A}(i)\mathcal{C}^{ab}(i)a^b_{\mathrm{akyron},\mu}(x-z(i)) \;=\; \mathcal{A}(i)\mathcal{C}^{a1}(i)\frac{x_\mu - z_\mu(i)}{(x-z(i))^2+\lambda^2} \tag{D.1}$$

(c.f. (2.3)). In the corresponding field strength the derivative terms cancel each other:

$$F^a_{\mu\nu}(i) \;=\; \underbrace{\partial_\mu A^a_\nu(i) - \partial_\nu A^a_\mu(i)}_{=0} + \epsilon^{abc}A^b_\mu(i)A^c_\nu(i) \;=\; \epsilon^{abc}A^b_\mu(i)A^c_\nu(i). \tag{D.2}$$

For any linear superposition of akyrons

$$A^a_\mu \;=\; \sum_i A^a_\mu(i) \tag{D.3}$$

the same is true:

$$F^a_{\mu\nu} \;=\; \underbrace{\partial_\mu A^a_\nu - \partial_\nu A^a_\mu}_{=0} + \epsilon^{abc}A^b_\mu A^c_\nu \;=\; \epsilon^{abc}A^b_\mu A^c_\nu. \tag{D.4}$$

For the topological charge density follows

$$\begin{aligned} q \;&=\; \frac{1}{32\pi^2}F^a_{\mu\nu}\tilde{F}^a_{\mu\nu} \;=\; \frac{1}{64\pi^2}\epsilon_{\mu\nu\alpha\beta}F^a_{\mu\nu}F^a_{\alpha\beta} \;=\; \frac{1}{64\pi^2}\epsilon_{\mu\nu\alpha\beta}\epsilon^{abc}\epsilon^{ade}A^b_\mu A^c_\nu A^d_\alpha A^e_\beta \;= \\ &=\; \frac{1}{64\pi^2}\epsilon_{\mu\nu\alpha\beta}\Big(\delta^{bd}\delta^{ce}-\delta^{be}\delta^{cd}\Big)A^b_\mu A^c_\nu A^d_\alpha A^e_\beta \;=\; \frac{1}{32\pi^2}\underbrace{\epsilon_{\mu\nu\alpha\beta}(A^b_\mu A^b_\alpha)}_{=0}(A^c_\nu A^c_\beta) \;=\; 0. \end{aligned} \tag{D.5}$$

Appendix E

The Fourier transform of a pseudoparticle

In this appendix we calculate the Fourier transform of $x_\nu/(x^2+\lambda^2)$.
At first we replace x_ν in the numerator by a derivative:

$$\int d^4x\, e^{ikx} \frac{x_\nu}{x^2+\lambda^2} \;=\; -i\frac{\partial}{\partial k_\nu} \int d^4x\, e^{ikx} \frac{1}{x^2+\lambda^2}. \tag{E.1}$$

In order to calculate the integral, it is convenient to introduce spherical coordinates:

$$\begin{aligned} \int d^4x\, e^{ikx} \frac{1}{x^2+\lambda^2} \;&=\; 4\pi \int_0^\infty dr\, r^3 \int_0^\pi d\alpha \sin(\alpha)^2 e^{ikr\cos(\alpha)} \frac{1}{r^2+\lambda^2} \;= \\ &=\; 4\pi \int_0^\infty dr\, \frac{r^3}{r^2+\lambda^2} \int_0^\pi d\alpha \sin(\alpha)^2 e^{ikr\cos(\alpha)} \;=\; \ldots \end{aligned} \tag{E.2}$$

[39], page 486, 3.915(5.):

$$\ldots \;=\; 4\pi \int_0^\infty dr\, \frac{r^3}{r^2+\lambda^2} \left(\frac{\pi}{kr} J_1(kr)\right) \;=\; \frac{4\pi^2}{k} \int_0^\infty dr\, \frac{r^2 J_1(kr)}{r^2+\lambda^2} \;=\; \ldots \tag{E.3}$$

(J_1 is a Bessel function of the first kind). [39], page 671, 6.566(2.):

$$\ldots \;=\; \frac{4\pi^2 \lambda K_1(k\lambda)}{k} \tag{E.4}$$

(K_1 is a modified Bessel function of imaginary argument). Inserting (E.4) in (E.1) yields

$$\int d^4x\, e^{ikx} \frac{x_\nu}{x^2+\lambda^2} \;=\; -i\frac{\partial}{\partial k_\nu} \frac{4\pi^2 \lambda K_1(k\lambda)}{k} \;=\; \frac{8\pi^2 i k_\nu}{k^4} \left(\frac{k\lambda K_1(k\lambda)}{2} - \frac{k^2\lambda^2 K_1'(k\lambda)}{2}\right). \tag{E.5}$$

E.1 Instantons and antiinstantons form transverse gauge fields, akyrons form longitudinal gauge fields

Any gauge field A^a_μ can be written as a sum of plane waves:

$$A^a_\mu(x) = \frac{1}{(2\pi)^4}\int d^4k\, e^{-ikx}\tilde{A}^a_\mu(k), \tag{E.6}$$

where $\tilde{A}^a_\mu$, the Fourier transform of A^a_μ, is given by

$$\tilde{A}^a_\mu(k) = \int d^4k\, e^{ikx}A^a_\mu(x). \tag{E.7}$$

The Fourier transformed gauge field $\tilde{A}^a_\mu$ can be decomposed in a transverse and a longitudinal part:

$$\tilde{A}^a_\mu(k) = \tilde{A}^a_{\mu,\mathrm{transverse}}(k) + \tilde{A}^a_{\mu,\mathrm{longitudinal}}(k) \tag{E.8}$$

with

$$k_\mu\tilde{A}^a_{\mu,\mathrm{transverse}}(k) = 0 \tag{E.9}$$
$$\tilde{A}^a_{\mu,\mathrm{longitudinal}}(k) \propto k_\mu. \tag{E.10}$$

Superpositions of instantons (2.1) and antiinstantons (2.2) form transverse gauge fields, whereas superpositions of akyrons (2.3) form longitudinal gauge fields. This can be seen by considering the Fourier transforms of these pseudoparticles:

$$\tilde{a}^a_{\mu,\mathrm{instanton}}(k) = \eta^a_{\mu\nu}k_\nu f(k) \tag{E.11}$$
$$\tilde{a}^a_{\mu,\mathrm{antiinstanton}}(k) = \bar{\eta}^a_{\mu\nu}k_\nu f(k) \tag{E.12}$$
$$\tilde{a}^a_{\mu,\mathrm{akyron}}(k) = \delta^{a1}k_\mu f(k), \tag{E.13}$$

where

$$f(k) = \frac{8\pi^2 i}{k^4}\left(\frac{k\lambda K_1(k\lambda)}{2} - \frac{k^2\lambda^2 K_1'(k\lambda)}{2}\right) \tag{E.14}$$

(c.f. (E.5)). (E.11) and (E.12) satisfy (E.9) due to the antisymmetry of $\eta^a_{\mu\nu}$ and $\bar{\eta}^a_{\mu\nu}$, while (E.13) obviously fulfills (E.10).

Appendix F

The continuum limit in the pseudoparticle approach

In this section we discuss the continuum limit in the pseudoparticle approach, i.e. the limit of infinitely many pseudoparticles.

F.1 The gauge field

To begin with, we restrict the gauge field of an $\mathcal{A}$-ensemble (2.6) to instantons and akyrons and consider its continuum version:

$$\begin{aligned} A_\mu^a(x) &= \int d^4z \left(\sum_{i=1}^{9} \mathcal{A}(i,z) \mathcal{C}^{ab}(i,z) a^b_{\mu,\text{instanton}}(x-z) + \right. \\ &\left. \sum_{j=10}^{12} \mathcal{A}(j,z) \mathcal{C}^{ab}(j,z) a^b_{\mu,\text{akyron}}(x-z) \right). \end{aligned} \tag{F.1}$$

It is sufficient to consider nine instantons and three akyrons at the same spacetime point. Increasing the number of pseudoparticles further will not allow us to represent any other gauge field configurations.

In the following we demonstrate that "almost every gauge field configuration" A_μ^a can be represented according to (F.1), that is there exist amplitudes $\mathcal{A}(i)$ and $\mathcal{A}(j)$ and color orientation matrices $\mathcal{C}^{ab}(i)$ and $\mathcal{C}^{ab}(j)$ satisfying this equation. The first step is to insert (2.1) and (2.3) in (F.1) and to define functions $\mathcal{S}^{aB} = (\mathcal{S}^{a0}, \mathcal{S}^{ab})$ via

$$A_\mu^a(x) = \int d^4z \left(\underbrace{\sum_{i=1}^{9} \mathcal{A}(i,z) \mathcal{C}^{ab}(i,z)}_{=\mathcal{S}^{ab}(z)} \eta^b_{\mu\nu} + \underbrace{\sum_{j=10}^{12} \mathcal{A}(j,z) \mathcal{C}^{ab}(j,z) \delta^{b1}}_{=\mathcal{S}^{a0}(z)} \delta_{\mu\nu} \right) \frac{x_\nu - z_\nu}{(x-z)^2 + \lambda^2}. \tag{F.2}$$

It can be shown that any $\mathcal{S}^{aB}$ can be realized by suitably chosen amplitudes $\mathcal{A}(i)$ and $\mathcal{A}(j)$ and color orientation matrices $\mathcal{C}^{ab}(i)$ and $\mathcal{C}^{ab}(j)$ (c.f. Appendix C). Therefore, the problem has been

reduced to the question whether any gauge field configuration can be represented by suitably chosen $\mathcal{S}^{aB}$.

Fourier transforming (F.2) turns the convolution into an ordinary multiplication:

$$\begin{aligned}\tilde{A}^a_\mu(k) &= \left(\tilde{\mathcal{S}}^{ab}(k)\eta^b_{\mu\nu} + \tilde{\mathcal{S}}^{a0}(k)\delta_{\mu\nu}\right)\int d^4x\, e^{ikx}\frac{x_\nu}{x^2+\lambda^2} \quad = \\ &= \left(\tilde{\mathcal{S}}^{ab}(k)\eta^b_{\mu\nu} + \tilde{\mathcal{S}}^{a0}(k)\delta_{\mu\nu}\right)\frac{8\pi^2 i k_\nu}{|k|^4}\left(\frac{|k|\lambda K_1(|k|\lambda)}{2} - \frac{k^2\lambda^2 K_1'(|k|\lambda)}{2}\right) \qquad \text{(F.3)}\end{aligned}$$

(the Fourier transform of $x_\nu/(x^2+\lambda^2)$ is carried out in Appendix E; K_1 is a modified Bessel function of imaginary argument). Without loss of generality we consider $a = 1$:

$$\begin{pmatrix}\tilde{A}^1_0(k)\\ \tilde{A}^1_1(k)\\ \tilde{A}^1_2(k)\\ \tilde{A}^1_3(k)\end{pmatrix} =$$

$$= \underbrace{\frac{8\pi^2 i}{|k|^4}\left(\frac{|k|\lambda K_1(|k|\lambda)}{2} - \frac{k^2\lambda^2 K_1'(|k|\lambda)}{2}\right)}_{\mathcal{F}(k)}\underbrace{\begin{pmatrix}k_0 & -k_1 & -k_2 & -k_3\\ k_1 & k_0 & -k_3 & k_2\\ k_2 & k_3 & k_0 & -k_1\\ k_3 & -k_2 & k_1 & k_0\end{pmatrix}}_{=\mathcal{K}(k)}\begin{pmatrix}\tilde{\mathcal{S}}^{10}(k)\\ \tilde{\mathcal{S}}^{11}(k)\\ \tilde{\mathcal{S}}^{12}(k)\\ \tilde{\mathcal{S}}^{13}(k)\end{pmatrix}. \qquad \text{(F.4)}$$

For $k \neq 0$ this equation can be solved for $(\tilde{\mathcal{S}}^{10}, \tilde{\mathcal{S}}^{11}, \tilde{\mathcal{S}}^{12}, \tilde{\mathcal{S}}^{13})$, because $\mathcal{F} \neq 0$ and $\det(\mathcal{K}) = |k|^4 \neq 0$. For $k = 0$ both $\mathcal{F}$ and $\mathcal{K}$ are singular. To study this case, we first deduce

$$\int d^4x\, A^a_\mu(x) \quad = \quad 0 \qquad \text{(F.5)}$$

from (F.2) by applying a proper regularization scheme. (F.5) implies $\tilde{A}^a_\mu(k=0) = 0$. Inserting this in (F.4) shows that the value of $\tilde{\mathcal{S}}^{aB}(k=0)$ has no effect on the gauge field A^a_μ. On the other hand, changing $\tilde{\mathcal{S}}^{aB}(k=0)$ amounts to a constant shift of $\mathcal{S}^{aB}$: $\mathcal{S}^{aB} \to \mathcal{S}^{aB} + \mathcal{S}^{aB}_0$. That is adding $\mathcal{S}^{aB}_0$ changes $\mathcal{S}^{aB}$, whereas the gauge field A^a_μ remains unaltered. To get rid of this redundancy, we require

$$\mathcal{G}[\mathcal{S}^{aB}] \quad = \quad \int d^4x\, \mathcal{S}^{aB}(x) \quad = \quad 0. \qquad \text{(F.6)}$$

Of course, there are many other sensible conditions, which could have been chosen.

To be able to represent any gauge field configuration, we have to find a way around (F.5). This can easily be achieved by adding constants B^a_μ to (F.1).

The final result is the following: any gauge field configuration A^a_μ has a unique expansion

$$A^a_\mu(x) \quad = \quad \int d^4z\, \left(\mathcal{S}^{ab}(z)a^b_{\mu,\text{instanton}}(x-z) + \mathcal{S}^{a0}(z)a^1_{\mu,\text{akyron}}(x-z)\right) + B^a_\mu \qquad \text{(F.7)}$$

in terms of $S^{aB}(z)$ and B^a_μ with $S^{aB}(z)$ constrained by (F.6). Instead of $S^{aB}(z)$ one can also use amplitudes $\mathcal{A}(i,z)$, $i=1,\ldots,12$, with fixed and linearly independent color orientation matrices $\mathcal{C}^{ab}(i,z)$, $i=1,\ldots,9$, and $\mathcal{C}^{a1}(j,z)$, $j=10,\ldots,12$:

$$\begin{aligned} A^a_\mu(x) &= \int d^4z \left(\sum_{i=1}^{9} \mathcal{A}(i,z)\mathcal{C}^{ab}(i,z) a^b_{\mu,\text{instanton}}(x-z) + \right. \\ &\left. \sum_{j=10}^{12} \mathcal{A}(j,z)\mathcal{C}^{ab}(j,z) a^b_{\mu,\text{akyron}}(x-z) \right) + B^a_\mu. \end{aligned} \tag{F.8}$$

Note that instead of instantons one can also use antiinstantons.

F.2 The integration measure

Now that we have convinced ourselves that any gauge field configuration has a unique expansion in terms of $(\mathcal{S}^{aB}(z), B^a_\mu)$ or $(\mathcal{A}(i,z), B^a_\mu)$, we turn our attention to the integration measure of the path integral. Since the relation between A^a_μ and $(\mathcal{S}^{aB}(z), B^a_\mu)$ as well as $(\mathcal{A}(i,z), B^a_\mu)$ is linear and invertible (c.f. (F.6) to (F.8)), the Jacobian appearing after a change of coordinates is merely an irrelevant constant. The integration measure corresponding to coordinates $(\mathcal{S}^{aB}(z), B^a_\mu)$ is given by

$$\begin{aligned} \int DA \ldots &= \int \left(\prod_{a,B} D\mathcal{S}^{aB}\, \delta(\mathcal{G}[\mathcal{S}^{aB}]) \right) \left(\prod_{\mu,a} dB^a_\mu \right) \underbrace{\left| \frac{\delta A^a_\mu}{\delta(\mathcal{S}^{aB}, B^a_\mu)} \right|}_{=\text{constant}} \ldots \propto \\ &\propto \int \left(\prod_{a,B} D\mathcal{S}^{aB}\, \delta(\mathcal{G}[\mathcal{S}^{aB}]) \right) \left(\prod_{\mu,a} dB^a_\mu \right) \ldots, \end{aligned} \tag{F.9}$$

whereas the integration measure corresponding to coordinates $(\mathcal{A}(i,z), B^a_\mu)$ is given by

$$\begin{aligned} \int DA \ldots &= \int \left(\prod_{i} D\mathcal{A}(i) \right) \left(\prod_{a,B} \delta(\mathcal{G}[\mathcal{S}^{aB}(\mathcal{A}(i))]) \right) \left(\prod_{\mu,a} dB^a_\mu \right) \underbrace{\left| \frac{\delta A^a_\mu}{\delta(\mathcal{A}(i), B^a_\mu)} \right|}_{=\text{constant}} \ldots \propto \\ &\propto \int \left(\prod_{i} D\mathcal{A}(i) \right) \left(\prod_{a,B} \delta(\mathcal{G}[\mathcal{S}^{aB}(\mathcal{A}(i))]) \right) \left(\prod_{\mu,a} dB^a_\mu \right) \ldots \end{aligned} \tag{F.10}$$

F.3 Approximations with the correct naive continuum limit

In this section we show that $\mathcal{A}$-ensembles and $\mathcal{S}^{12}$-ensembles are approximations of SU(2) Yang-Mills theory, which possess the correct naive continuum limit (with exception of the constants B^a_μ).

F.3.1 "$\mathcal{A}$-ensembles"

A straightforward approximation of (F.8) with a finite number of pseudoparticles is

$$A^a_\mu(x) = \sum_i \mathcal{A}(i)\mathcal{C}^{ab}(i)a^b_{\mu,\text{instanton}}(x-z(i)) + \sum_j \mathcal{A}(j)\mathcal{C}^{ab}(j)a^b_{\mu,\text{antiinstanton}}(x-z(j)) + \sum_k \mathcal{A}(k)\mathcal{C}^{ab}(k)a^b_{\mu,\text{akyron}}(x-z(k)) + B^a_\mu \tag{F.11}$$

with randomly chosen positions $z(i)$ inside a spacetime hypersphere. Although it is of no relevance in the continuum limit, we consider an equal number of instantons and antiinstantons. The approximation is then symmetric with respect to the topological charge (c.f. (2.5)). According to section F.1, where we have seen that there are three times as many instanton/antiinstanton degrees of freedom as there are akyron degrees of freedom, we choose
$N_{\text{instanton}} : N_{\text{antiinstanton}} : N_{\text{akyron}} = 3 : 3 : 2$.

The integration over all field configurations (F.10) is approximated by

$$\int DA \ldots \propto \int \left(\prod_i d\mathcal{A}(i)\right)\left(\prod_{\mu,a} dB^a_\mu\right)\ldots \tag{F.12}$$

Because we are considering a finite spacetime region, we were allowed to drop the δ-functions. They have no effect on any finite spacetime region.

With exception of the constants B^a_μ this is an $\mathcal{A}$-ensemble (c.f. section 2.2.1).

F.3.2 "$\mathcal{S}^{12}$-ensembles"

This time the starting point is (F.7). Replacing the integral by a sum yields

$$A^a_\mu(x) = \sum_i \left(\mathcal{S}^{ab}(i)a^b_{\mu,\text{instanton}}(x-z(i)) + \mathcal{S}^{a0}(i)a^1_{\mu,\text{akyron}}(x-z(i))\right) + B^a_\mu = \sum_i \mathcal{S}^{aB}(i)a^B_{\mu,\mathcal{S}^{12}}(x-z(i)) + B^a_\mu, \tag{F.13}$$

with $a^B_{\mu,\mathcal{S}^{12}}$ defined by (2.10).

The integration over all field configurations (F.9) is approximated by

$$\int DA \ldots \propto \int \left(\prod_{i,a,B} d\mathcal{S}^{aB}(i)\right)\left(\prod_{\mu,a} dB^a_\mu\right)\ldots \tag{F.14}$$

Again we have dropped the δ-functions.

With exception of the constants B^a_μ this is an $\mathcal{S}^{12}$-ensemble (c.f. section 2.2.3).

Appendix G

Calculating Wilson loops numerically

In this appendix we explain how to compute Wilson loops numerically.

The starting point is (3.1). We parameterize the closed spacetime curve z defining the Wilson loop W_z by $\lambda \in [\lambda_{\min}, \lambda_{\max}]$:

$$\begin{aligned} W_z[A] &= \frac{1}{2}\mathrm{Tr}\left(P\left\{\exp\left(i\oint dz_\mu\, A_\mu(z)\right)\right\}\right) = \\ &= \frac{1}{2}\mathrm{Tr}\left(P\left\{\exp\left(i\int_{\lambda_{\min}}^{\lambda_{\max}} d\lambda\, \frac{dz_\mu(\lambda)}{d\lambda} A_\mu(z(\lambda))\right)\right\}\right). \end{aligned} \tag{G.1}$$

To approximate this expression numerically, we replace the integral in the exponent by a sum. The exponential function can be written as a path ordered product:

$$\begin{aligned} W_z[A] &\approx \frac{1}{2}\mathrm{Tr}\left(P\left\{\exp\left(i\sum_{i=1}^{N}\Delta z_\mu(i) A_\mu(i)\right)\right\}\right) = \\ &= \frac{1}{2}\mathrm{Tr}\left(P\left\{\prod_{i=1}^{N}\exp\left(i\Delta z_\mu(i) A_\mu(i)\right)\right\}\right), \end{aligned} \tag{G.2}$$

where

$$\begin{aligned} \Delta z_\mu(i) &= \Delta\lambda\, \frac{dz_\mu(\lambda)}{d\lambda}\bigg|_{\lambda=\lambda(i)} \quad , \quad \Delta\lambda = \frac{\lambda_{\max}-\lambda_{\min}}{N} \quad , \\ \lambda(i) &= \lambda_{\min} + \left(i-\frac{1}{2}\right)\Delta\lambda \quad , \quad A_\mu(i) = A_\mu(z(i)) \quad , \quad z(i) = z(\lambda(i)). \end{aligned} \tag{G.3}$$

The coefficients of the path ordered product in (G.2) can be calculated:

$$\exp\left(i\Delta z_\mu(i) A_\mu(i)\right) = \cos(|\vec{\alpha}(i)|) + i\sin(|\vec{\alpha}(i)|)\frac{\vec{\alpha}(i)}{|\vec{\alpha}(i)|}\vec{\sigma} \quad , \quad \alpha^a(i) = \frac{\Delta z_\mu(i) A^a_\mu(i)}{2}. \tag{G.4}$$

G.1 Choosing an appropriate number of sample points

When calculating Wilson loops numerically via (G.2), it is important to choose an appropriate number of sample points. In order to save computation time, we would like to choose N as small as possible. On the other hand, the numerical error involved should be negligible.

To get a better understanding of the magnitude of the numerical error, associated with different sample point densities, we studied two cases, where Wilson loops can be calculated analytically:

a) Circular Wilson loops in the 1-2-plane, radius r, $A_1^1 = A_2^2 = \beta$ [42]:

$$W_z[A] \quad = \quad -\cos\left(\pi\left(1+r^2\beta^2\right)^{1/2}\right). \tag{G.5}$$

b) Circular Wilson loops, "perpendicular to a single instanton" (c.f. [43], section 4.2.1).

Using different sample point densities, we computed the analytical and the numerical values of $10,000$ Wilson loops with randomly chosen parameters in both cases:

- Case a): $r \in [0.2, 1.0]$, $\beta \in [-1.0, 1.0]$.
- Case b): $r \in [0.2, 1.0]$, $\xi \in [0.0, 2.0]$, the instanton has size $\lambda = 1.0$ and a randomly chosen color orientation.

From the results we calculated the maximum absolute error and the mean error (Table G.1). There is strong empirical evidence that both errors are of order $1/(\text{sample point density})^2$.

	maximum absolute error	mean error
Case a), sample point density = 10.0	$8.75600e^{-04}$	$1.20751e^{-04} \pm 1.81233e^{-06}$
Case a), sample point density = 100.0	$8.83737e^{-06}$	$1.23419e^{-06} \pm 1.84447e^{-08}$
Case a), sample point density = 1000.0	$8.85994e^{-08}$	$1.23695e^{-08} \pm 1.84781e^{-10}$
Case b), sample point density = 10.0	$7.55270e^{-04}$	$-2.81595e^{-04} \pm 2.16789e^{-06}$
Case b), sample point density = 100.0	$7.57427e^{-06}$	$-2.87862e^{-06} \pm 2.20653e^{-08}$
Case b), sample point density = 1000.0	$7.58124e^{-08}$	$-2.88564e^{-08} \pm 2.21073e^{-10}$

Table G.1: average errors in the numerical calculation of Wilson loops due to insufficient sampling.

All results presented in this work have been calculated with a sample point density of at least 5.0. Figure G.1 shows a typical example, for which a sample point density of 5.0 is more than sufficient (for sample point densities $\gtrsim 1.0$ ensemble averages of Wilson loops are indistinguishable within statistical errors).

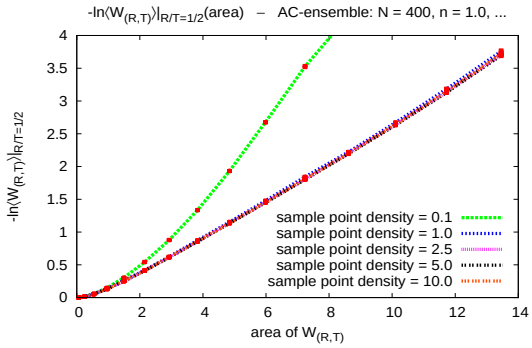

Figure G.1: $\mathcal{AC}$-ensemble, $N = 400$, $n = 1.0$, $\lambda = 0.5$, $g = 4.0$. $-\ln\langle W_{(R,T)}\rangle|_{R/T=1/2}$ calculated with different sample point densities plotted against the area.

Bibliography

[1] R. P. Feynman, "Space-Time Approach To Nonrelativistic Quantum Mechanics," Rev. Mod. Phys. **20** (1948) 367.

[2] K. G. Wilson, "Confinement Of Quarks," Phys. Rev. D **10** (1974) 2445.

[3] M. Creutz, "Confinement And The Critical Dimensionality Of Space-Time," Phys. Rev. Lett. **43** (1979) 553 [Erratum-ibid. **43** (1979) 890].

[4] M. Creutz, L. Jacobs and C. Rebbi, "Monte Carlo Study Of Abelian Lattice Gauge Theories," Phys. Rev. D **20** (1979) 1915.

[5] M. Creutz, "Monte Carlo Study Of Quantized SU(2) Gauge Theory," Phys. Rev. D **21** (1980) 2308.

[6] M. Creutz, "Asymptotic Freedom Scales," Phys. Rev. Lett. **45** (1980) 313.

[7] T. Schafer and E. V. Shuryak, "Instantons In QCD," Rev. Mod. Phys. **70** (1998) 323 [arXiv:hep-ph/9610451].

[8] F. Lenz, J. W. Negele and M. Thies, "Confinement From Merons," Phys. Rev. D **69** (2004) 074009 [arXiv:hep-th/0306105].

[9] J. W. Negele, F. Lenz and M. Thies, "Confinement From Instantons Or Merons," Nucl. Phys. Proc. Suppl. **140** (2005) 629 [arXiv:hep-lat/0409083].

[10] L. Del Debbio, M. Faber, J. Giedt, J. Greensite and S. Olejnik, "Detection Of Center Vortices In The Lattice Yang-Mills Vacuum," Phys. Rev. D **58** (1998) 094501 [arXiv:hep-lat/9801027].

[11] M. Wagner and F. Lenz, "The Pseudoparticle Approach For Solving Path Integrals In Gauge Theories," PoS **LAT2005** (2005) 315 [arXiv:hep-lat/0510083].

[12] R. Jackiw and C. Rebbi, "Conformal Properties Of A Yang-Mills Pseudoparticle," Phys. Rev. D **14** (1976) 517.

[13] H. J. Rothe, "Lattice Gauge Theories: An Introduction," World Sci. Lect. Notes Phys. **74** (2005) 1.

[14] M. Creutz, "Quarks, Gluons And Lattices," Cambridge Univ. Pr. (1983) 1.

[15] J. D. Stack, "The Heavy Quark Potential In SU(2) Lattice Gauge Theory," Phys. Rev. D **27** (1983) 412.

[16] G. S. Bali, K. Schilling and C. Schlichter, "Observing Long Color Flux Tubes In SU(2) Lattice Gauge Theory," Phys. Rev. D **51** (1995) 5165 [arXiv:hep-lat/9409005].

[17] M. Lüscher and P. Weisz, "Quark Confinement And The Bosonic String," JHEP **0207** (2002) 049 [arXiv:hep-lat/0207003].

[18] M. Lüscher, K. Symanzik and P. Weisz, "Anomalies Of The Free Loop Wave Equation In The WKB Approximation," Nucl. Phys. B **173** (1980) 365.

[19] M. Lüscher, "Symmetry Breaking Aspects Of The Roughening Transition In Gauge Theories," Nucl. Phys. B **180** (1981) 317.

[20] L. S. Brown and W. I. Weisberger, "Remarks On The Static Potential In Quantum Chromodynamics," Phys. Rev. D **20** (1979) 3239.

[21] W. Lucha, F. F. Schoberl and D. Gromes, "Bound States Of Quarks," Phys. Rept. **200** (1991) 127.

[22] P. Di Vecchia, K. Fabricius, G. C. Rossi and G. Veneziano, "Preliminary Evidence For U(1)-A Breaking In QCD From Lattice Calculations," Nucl. Phys. B **192** (1981) 392.

[23] M. Teper, "Unmasking The Topological Charge Content Of Fluctuating Lattice Gauge Fields," Phys. Lett. B **232** (1989) 227.

[24] C. Christou, A. Di Giacomo, H. Panagopoulos and E. Vicari, "Improved Lattice Operators: The Case Of The Topological Charge Density," Phys. Rev. D **53** (1996) 2619 [arXiv:hep-lat/9510023].

[25] A. Di Giacomo, "Topology In Lattice QCD," arXiv:hep-lat/9711034.

[26] E. Witten, "Current Algebra Theorems For The U(1) 'Goldstone Boson'," Nucl. Phys. B **156** (1979) 269.

[27] M. J. Teper, "Glueball Masses And Other Physical Properties Of SU(N) Gauge Theories In D = 3+1: A Review Of Lattice Results For Theorists," arXiv:hep-th/9812187.

[28] B. J. Harrington and H. K. Shepard, "Periodic Euclidean Solutions And The Finite Temperature Yang-Mills Gas," Phys. Rev. D **17** (1978) 2122.

[29] D. J. Gross, R. D. Pisarski and L. G. Yaffe, "QCD And Instantons At Finite Temperature," Rev. Mod. Phys. **53** (1981) 43.

[30] M. Wagner, K. Hormann and G. Greiner, "C^2-Continuous Surface Reconstruction With Piecewise Polynomial Patches," Preprint (2003).

[31] L. D. McLerran and B. Svetitsky, "Quark Liberation At High Temperature: A Monte Carlo Study Of SU(2) Gauge Theory," Phys. Rev. D **24** (1981) 450.

[32] S. A. Gottlieb, J. Kuti, D. Toussaint, A. D. Kennedy, S. Meyer, B. J. Pendleton and R. L. Sugar, "The Deconfining Phase Transition And The Continuum Limit Of Lattice Quantum Chromodynamics," Phys. Rev. Lett. **55** (1985) 1958.

[33] M. Engelhardt, K. Langfeld, H. Reinhardt and O. Tennert, "Deconfinement In SU(2) Yang-Mills Theory As A Center Vortex Percolation Transition," Phys. Rev. D **61** (2000) 054504 [arXiv:hep-lat/9904004].

[34] V. G. Bornyakov, V. K. Mitrjushkin and M. Müller-Preussker, "Deconfinement Transition And Abelian Monopoles In SU(2) Lattice Gauge Theory," Phys. Lett. B **284** (1992) 99.

[35] F. Gliozzi, S. Lottini, M. Panero and A. Rago, "Random Percolation As A Gauge Theory," Nucl. Phys. B **719** (2005) 255 [arXiv:cond-mat/0502339].

[36] K. E. Cahill, "Noncompact Lattice Simulations Of SU(2) Gauge Theory," Phys. Lett. B **304** (1993) 307 [arXiv:hep-lat/9301010].

[37] K. E. Cahill, "Gauge Invariance And Confinement In Noncompact Simulations Of SU(2)," Nucl. Phys. Proc. Suppl. **34** (1994) 231 [arXiv:hep-lat/9312077].

[38] A. A. Belavin, A. M. Polyakov, A. S. Shvarts and Y. S. Tyupkin, "Pseudoparticle Solutions Of The Yang-Mills Equations," Phys. Lett. B **59** (1975) 85.

[39] I. S. Gradshteyn and I. M. Ryzhik, "Table Of Integrals, Series And Products," Academic Pr. (2000) 1.

[40] S. Brandt, "Data Analysis: Statistical And Computational Methods For Scientists And Engineers," Springer (1998) 1.

[41] A. H. Rosenfeld, A. Barbaro-Galtieri, W. J. Podolsky, L. R. Price, P. Soding, C. G. Wohl, M. Roos and W. J. Willis, "Data On Particles And Resonant States," Rev. Mod. Phys. **39** (1967) 1.

[42] M. Wagner, Private Communications (2005).

[43] A. Brzoska, "Dynamics Of Loop Variables In QCD," PhD thesis, Institute of Theoretical Physics III, Friedrich-Alexander-University Erlangen-Nürnberg (2005).

Danksagung

Herzlich danken möchte ich Prof. Frieder Lenz für die hervorragende Betreuung meiner Doktorarbeit. Zahlreiche Diskussionen, Tips und Ratschläge haben diese Arbeit in ihrer hier vorliegenden Form erst möglich gemacht. Darüber hinaus habe ich in unzähligen physikalischen Diskussionen, die nicht direkt mit meiner eigentlichen Arbeit verbunden waren, sehr viel gelernt; hervorzuheben sind hier die internen Workshops über Stringtheorie und über Quantenfeldtheorie in gekrümmten Räumen. Ebenfalls bedanken möchte ich mich für Hilfe und Tips bei der Vorbereitung diverser Vorträge, insbesondere die große Unterstützung die mir die Teilnahme an der LATTICE-2005-Konferenz in Dublin ermöglicht hat.

Für viele nutzbringende Diskussionen, hilfreiche Ratschläge, motivierende Worte sowie interessante Vorlesungen während meines Studiums und meiner Promotion möchte ich Prof. Günther Greiner, Prof. Alfred Hüller, Priv. Doz. Jan M. Pawlowski und Prof. Erhard Steffens ebenfalls herzlich danken.

Außerdem gilt mein Dank meinen momentanen und ehemaligen Kollegen die alle dazu beigetragen haben, dass ich meine Zeit am Institut für Theoretische Physik III als sehr angenehm empfunden habe. Besondere Erwähnung verdienen in diesem Zusammenhang meine Freunde Stephan Eisen, Matthias Schott und Konrad Urlichs.

Lebenslauf

Daten zur Person

Marc Wagner

Geburtsdatum: 17. September 1975

Familienstand: ledig

Staatsangehörigkeit: deutsch

Schulbildung

1981-1985	Grundschule in Wintersdorf
1985-1994	Dietrich-Bonhoeffer-Gymnasium in Oberasbach

Zivildienst

Okt. 1994-Dez. 1995	Altenpfleger im Pflegeheim der Arbeiterwohlfahrt in Zirndorf

Professionelles Tennis

1996-1997

Studium und Promotion

Okt. 1997-Sept. 2002	Studium der Informatik an der FAU-Erlangen
	Diplomarbeit: "Rekonstruktion glatter Oberflächen mit getrimmten B-Spline-Flächen", Note 1,0
	Diplomhauptprüfung: Gesamtnote 1,0 = "mit Auszeichnung bestanden"
Okt. 2000-März 2003	Studium der Physik an der FAU-Erlangen im Rahmen eines Doppelstudiums
	Diplomvorprüfung: Gesamtnote 1,0 = "sehr gut"
April 2003-heute	Promotion in theoretischer Elementarteilchenphysik am Institut für theoretische Physik III der FAU-Erlangen